Title

Pushing the Helium Envelope: Signatures of Normal and Unusual Supernovae from Sub-Chandrasekhar Mass White Dwarf Explosions

Author

Polin, Abigail E.

Publication Date

2020

Peer reviewed|Thesis/dissertation

Pushing the Helium Envelope: Signatures of Normal and Unusual Supernovae from Sub-Chandrasekhar Mass White Dwarf Explosions

by

Abigail E. Polin

A dissertation submitted in partial satisfaction of the

requirements for the degree of

Doctor of Philosophy

in

Physics

in the

Graduate Division

of the

University of California, Berkeley

Committee in charge:

Dr. Peter Nugent, Co-chair
Associate Professor Daniel Kasen, Co-chair
Professor Christopher McKee
Professor Alexei V. Filippenko

Spring 2020

Pushing the Helium Envelope: Signatures of Normal and Unusual Supernovae from Sub-Chandrasekhar Mass White Dwarf Explosions

Abstract

Pushing the Helium Envelope: Signatures of Normal and Unusual Supernovae from Sub-Chandrasekhar Mass White Dwarf Explosions

by

Abigail E. Polin

Doctor of Philosophy in Physics

University of California, Berkeley

Dr. Peter Nugent, Co-chair

Associate Professor Daniel Kasen, Co-chair

Type Ia supernovae (SNe) are among the most common astrophysical transients, yet their progenitors are still unknown. Throughout this thesis we examine a specific pathway to these explosions – the double detonation explosion mechanism. In this scenario a white dwarf (WD) is able to explode below the Chandrasekhar mass limit through the aid of an accreted helium shell. An ignition of this helium can send a shock wave into the center of the WD which, upon convergence, can ignite the core causing a thermonuclear runaway resulting in a Type Ia-like explosion.

Prior to this work, the double detonation scenario was not favored as a mechanism for Type Ia SNe, as there was no strong observational evidence supporting it. The first part of this thesis is a calculation of observational predictions of double detonation explosions. We perform hydrodynamical simulations and radiative transport calculations in order to produce testable predictions for observers. In doing so we identify a population of SNe Type Ia that likely arise from the double detonation progenitor channel recognized by the relationship between their Si II velocity and peak luminosity, and characteristic early color evolution.

While the double detonation scenario has mainly been employed to model signatures of SNe Type Ia, requiring WD masses greater than $\sim$0.9 $M_{\odot}$ and helium shell masses less than $\sim$0.01 $M_{\odot}$, there exists a wide parameter space beyond these limits which allows for more peculiar transients. We examine these regions and relate low mass double detonations to Ca-rich transients by their properties in the nebular phase. We also determine the peculiar signatures of double detonations triggered by thick helium shells. In doing so this work accurately predicts the observable properties associated with these events, which were later seen in SN 2018byg, establishing the most direct evidence to date that there are multiple mechanisms through which WDs explode.

I dedicate this thesis to my parents.
I hope you enjoy this theory. Which is mine.

Contents

Acknowledgments

This thesis, like most scientific endeavors, has been a collaborative effort. I would like to take this opportunity to thank all of the people who have helped me get to this point.

First, I would like to express my gratitude to my thesis advisors, Peter Nugent and Dan Kasen. Every graduate student hopes to have a good advisor, I have had the great fortune to have two. Your guidance over the past five years has been invaluable, and the experience of your combined expertise has shaped me into the scientist I am today. Thank you. I hope that the end of my time at Berkeley just marks the beginning of the work we will do together.

I have been fortunate to collaborate with several people, whose influence has helped shape this investigation. I would like to thank the ZTF Theory Network, and especially Lars Bildsten. Participating in this collaboration has helped me bridge that transition from student to independent researcher. The Sedona group, with a special thanks to Hannah Klion for taking it upon herself to implement checkpoints in the code. I am grateful to all of the observers who have pulled me in to help analyze interesting events. In particular I would like to thank Mansi Kasliwal, Ryan Foley, Kishalay De, and Wynn Jacobson-Galán, the results of my collaborations with whom appear in this text. And, of course, I would like to thank my thesis committee, your input has bettered this document.

I would also like to recognize the mentors who helped me get to graduate school in the first place, and whose guidance I value immensely, including: Andrea Lommen, Paul Chaikin, Maryam Modjaz, David Hogg, Andrew MacFadyen and Gabriela Gonzáles.

A huge part of graduate school is built upon the interactions amongst peers. I would like to thank the graduate students who have overlapped with me at Berkeley for making this experience the best it could be. In addition to those named elsewhere, I would like to particularly thank Charles Goullaud, Simca Bouma, Tom Zick, Jennifer Barnes, Austin Hedeman, Wren Suess, Melanie Veale, Chelsea Harris, Fatima Abdurrahman, Ellie Abrahams, and Sarafina Nance, who I consider friends as well as colleagues.

I would not be where I am without the support of my family. I would like to thank my parents, Sonya and David, for instilling a love of learning in me from an early age. Although, when you dropped me off at my first day of school I'm not sure you had another 27 years in mind. Thank you for making sure I knew that girls don't need to grow out of science. I would also like to thank my brothers, Daniel and Jonathan, my grandmothers, Beverly and Sonya, and the Duffell clan, for all of your love and support throughout the years.

I find myself needing to add some new acknowledgments right at the end of this process due to the people who have gotten me through the COVID-19 shelter in place with any semblance of productivity and sanity. I would like to thank my group: Dan Kasen, David Khatami, Hannah Klion and Siva Darbha, whose participation in our daily zoom check ins is solely responsible for helping me maintain any sort of schedule over these past two months. As well as my housemates, for being gracious and conscientious during this stressful time.

Lastly I would like to thank my partner, Paul Duffell, for your unyielding support, for believing in me, and for reminding me to believe in myself. Oh, and the coffee. Thank you for all of the coffee.

Chapter 1

Introduction

1.1 Type Ia Supernovae

Type Ia supernovae (SNe) are among the most common astrophysical transients, yet their progenitors are still unknown. Despite this they are used as cosmological distance measures, or standard candles. Here we describe the observational properties of SNe Type Ia, the diversity within this class, and their importance for astronomy as a whole.

1.1.1 Observational Properties

There are two main methods that we can use to examine SNe, photometry and spectroscopy. The light curves which we gain from photometric observations reveal to us how the luminosity of an event changes over time. From this we learn about what powers the SN. The spectra allow us to examine the energy distribution of the photons received from these events at a given snapshot in time. The absorption and emission features in these spectra reveal the composition of the SN ejecta.

Photometric Properties

The light curves of most Type Ia SNe are qualitatively similar. Figure 1.1 shows the main features of a normal SN Ia light curve. We see a rising period where the luminosity increases toward a period of maximum brightness. This rise typically occurs over approximately 20 days. Then we see a peak in the light curve, powered by the radioactive decay of ^{56}Ni. There is then a period of decline, followed, for normal SNe Ia, by a secondary peak in the near infrared (NIR) (Wood-Vasey et al. 2008). The last phase is a slow decline powered by the radioactive decay of ^{56}Co, the radioactive daughter of ^{56}Ni (Arnett 1982).

An important quantity gleaned from SN Ia light curves is Δm_{15}, the amount that the light curve luminosity decreases over the first 15 days after peak. This is a measure of the light curve width that we use to calibrate SN Ia light curves. Historically it has been thought that, despite SN Ia light curves displaying some variation, these events are largely from a

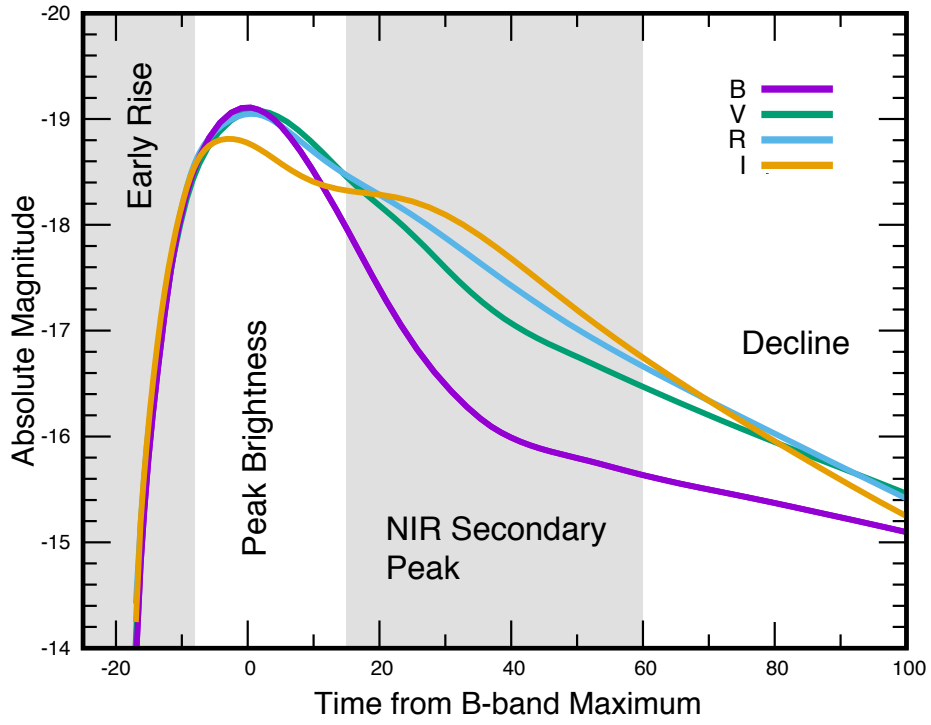

Figure 1.1: The light curves of a normal Type Ia SN, specifically the B, V, R, and I-band light curves of SN 2011fe. The epochs are separated into four regimes: the early rise, followed by a period of maximum light, followed by a secondary peak in the NIR (yellow) before the light curve slowly declines in all bands. Data collected from Silverman et al. (2012) via the open supernova catalog (OSC) (Guillochon et al. 2017).

one parameter family determined by the amount of ^{56}Ni synthesized in the explosion. This would allow for a standard width-luminosity relationship such that events with a smaller Δm_{15} (those with wider light curves) are intrinsically more luminous (Phillips 1993). This allows us to determine the intrinsic brightness of these events making them useful for cosmology (see Section 1.1.3). However, recent studies have suggested that in order to describe the full landscape of Type Ia SN light curves we need to also consider a second parameter, that of a varying ejecta mass (Stritzinger et al. 2006; Scalzo et al. 2014; Goldstein & Kasen 2018), complicating the process of determining the intrinsic luminosity of a Type Ia SN from its light curve alone.

Spectroscopic Properties

Spectra contain more information about a SN than light curves; however they are also observationally far more expensive to obtain. There are two distinct spectral epochs of

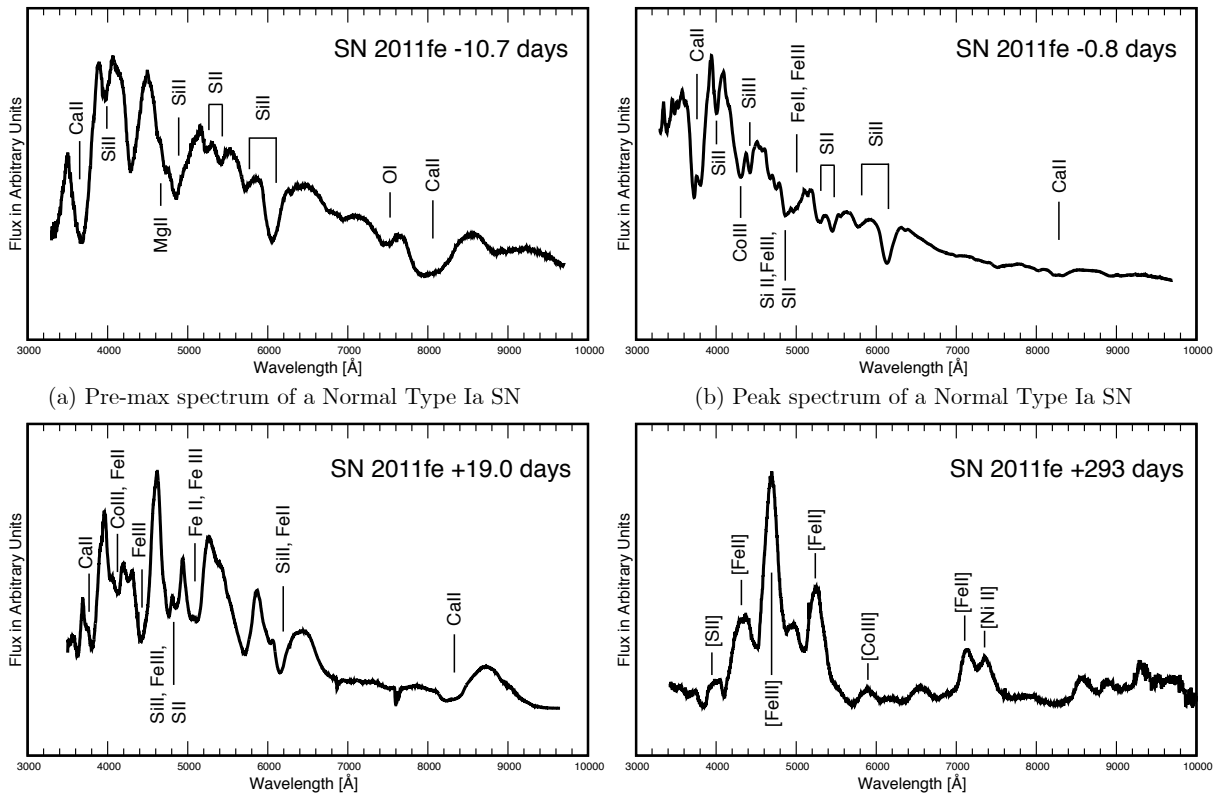

(a) Pre-max spectrum of a Normal Type Ia SN

(b) Peak spectrum of a Normal Type Ia SN

(c) Post-max spectrum of a Normal Type Ia SN

(d) Nebular spectrum of a Normal Type Ia SN

Figure 1.2: Sample spectra of the normal Type Ia SN 2011fe, exhibiting the evolution typical of this class. Early spectra (a) exhibit absorption features from IMEs, which at peak (b) are joined by IGE absorption features, and these IGEs dominate the spectra at late times (c). Panel (d) shows the nebular emission spectrum for SN 2011fe, which cools primarily through IGEs. Data taken from Pereira et al. (2013)(a&b), Yaron & Gal-Yam (2012)(c), and Mazzali et al. (2015)(d) via the OSC.

interest for SNe: the photospheric phase and the nebular phase.

During the photospheric phase we can envision the SN ejecta as an expanding ball of material, and over time we are able to probe deeper and deeper into that ejecta as the outer layers expand and become optically thin allowing the photosphere to recede. Typically for Type Ia SNe, the radioactive material (again ^{56}Ni) is confined to the inner regions of the ejecta. As photons are released through radioactive decay, they are absorbed by the elements in the outer layers of ejecta, creating absorption troughs in the black body continuum radiating from the surface of the photosphere. In this manner the SN reveals its composition over time from the outside in.

The spectral time series for a normal Type Ia SN is depicted in Figure 1.2. We characterize the spectral epochs in relation to the evolution of the light curve above, and discuss the

spectral properties seen before the light curve reaches maximum brightness (Figure 1.2(a)), at time of peak (Figure 1.2(b)), and during the light curve's decline (Figure 1.2(c)).

The earliest spectra, shown in Figure1.2(a), are defined by a strong continuum littered with P-Cygni profiles of intermediate mass elements (IMEs), a characteristic profile which displays an emission feature at the rest wavelength of a given line and a blueshifted absorption feature. The early spectra also exhibit a strong Ca II absorption feature on the blue side of the spectrum. Line velocities at early times indicate very fast photospheric velocities in the outermost ejecta ranging from around 18,000 up to 25,000 km/s.

As time continues and the light curve reaches peak luminosity the UV becomes suppressed by the optically thick iron group elements (IGEs) present in the inner regions which we can investigate as the photosphere recedes. Spectra taken at this epoch exhibit absorption features from IMEs, such as Si, S, O, and Ca, as well as some IGE absorption features from Co and Fe (Figure 1.2(b)). Line velocities indicate that the typical photospheric velocity during this phase is about 10,000 km/s.

Figure 1.2(c) shows an example spectrum from the post-maximum phase. As the photosphere probes deeper and deeper into the ejecta, the IGE absorption features from elements such as Fe and Co begin to dominate the spectra, IME features fade, and velocities drop off further.

Eventually, as the SN ejecta continues to expand it becomes becomes optically thin throughout and reaches the nebular phase. At this epoch we no longer see absorption features or much of a continuum, but rather emission peaks as the ejecta cools. For Type Ia SNe, the nebular phase typically begins around 150 days post explosion. Figure 1.2(d) shows a typical nebular spectrum of a normal Type Ia SN. It is difficult to obtain nebular spectra of SNe Ia and thus we do not have many examples, however, most of those examples are for normal SNe Ia. These show emission features from the forbidden transitions of [S II], [Fe II], [Fe III], [Ni II], [Co III], and sometimes [Ca II], which act as coolants while the ejecta is thermalized by the radioactive decay of ^{56}Co. Typical velocities at this epoch are around 5,000 km/s.

Diversity

Most SNe Type Ia form a fairly homogeneous group of objects described by the "normal SNe Ia" discussed above; however, there exists an amalgam of thermonuclear objects that deviate from typical SN Ia characteristics (see Taubenberger (2017) for a review). Such physically distinct classes of thermonuclear SNe include: 91T-like SNe Ia (Phillips et al. 1992; Filippenko et al. 1992a), 91bg-like SNe Ia (Filippenko et al. 1992b), and 02es-like SNe Ia (Ganeshalingam et al. 2012)[1]. While these subtypes are not as common as the normal SNe Ia they must be discussed in order to gain a full picture of Type Ia SNe.

[1]Other more peculiar events of probable thermonuclear origin are also found in nature such as "fast-decliners" (Kasliwal et al. 2010; Perets et al. 2011; Drout et al. 2013), SNe Iax (Foley et al. 2013), and Ca-rich transients. See Section 1.3 for a more detailed description of the Ca-Rich transients.

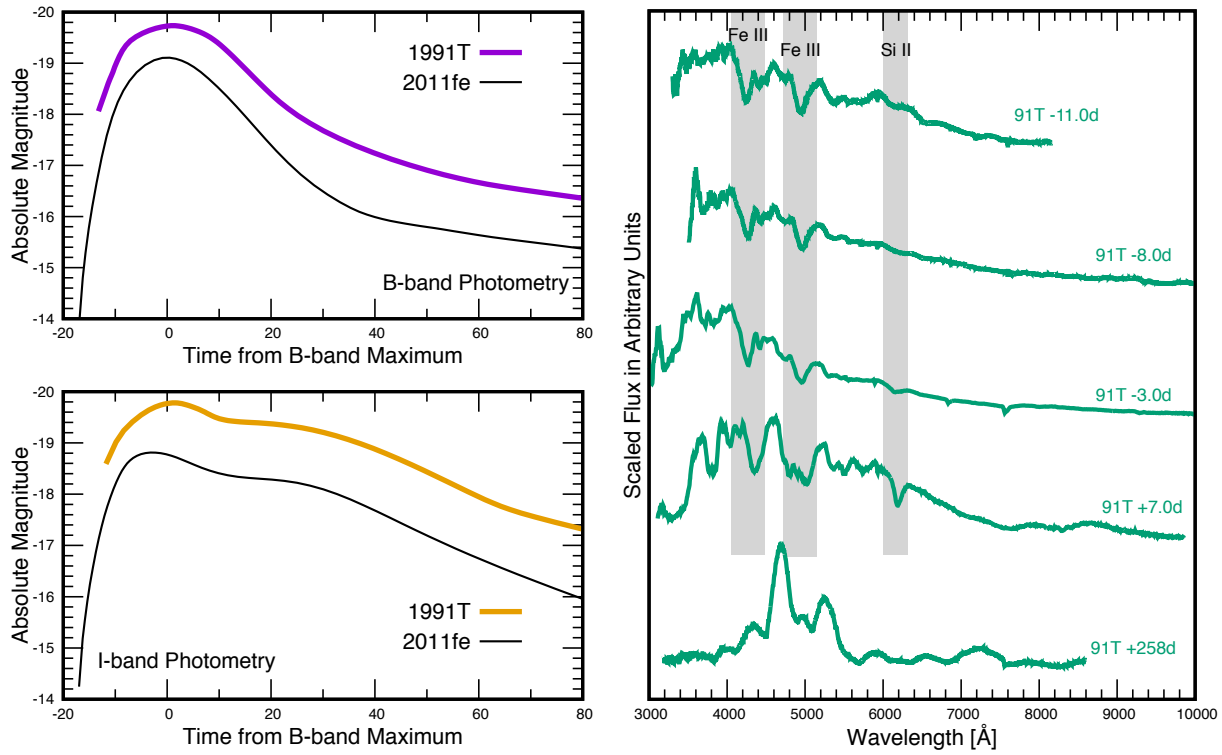

Figure 1.3: Observational properties of the overluminous 91T-like SNe Ia,. Light curves of 91T-like SNe Ia tend to be brighter and decline more slowly than normal SNe Ia. The early spectra are peculiar in that they only exhibit IGE absorption features and lack the IME features present in normal SNe Ia. Light curves taken from Lira et al. (1998), spectra taken from Mazzali et al. (1995), Silverman et al. (2012), Gómez & López (1998), and Filippenko et al. (1992a) via the OSC.

The most luminous events fall into the category of 91T-like SNe Ia, which make up at least 9% of Type Ia SNe (Li et al. 2011b). These exhibit both bright peak magnitudes and broad light curves (typical Δm_{15} are approximately 0.8 mag), and typically have a very strong secondary peak in the NIR (Taubenberger 2017). The pre-max spectra of these objects are also peculiar, exhibiting a nearly featureless continuum with the exception of strong Fe III absorption features, when we would normally expect to see contributions from IMEs like Si II. See Figure 1.3.

On the other luminosity extreme are the subluminous 91bg-like SNe Ia shown in Figure 1.4. These events, which make up about 15% of SNe Ia (Li et al. 2011b), display a wide variation in peak magnitude, ranging from an absolute B-band magnitude of -18 all the way down to -16.5 mag (Taubenberger 2017). They also have very narrow light curves (with typical Δm_{15} around 1.8-2.0 mag (Taubenberger 2017)) which lack a secondary peak in the NIR. The spectra of 91bg-like SNe Ia are also peculiar, exhibiting strong Ti II absorption

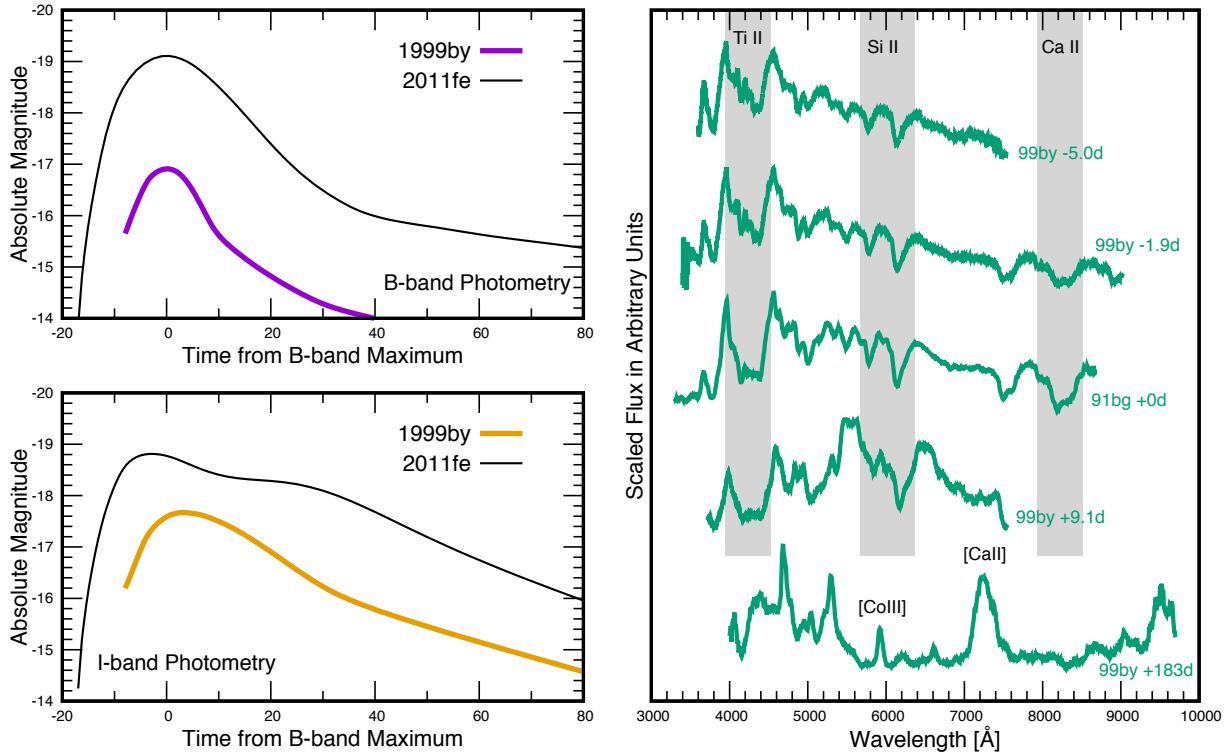

Figure 1.4: Observational properties of the subluminous 91bg-like SNe Ia, featuring SN 1991bg and SN 1999by. Light curves of 91bg's tend to be dimmer and decline more quickly than normal SNe Ia. The early spectra are peculiar in that they show strong Ti II absorption features not typical in normal SNe Ia. The nebular spectra also exhibit a strong [Ca II] feature around 7200 Å. Light curves taken from Silverman et al. (2012), spectra taken from Garnavich et al. (2004), Blondin et al. (2012), Silverman et al. (2012)(99by), and Silverman et al. (2012)(91bg) via the OSC.

features in the photospheric phase and strong [Ca II] emission at nebular times.

Figure 1.5 shows the final and least common subtype, the 02es-like SNe Ia (Ganeshalingam et al. 2012). The 02es-like SNe Ia account for only 5% of SNe Type Ia (Li et al. 2011b). They are also subluminous, however they decline much more slowly than 91bg's, exhibiting typical Δm_{15} of approximately 1.1-1.3 mag (Taubenberger 2017). The characteristics of the different SNe Ia subtypes are summarized in Table 1.1.

When we place the photospheric spectra in order from brightest events to the dimmest we can examine a spectroscopic sequence first noted by Nugent et al. (1995). When the peak spectra of Type Ia SNe are arranged from those events with the brightest peak magnitudes to those with the dimmest the following trends arise. First, and most prominently the ratio of the Si II absorption features becomes larger as we move up the sequence such that for high luminosity events the absorption feature at 5800 Å decreases with respect to the

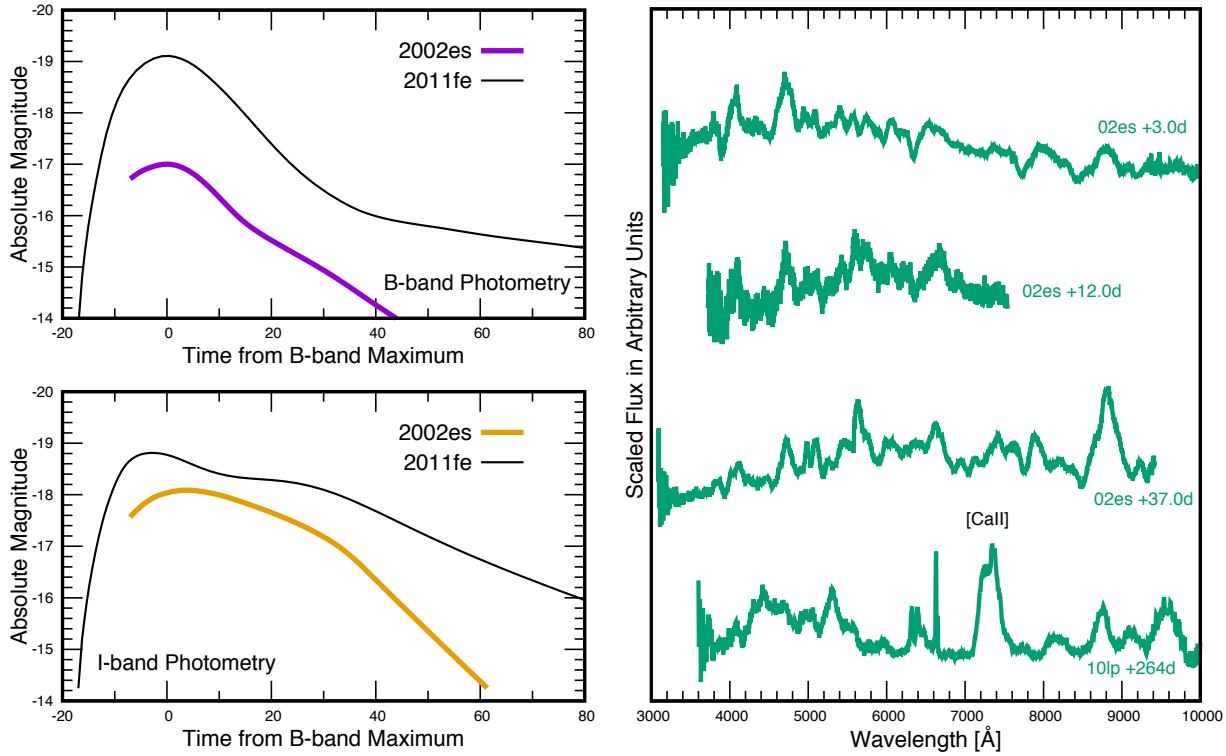

Figure 1.5: Observational properties of the rare 02es-like SNe Ia, featuring SN 2002es and SN 2010lp. Light curves of 02es's tend to be dimmer than normal SNe Ia, but do not decline as quickly as 91bg's. Light curves taken from Ganeshalingam et al. (2012), spectra taken from Ganeshalingam et al. (2010), Blondin et al. (2012)(02es), and Taubenberger et al. (2013)(10lp) via the OSC.

one at 6150 Å. The overall IME absorption features grow weaker for more luminous events, particularly those at 7500 and 8200 Å associated with O I, Mg II, and Ca II. The subluminous 91bg-like SNe Ia start to exhibit strong Ti II troughs near 4200 Å. And, lastly, the relative strengths of the two S II absorption features at 5400 Å varies such that for low luminosity events the red trough is stronger than the blue, but these features become equal around normal SNe Ia and reciprocal for the brightest (91T-like) SNe Ia. Any proposed progenitor for Type Ia SNe must reproduce this sequence of trends in order to remain a viable candidate.

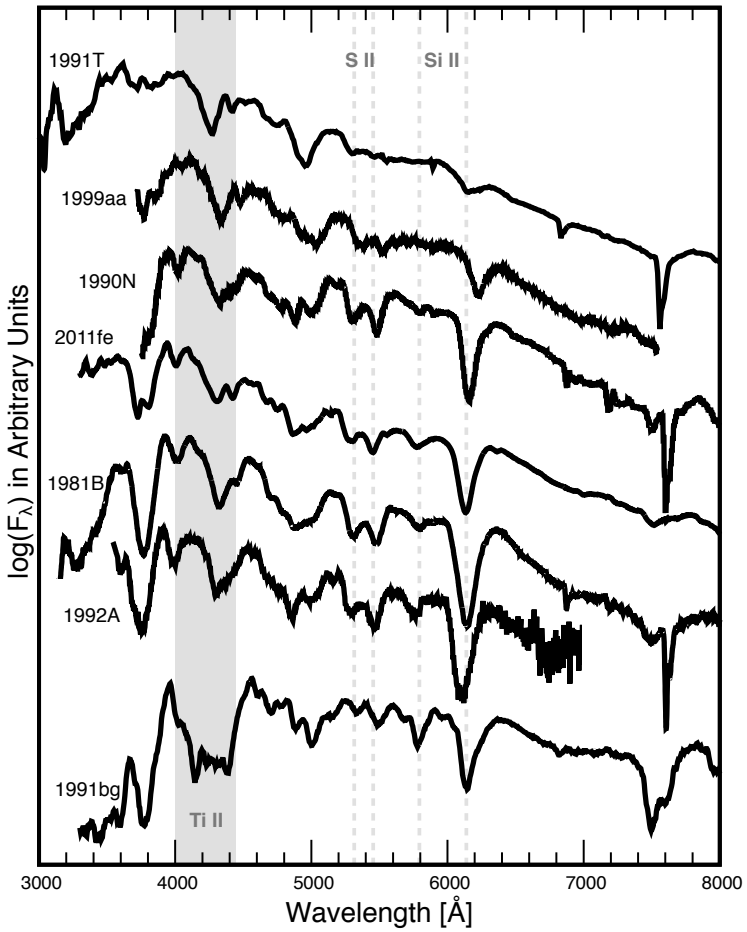

Figure 1.6: The spectral sequence introduced by Nugent et al. (1995) displaying SNe Ia in order from most luminous at the top to lease luminous at the bottom. When arranged in this manner trends in absoprtion features such as Si II and S II arise.

Table 1.1: Summary of the Diversity Amongst Type Ia SNe.

Subtype	M_B range (at time of B-band peak)	Δm_{15} range	Percentage of SNe Ia
Normal SNe Ia	-19.5 to -18.5	0.8 to 1.7	70%
1991T-like SNe Ia	-20.9 to -19.4	0.7 to 1.0	9%
1991bg-like SNe Ia	-18.5 to -16.0	1.7 to 2.1	25%
2002es-like SNe Ia	-18.0 to -17.6	1.1 to 1.3	5%

Note. — All values should be considered approximate. Magnitudes and Δm_{15}s were taken from Taubenberger (2017) and frequencies were taken from Li et al. (2011b).

1.1.2 Theory and Possible Progenitors

Combining the compositional information we glean from observations it is believed that Type Ia SNe likely arise from the thermonuclear explosions of white dwarfs (WDs). However, there are many ways this explosion could come to be.

The original (simplified) picture for how these WDs explode involves the WD gaining mass donated from a binary companion. When the mass of the WD approaches the Chandrasekhar mass limit, it can no longer support itself via electron degeneracy pressure and explodes. However, even this simple picture quickly becomes very complicated.

The first question arises when we consider the binary companion. Here there are two options. In the first the WD accretes material from a non-degenerate companion until the WD explodes. This is known as the single degenerate scenario and in this case the binary companion survives (Whelan & Iben 1973). The other option is for the binary companion to be another degenerate WD. In this double degenerate scenario the two WDs merge, explode, and do not leave behind a surviving companion (Webbink 1984; Iben & Tutukov 1984).

Another possible pathway to a double degenerate situation involves the collision of two WDs that exist in a triple system. This triple system would need to involve two WDs in a binary orbited by another, roughly solar mass, object. It is possible that in a small number of these systems the 3-body gravitational interactions could drive the two WDs into a head-on collision, causing an explosion (Katz & Dong 2012; Kushnir et al. 2013). However, a recent analysis of the WD population in the Gaia database show that the number of WDs in such systems are orders of magnitude too low to explain the frequency of Type Ia SNe (Hallakoun & Maoz 2019). While this scenario could still occur in nature (see for example Dong et al. (2015)) it would have to be exceedingly rare.

After the initial WD ignition there are even more options to consider. It was originally thought that the WD would detonate near its center leading to an immediate thermonuclear runaway (Arnett 1969). It was soon realized, however, that this method burns the whole WD until it reaches nuclear statistical equilibrium (NSE) and the entire ejecta becomes dominated by ^{56}Ni and contains very few IMEs, resulting in a light curve that is too bright and spectra that lack the necessary IME absorption features. It was then suggested that perhaps the WD fully deflagrates rather than ever experiencing a detonation. This, however, results in nearly the opposite problem. There is too little ^{56}Ni synthesized to explain the luminosity of a typical SN Ia and an excess of IMEs is synthesized throughout the ejecta (Mazzali et al. 2007)[2]. The current favored burning mechanism is a combination of the above. First the WD goes through a deflagration phase, burning some of its core. Then a deflagration-detonation transition occurs burning the rest of the WD via thermonuclear runaway (Schmidt et al. 2010). While it is still an open question exactly how this transition occurs, studies have shown that the resulting ejecta is able to explain normal Type Ia SNe (Kasen et al. 2009).

[2]While ruled out as a SN Ia progenitor, the deflagration of a WD is still a possibility for the progenitor of SNe Iax (Foley et al. 2010; Kromer et al. 2013; Fink et al. 2014; Magee et al. 2016).

All of the above methods of exploding a WD occur near the Chandrasekhar mass limit, so that the ejecta mass of a SN Ia remains fairly constant and any variation in observables is caused by varying amounts of ^{56}Ni synthesized in the explosion. This thesis explores an alternative scenario where the progenitor explodes below the Chandrasekhar mass limit. This allows for a variety of ejecta masses to be produced by these explosions as well as a variable mass of ^{56}Ni. Please see Section 1.2 for the discussion on the sub-Chandrasekhar mass progenitor channel.

1.1.3 Importance: SNe Ia and Cosmology

Because of the seemingly reliable relationship between the width of a SN Ia light curve and its peak magnitude it is in principle simple to determine the intrinsic brightness of a Type Ia SN from photometric observations (Phillips 1993). The consequences of this are profound. If we are confident about the intrinsic luminosity of these events, we can use them as our cosmological distance measures or standard candles. With these we can determine the distance to far away galaxies by comparing the absolute magnitude we believe intrinsic of the SN to the observed, apparent, magnitude. The history of standard candels begins in 1912 when Henrietta Leavitt, an astronomer employed as a computer at Harvard College Observatory, discovered the period-luminosity relationship of Cepheid variables (Leavitt & Pickering 1912). Leavitt's discovery directly led to our first standard candles. In 1929 Edwin Hubble used this relationship to determine the distance to nearby galaxies by comparing the observed magnitudes of Cepheid variables to their intrinsic luminosities (Hubble 1929). Cepheid variables are not luminous enough to tell us the distance to anything but very nearby galaxies, so the need for a significantly more luminous standard candle is paramount. Therein lies the importance of Type Ia SNe for cosmology.

By using Type Ia SNe as standard candles to measure the distance to very distant galaxies the Nobel Prize winning discovery of the accelerating expansion of the universe was made by two teams (Riess et al. 1998; Perlmutter et al. 1999). However, in recent years there has been a discrepancy in measured value of the rate of the expansion (the Hubble constant or H_0) as measurements taken with SNe Ia and those taken by measuring the cosmic microwave background (CMB) have diverged. The solution to this quandary is indeterminate but an important piece of the puzzle is a greater understanding of Type Ia SNe. What are the progenitors of these events? Are there multiple progenitor pathways? And how can we tell which SNe Ia are really standardizable?

1.2 Double Detonations of Sub-Chandrasekhar Mass White Dwarfs

Sub-Chandrasekhar mass carbon-oxygen (CO) WDs have been discussed extensively as a possible progenitor for Type Ia SNe. Early studies modeled the explosion of sub-Chandrasekhar

mass CO WDs with a thick shell of accreted helium and found that a detonation in the helium shell can trigger an explosion of the CO core in what was called the "double-detonation model" (Woosley & Weaver 1994; Nomoto 1982b,a; Livne 1990). The helium ignition sends a shock wave into the center of the CO WD causing a detonation near the core of the star followed by thermonuclear runaway. This process has been theorized as a possible path to SNe Type Ia, initially for WDs with large helium shells (Woosley & Weaver 1994; Nomoto 1982a,b; Livne 1990). However, these original, thick shell, models were not good candidates for Type Ia supernovae. The thick helium shells produce too much ^{56}Ni during nuclear burning for this to be a viable progenitor (Hoeflich & Khokhlov 1996; Nugent et al. 1997). The ashes of thick helium shells have also been shown to cause Fe-group line blanketing in the spectra, resulting in peak spectra redder than typical SNe Ia (Nugent et al. 1997; Kromer et al. 2010; Woosley & Kasen 2011). Modern computing has allowed for more detailed studies of the nuclear reactions involved in these explosions, revealing that the minimal mass of a helium shell required to trigger an explosion via a double detonation is much smaller than those used in the early models (Bildsten et al. 2007; Shen & Bildsten 2014; Fink et al. 2007, 2010). Current simulations show that the latter can be a promising path to normal and subluminous SNe Type Ia (Shen et al. 2018a; Polin et al. 2019b; Townsley et al. 2019). The possibility and consequences of such thin helium shell explosions motivate the need to re-examine these progenitors for SNe Ia.

Evidence increasingly points toward sub-Chandrasekhar mass WDs being responsible for a significant portion of SNe Type Ia. This thesis points to a population of SNe Ia distinguished by the relationship between their peak luminosity and Si II velocity as likely candidates for originating from a sub-Chandrasekhar mass double detonation (originally from Polin et al. (2019b)), a delineation that was further supported by the examination of spectropolarimetry measurements of this population in Cikota et al. (2019). Furthermore, newly discovered fast Gaia WDs have been pointed to as the potential surviving companions of a very thin helium shell ignition occurring during a dynamical merger of two WDs, known as the D6 mechanism (Shen et al. 2018b). Here dynamically unstable mass transfer occurs between the two WDs allowing for a small amount of helium to be accreted by the progenitor. This helium then ignites and results in a double detonation explosion shortly before the WDs can merge. This allows for the donor WD to be in close proximity to the explosion resulting in a velocity kick of a few thousand km/s Shen et al. (2018b).

While numerous studies show promising results when comparing double detonation models to SNe Type Ia during the photospheric phase this thesis includes the first comprehensive examination of what these models look like in the nebular phase, when the ejecta becomes fully optically thin (originally Polin et al. (2019a)).

1.2.1 Thick Helium Shell Double Detonations

The upcoming era of all-sky, high cadence transient searches also motivates the consideration of potential rare transients. Polin et al. (2019b) predicted the signatures of double detonation explosions triggered by thick helium shells. This includes a detectable early excess in flux

in the SNe Ia light curves during the first few days after explosion, significant blanketing in the UV and the blue portion of the optical spectra near peak, and a distinct red-to-blue evolution of the optical colors shortly after explosion. All of this excludes these thick helium shell models from being the progenitors of Type Ia SNe. At the time of publication of our models no such events had been detected; however, due to technological advances astronomers at the Zwicky Transient Facility (ZTF) were able to discover SN 2018byg, the first event that clearly displayed all the "smoking gun" features we predicted (De et al. 2019).

The discovery of SN 2018byg (ZFT18aaqeasu) provides strong evidence for a sub-Chandrasekhar mass explosion triggered by a massive helium shell ignition. De et al. (2019) fit this peculiar Type I SN with a model derived from Polin et al. (2019b), concluding that the early flux excess exhibited by SN 2018byg is due to the radioactive decay of elements in the outermost ejecta, produced during the initial helium shell burning. The spectrum at peak brightness was also completely line blanketed for wavelengths less than 5000 Å which is modeled well by optically thick helium shell ashes in the outermost ejecta. See Chapter 5 for a more in depth discussion of this discovery. This event lends credence to the ability of the double detonation scenario to lead to the explosion of a WD, encouraging us to look for the thin helium shell double detonations amongst the population of observed Type Ia SNe.

1.3 Ca-rich Transients

Other rare transients may also relate to WDs accreting helium shells. The helium shell detonation scenario has mainly been employed to model photometric and spectroscopic signatures in SNe Ia (Sim et al. 2010; Kromer et al. 2010; Woosley & Kasen 2011; Polin et al. 2019b; Townsley et al. 2019); however, there exists a wide parameter space within the double-detonation scenario, mainly at the low mass end, that can be used to explain atypical objects.

Ca-rich gap transients, so called because their peak luminosity lives in the "gap" between that of novae and SNe, are a class of astrophysical transients identified by their nebular spectra which are dominated by [Ca II] emission (Perets et al. 2010; Filippenko et al. 2003; Kasliwal et al. 2012). Ca-rich SNe are a particularly heterogeneous group of objects that, like other thermonuclear objects, are thought to arise from a progenitor system containing a WD. These low luminosity events (-14 to -16.5 mag) all exhibit a fast photospheric evolution, rising in about 15 days, with photospheric velocities ranging from 5,000-10,000 km/s. They reach the nebular phase very quickly, in 1-3 months, indicating a small ejecta mass ($\sim$0.5 $M_{\odot}$; Perets et al. 2010; Lunnan et al. 2017). Furthermore, Ca-rich transients tend to occur offset from their host galaxies indicating an origin from an old stellar population (Lunnan et al. 2017). These features compound to make Ca-rich transients hard to find, however they are not uncommon. Currents rate estimates place them from 33-94% as frequent as Type Ia SNe (Frohmaier et al. 2018).

Figure 1.7 shows example spectra of Ca-rich SNe in the photospheric phase (left) and nebular phase (right). While the photospheric spectra of Ca-rich transients are unusually

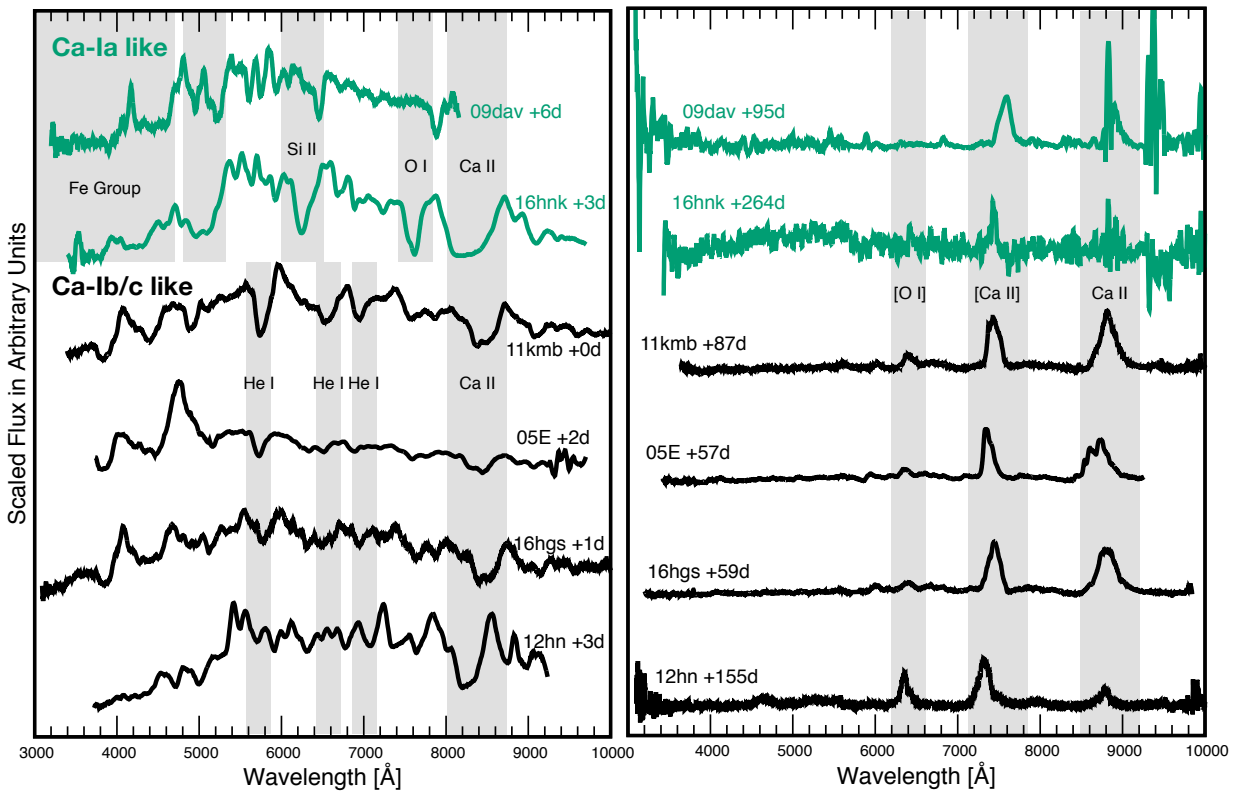

Figure 1.7: Spectra of Ca-rich transients. Ca-Ib/c like events (those that show He in the photospheric spectra) are shown in black and Ca-Ia like events (those that show Si features, but no He) are plotted in green. The left panel shows the population to be highly heterogeneous at peak brightness while the right panel shows the nebular spectra to all be similar, cooling primarily through [Ca II]. Data taken from Jacobson-Galan et al. (2019) with permission of the co-authors.

diverse, they show similarities in the nebular phase. These objects show weak iron line transitions, with [Ca II] emission at 7200 Å being the dominant emission feature. Some Ca-rich transients have detectable [O I] emission in their nebular spectra around 6300 Å, and the defining requirement of the class is an integrated [Ca II]/[O I] flux ratio greater than 2.

Understanding these elusive events is important for a wide variety of fields in astronomy since they potentially produce a significant portion of the Ca in the universe (Frohmaier et al. 2018). Furthermore, owing to the majority of these events occurring significantly offset from their hosts, in old stellar populations, they provide a window into stellar evolution in those environments. Our understanding of these objects has been limited by a small number of observations – only 17 candidates have been published to date (Lunnan et al. 2017). However, surveys like ZTF are primed to expand our current data set dramatically, with an

estimate of over 20 events per year from ZTF alone (Frohmaier et al. 2018).

A variety of progenitor scenarios involving the thermonuclear explosion of a WD have been proposed to explain the peculiar properties of Ca-rich transients and their environments. Accretion-induced collapse (AIC) of a WD into a neutron star (NS) will produce a subluminous explosion. However, the combination of a very rapid rise time (about 1d), high expansion velocities and over production of IMEs makes this an unlikely scenario (Metzger et al. 2009). Similar discrepancies between models and observations also rule out the tidal disruptions of WDs by NSs or stellar-mass black holes (BHs) (Metzger 2012; Margalit & Metzger 2016; Toonen et al. 2018; Zenati et al. 2019a,b). Tidal detonations of a WD by interaction with an intermediate-mass black hole (IMBH) does occur in dense stellar systems, but is difficult to reconcile owing to the lack of observed IMBHs at the locations of Ca-rich transients (Rosswog et al. 2008; MacLeod et al. 2014; Sell et al. 2015).

Given the range of observed properties, a highly promising progenitor channel for peculiar thermonuclear SNe such as Ca-rich transients is the detonation of a low mass WD via the double detonation mechanism. Alternatively, thin helium shell detonations that only partially disrupt the core can result in rapidly evolving, low luminosity explosions often called ".Ia" SNe (Bildsten et al. 2007; Shen et al. 2010). However, the rise-times and ejecta masses produced in .Ia models are so far inconsistent with those of Ca-rich objects.

1.4 Thesis Overview

Modeling these explosions presents many challenges. The hydrodynamical simulations require examining physics from roughly 10^3 cm (scales required to resolve shock fronts) to 10^{10} cm (several expansion scales for the ejecta to reach homology). Furthermore, we need to accurately calculate the energy gains and compositional yields that occur during nuclear burning. To accomplish this, it is necessary to utilize the most state-of-the-art numerical techniques. We use `Castro` Almgren et al. (2010), a massively parallel, compressible hydrodynamics code capable of adaptive mesh refinement (AMR) (Almgren et al. 2010). AMR enables selective high resolution in areas of interest, such as shock fronts and areas of nuclear burning, making it possible to run a global simulation of these explosions over the requisite orders of magnitude.

This thesis is primarily an exploration into the theory of double detonations. Chapter 2 describes the hydrodynamic simulations of double detonation explosions created with `Castro`. These simulations serve as the foundation of this work. In Chapter 3 we begin to examine the observational consequences of this suite of hydro models by performing radiative transport calculations with the Monte Carlo radiative transport code `Sedona` (Kasen et al. 2006). Using `Sedona` under the approximation of local thermal equilibrium (LTE) we produce synthetic light curves and spectra for the double detonation models throughout the photospheric phase. In Chapter 4 we again begin with the suite of hydrodymanic double detonation models and examine their observational consequences, this time in the nebular

phase. In Chapter 6 we discuss what the above exploration has revealed about Ca-rich transients.

The inclusion of radiative transport calculations allows us to examine the observational consequences of the theory we develop. In this manner we take theory, and produce testable predictions that can be compared directly to data. The second half of this thesis is a discussion on the status of observed double detonations and the role of our models in identifying those events. Chapter 5 discusses the discovery of SN 2018byg, the first strong example of a transient which displays all the predicted "smoking gun" signatures of a double detonation triggered by a thick helium shell. Chapter 6 includes the discussion of SN 2016hnk, a peculiar Ca-rich transient which may also be of thick helium shell double detonation origin. SN 2016hnk also serves as our first opportunity to test our model's ability to consistently match an observation both in the photospheric and the nebular phase. In Chapter 7 we discuss how the predicted signatures of double detonations have affected Ia searches and include the most recent rate estimations from the ZTF's infant Ia program. We conclude in Chapter 8 by presenting our preliminary multi-dimensional (multi-D) simulations of double detonation explosions. We discuss the future direction of this field and what questions these multi-D simulations will help us to resolve.

Chapter 2

Hydrodynamical Simulations of Double Detonation Explosions

The content of this chapter is drawn from Polin et al. (2019b), with permission from the co-authors.

We begin by presenting a numerical parameter survey of sub-Chandrasekhar mass WD explosions that serves as the foundation of this thesis. As in previous studies we show how the ignition of a helium shell can either directly ignite the WD at the core-shell interface ("edge-lit" explosions) or propagate a shock wave into the the core causing a central ignition ("double detonation" explosions). Here we examine the explosions of WDs from 0.6 - 1.2 $M_\odot$ with helium shells of 0.01, 0.05 and 0.08 $M_\odot$. In this chapter we describe our survey of hydrodynamical explosion models. The numerical setup used to simulate the explosion from the helium detonation through homology is described in Section 2.1. The hydrodynamic outflow and elemental yields synthesized from nuclear burning are discussed in Section 2.2. In Chapter 3 we describe the synthetic observables created with these models and discuss the results in the context of type Ia SNe.

2.1 Numerical Methods

We model the explosion in several stages. First, the initial model is built by starting with a bare, isothermal WD progenitor. Next, a helium shell of some mass is added iteratively to the outermost layers of the WD, modelling the accretion of this mass slowly from a companion. During each step of this process the new progenitor is evolved to hydrostatic equilibrium to determine a stable central density of the WD. After the shell reaches a desired mass and equilibrium is achieved, burning is initiated within the helium layer. The resulting thermonuclear hydrodynamics are then evolved in 1-D. Each model is evolved until the ejecta reaches homologous expansion, after which we perform radiative transport calculations to produce light curves and spectra for each model.

2.1.1 Initial Models and Parameter Space

The initial models were created by the process described in Zingale et al. (2013). Each model begins with an isothermal WD of a desired mass which is 50% carbon and 50% oxygen. The WD profile is then augmented with an isentropic helium shell on its surface. We use MAESTRO, a low Mach number hydrodynamics code (Zingale et al. 2018; Nonaka et al. 2010), to build the model profile and ensure it begins in hydrostatic equilibrium. This checks that our choice of central density of the WD is appropriate to support the additional mass of the helium shell. In the process of finding an equilibrium solution, a mixed transition layer is introduced between the CO WD and the helium layer. The purpose of this mixed region is to ensure there is no discontinuous change in composition. For most models this mixed region is resolved over 128 grid cells at the coarsest level of refinement. When the width of this layer is increased the nucleosynthetic yields from the core of the white dwarf show no difference and the yields from the helium shell are similar to igniting the helium at an equivalently larger radius above the white dwarf (see table 2.3).

This parameter survey varies the mass of the white dwarf (M_{WD}), the mass of the helium shell (M_{He}), the amount of material confined in the mixed region between the WD and the helium shell (δ), and the location of the initial helium ignition (R_{ign}). The WD mass ranges from 0.6-1.2 $M_\odot$, in increments of 0.1 $M_\odot$, and the helium shell mass takes on the values 0.08, 0.05 and 0.01 $M_\odot$. Additional WD/He mass combinations of interest were explored less systematically. See table 2.2 for the comprehensive set of the 47 models explored in this survey as well as their conditions at the location of ignition.

2.1.2 Hydrodynamics and Nuclear Processes

The compressible Eulerian hydrodynamics code Castro is used to follow the progression of the explosions. Castro allows for adaptive mesh refinement (AMR) which enables the selective increase of resolution in areas of interest in the simulation; specifically, in areas where nuclear burning is active (Zingale et al. 2018; Almgren et al. 2010). Our simulations begin with a cell size of order 10^5 cm. Each simulation is allowed 4 levels of refinement, with each refinement level increasing the resolution by a factor of 4, resulting in a minimal resolution of order 10^3 cm.

We enable Castro's built-in monopole gravity and the Helmholtz equation of state (Timmes & Swesty 2000). A 13 isotope α-chain nuclear network is used to monitor the nuclear reactions (Timmes 1999). The network includes (α,γ) and (γ, α) reactions for 13-isotopes: ^{4}He, ^{12}C, ^{16}O, ^{20}Ne, ^{24}Mg, ^{28}Si, ^{32}S, ^{36}Ar, ^{40}Ca, ^{44}Ti, ^{48}Cr, ^{52}Fe, and ^{56}Ni. For temperatures above 2.5×10^9K, (α,p)(p,γ) reactions (and their inverse reactions) are included for 8 additional isotopes: ^{27}Al, ^{31}P, ^{35}Cl, ^{39}K, ^{43}Sc, ^{47}V, ^{51}Mn, and ^{55}Co.

Several additional calculations were performed with a larger reaction network consisting of 21 isotopes. The 21 isotope network includes all of the reactions in the 13 isotope network (including those additional reactions for temperatures above 2.5×10^9K) as well as ^{1}H, ^{3}He, ^{14}N, ^{56}Cr, ^{54}Fe, and ^{56}Fe. These additional isotopes allow for the distinction of iron group

elements toward the end of the α-chain in more detail, with the presence of three more radioactive isotopes. In the examples considered, the larger network did not yield significantly different results and it was determined that the 13 isotope network was sufficient for the scope of this study.

2.1.3 Ignitions and Explosion Mechanisms

After an initial model is shown to have reached an equilibrium state it is imported into Castro where the remaining hydrodynamics calculations are performed. A radius is chosen at which to trigger an ignition in the helium layer by heating a single grid cell in the coarsest level of refinement (order 10^5 cm). Once nucleosynthesis is initiated, all artificial heating is turned off. We run each simulation from the time of this initial helium ignition, through all of the nucleosynthetic burning, and until the ejecta reaches homologous expansion (when the velocity field is constant with time and proportional to radius: $v = r/t$).

There are two promising paths to explosion for these sub-Chandrasekhar mass WDs. In the double detonation scenario, the ignition of the helium shell sends a shock wave into the CO WD igniting the WD at the center of its core (Woosley & Weaver 1994; Nomoto 1982b,a). The second scenario is known as the direct-dive or edge-lit detonation, where the ignition of the helium shell directly ignites the CO WD at its interface with the helium shell (Shen & Bildsten 2014; Moll & Woosley 2013). Progenitors modeled in this study exhibit both ignition mechanisms depending on the properties (density, temperature and pressure) of the ignition site within the helium shell.

Models are initially ignited at the base of the convective region in the helium shell. This is a natural choice because it is likely where the helium reaches the highest temperature and pressure while still under hydrostatic equilibrium. Both edge-lit explosions and traditional double detonations occur. It has been shown that an edge-lit explosion modeled in 1-D are qualitatively similar to a double detonation of the same progenitor (Woosley & Kasen 2011) but it is expected that this degeneracy will break down in higher dimensional studies. Given the 1-D nature of this study, we choose to focus on the double detonations, which are likely to have fewer asymmetries moving into higher dimensions than their edge-lit counterparts.

After examining the initial parameter space of models, further choices for ignition location were explored. It is possible to ignite the edge-lit models as double detonations, by igniting the helium at a location of lower temperature, pressure and density (or a larger radius) within the shell. After examining all of the results where models were ignited at the interface between the WD and the shell, each of the initial models that led to an edge-lit explosion was re-ignited at a minimal radius required to produce a double detonation explosion (see tables 2.2 and 2.3).

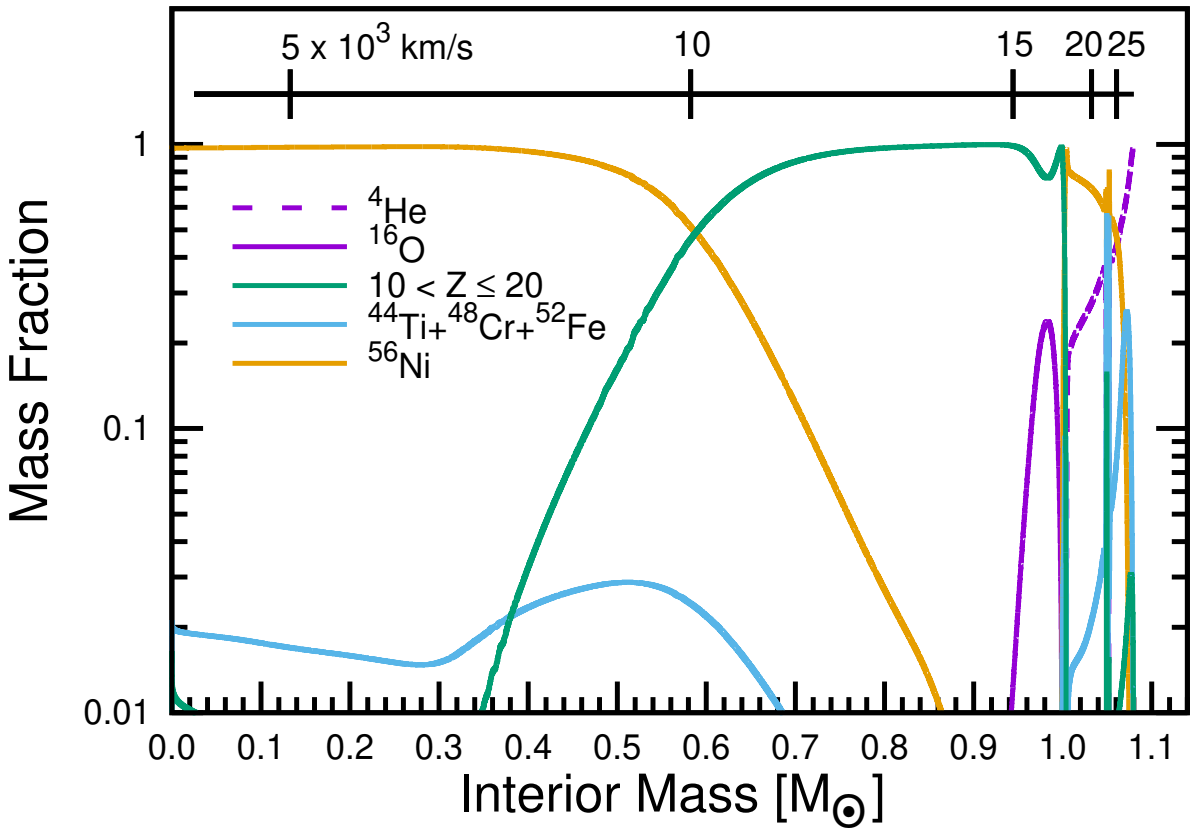

Figure 2.1: Elemental composition of the supernova ejecta as a function of interior mass for a 1.0 $M_\odot$ WD with a 0.08 $M_\odot$ helium shell that has reached homology. The mass fractions ^{4}He (dashed) and ^{16}O (solid) are shown in purple. Summed mass fractions of intermediate mass elements (IMEs) ($10 < Z < 22$) in green, radioactive material of $22 \leq Z < 28$ in blue, and ^{56}Ni is shown in yellow. ^{12}C is almost completely burnt in this model with a mass fraction of never reaching above 10^{-4}. The bar on top of the figure indicates the ejecta velocity in increments of 5000 km/s. Everything for an interior mass greater than 1.0 $M_\odot$ is synthesized from the burnt helium shell and everything less than 1.0 $M_\odot$ is from the underlying WD. This is one of the heaviest shells modelled in this paper, so a large amount of radioactive material is produced from the shell.

2.2 Nucleosynthetic Yields

This section examines the nucleosynthesis yields of the explosion models. First, the overall composition of the material produced is investigated. Next, the composition of the fastest ejecta is examined. This outermost material, which is created from the burning of the helium shell, dominates the early light curve and spectral features, imprinting a characteristic signature on the observed transient. Underneath the ashes of the helium shell the ejecta looks more like a standard thermonuclear WD explosion. The α-chain burning becomes more complete when burning occurs at higher density, temperature and pressure. Thus, the center of the ejecta is composed of mainly heavy, radioactive material, while intermediate mass and lighter elements are present further out (see Figure 2.1 for an example from a thick helium shell model).

2.2.1 Overall Nucleosynthetic Yields

Figure 2.2 shows the total abundances produced by models ignited at the interface between the helium shell and the CO WD. As the total mass of the initial model increases, so does its central density, temperature and pressure. As burning occurs the more massive models burn more completely through the α-chain network, and heavier elements are created. Specifically the amount of ^{56}Ni produced is significantly larger for models with a total mass above 0.9 $M_\odot$, reaching the quantities required to power SN Ia-like brightness through radioactive decay. Details on the energetics of the explosions can be found in Table 2.1.

It is difficult to compare these results directly with literature as there has been no other 1D double detonation study performed with a large suite of models. We do however, compare our closest matched models to the results of the four previous studies which come closest to our approximations: the 1D simulations of bare sub-Chandrasekhar mass WDs (those with no helium shell) in Sim et al. (2010) and Shen et al. (2018a), the 2D double detonation simulations in Fink et al. (2010) and the 3D rotating WDs modeled in García-Senz et al. (2018).

From a qualitative standpoint our results are in line with expectations from these previous studies which have established a relationship between ^{56}Ni and total mass of the system. Our ^{56}Ni yields in this study show close agreement to the amount of ^{56}Ni produced as a function of total mass to the bare sub-Chandrasekhar mass WDs (those with no helium shell) in Sim et al. (2010). However, more recent studies of these bare WDs in Shen et al. (2018a) show significantly more ^{56}Ni than produced in our study for the lower-mass models. The bare 0.9 $M_\odot$ model produced a factor of 2 more ^{56}Ni than the 0.9 $M_\odot$ WD with a 0.01 $M_\odot$ helium shell in this study. Our models also show similar yields to the traditional 2D double detonation explosions modeled in Fink et al. (2010) and the 3D rotating WDs modeled in García-Senz et al. (2018) when examining the amount of ^{56}Ni produced from the underlying WD. For example the Fink et al. (2010) 0.92 $M_\odot$ WD with a 0.084 $M_\odot$ helium shell produces 0.34 $M_\odot$ ^{56}Ni in the core, and the 0.9 $M_\odot$ WD with a 0.08 $M_\odot$ helium shell in this study produces

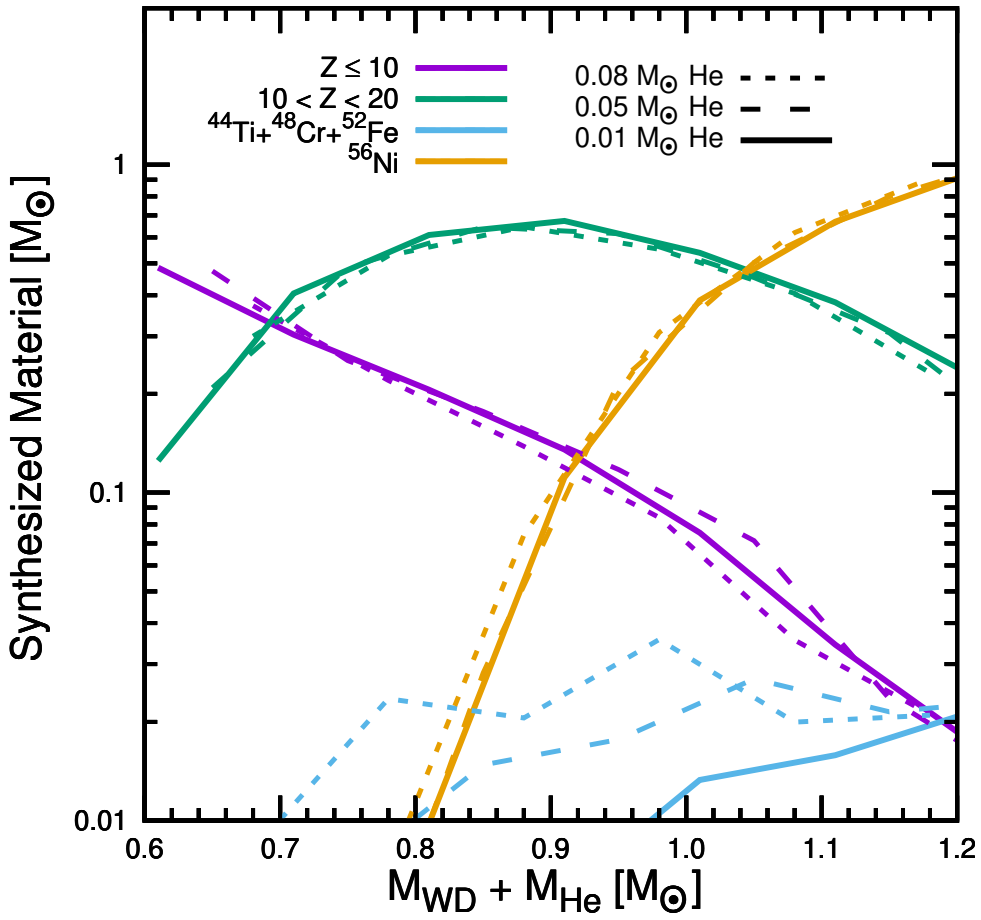

Figure 2.2: Nucleosynthesis yields for models ignited at the interface between the helium shell and the CO WD. Models with the same mass helium shell are connected with lines of the same dash type (solid line for 0.01 $M_\odot$ He, long dashes for 0.05 $M_\odot$ He, and short dashes for 0.08 $M_\odot$ He). Summed masses of elements produced with $Z \leq 10$ (mostly ^{16}O) are shown in purple, IMEs ($10 < Z < 22$) in green, radioactive material of $22 \leq Z < 28$ in blue, and ^{56}Ni is shown in yellow. As the central density of the progenitor increases, nuclear burning completes more of the α-chain network producing heavier elements. Models whose total mass exceeds 0.9 $M_\odot$ produce ^{56}Ni in quantities required to power normal SN Ia-like light curves.

0.31 $M_\odot$ ^{56}Ni in the core, and our 1.1 $M_\odot$ WD with a 0.05 $M_\odot$ model produces only 10% more ^{56}Ni than the García-Senz et al. (2018) 1.1$M_\odot$ WD with 0.052 $M_\odot$ helium.

It is unclear why the Shen et al. (2018a) results differ so strongly from the rest of the literature. A post-processing technique is used to determine the nucleosynthetic yields, which could explain the difference between the ^{56}Ni produced in Fink et al. (2010) and García-Senz et al. (2018) as well as our own which all calculate the nucleosynthesis concurrent with the hydrodynamics. However, this does not explain the divergence between the Shen et al. (2018a) and the Sim et al. (2010) results which employ a similar post-processing correction. It is possible that these differences occur from the computational resolution. The Shen et al. (2018a) models have a resolution of $\sim 10^4$ cm while ours are resolved to an order of magnitude finer resolution on burning fronts. However, again this does not explain the difference between their results and those in Sim et al. (2010) which have a resolution of order 10^6 cm.

There are also a number of physical differences between the bare WD simulations (Sim et al. 2010; Shen et al. 2018a) and the double detonations performed in this study, which makes it difficult to isolate what causes the differences in yields. For example, the fact that the initial conditions initiate burning at the core of the WD, differs from the helium shell ignition in a double detonation, which results in an inward shock that compresses the core before detonation. In the future it would be prudent to perform a systematic comparison study which has closer initial conditions to Shen et al. (2018a) to determine the source of the discrepancy.

2.2.2 Outermost Ejecta: Material Produced from the Helium Shell

A distinct feature of a sub-Chandrasekhar mass WD explosion is the presence of heavy, radioactive material in the outermost ejecta, a result of the burning of the initial helium shell. Figure 2.3 shows the amount of radioactive material produced from the burnt helium shell compared with the overall radioactive material produced. The amount of radioactive material produced during helium burning is a function of the density and temperature profile of the shell, which is is a function of both the mass of the helium shell and the mass of the underlying WD. For the same WD, the heavier the helium shell the more radioactive material is produced on the surface of the explosion. Thin helium shells do not produce a significant amount of radioactive material in the outermost ejecta on any of the WDs explored in this study.

As this material decays it creates an excess flux in the early observed light curves not present in traditional Chandrasekhar mass WD explosions. The presence of this material is the primary distinguishing factor between sub-Chandrasekhar and Chandrasekhar mass explosions. Figure 2.3 shows that in thick shell models with a total mass less than 0.9 $M_\odot$ a significant fraction of the total radioactive material produced is synthesized in the helium shell. In Chapter 3 we discuss the effect of this radioactive material on the light curves of the thick shell models.

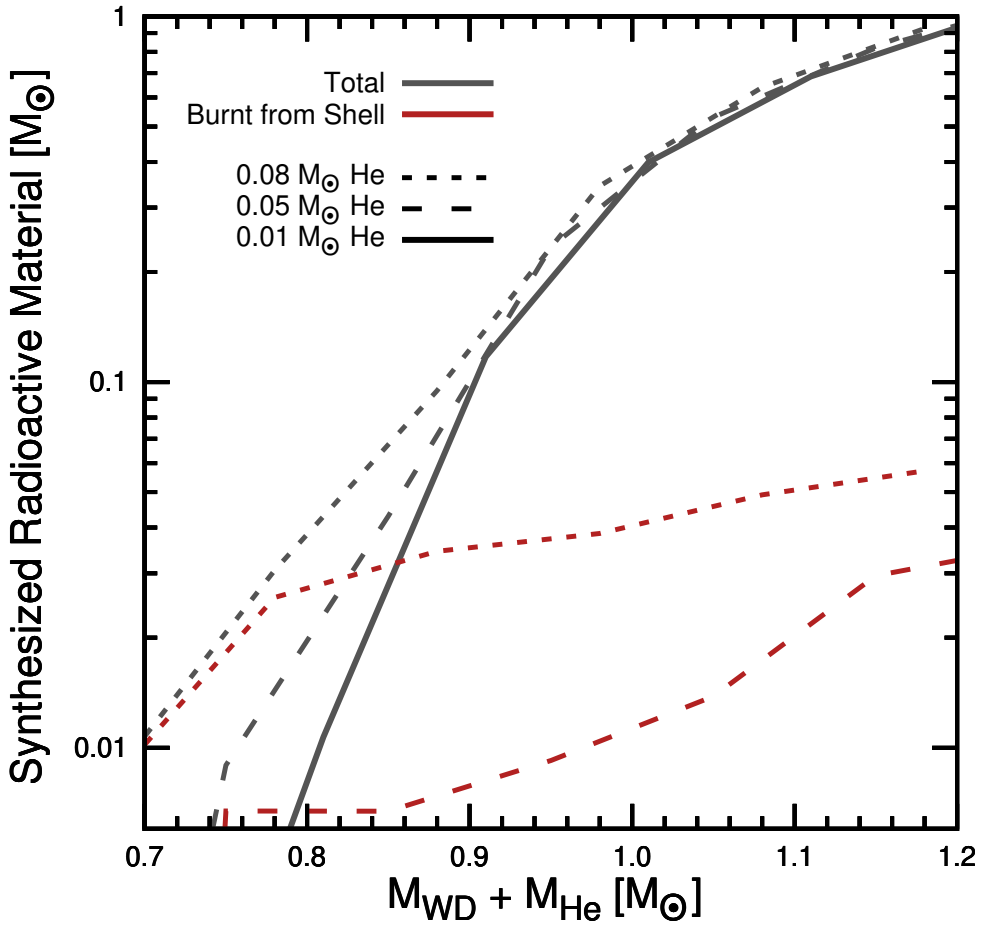

Figure 2.3: The total radioactive material produced (grey) compared with the summed mass of radioactive material burnt from the helium shell (red). Solid lines are models with 0.01 $M_\odot$ He, long dashes have 0.05 $M_\odot$ He, and short dashes 0.08 $M_\odot$ He. Models with 0.01 $M_\odot$ helium shells produce less than 0.003 $M_\odot$ of radioactive material in their outermost ejecta and are not plotted. For models with a total mass less than 0.9 $M_\odot$ the amount of radioactive material produced in the outermost ejecta is comparable to the total radioactive material produced. Observable signatures of this heavy, radioactive material present in the outermost ejecta are discussed in Chapter 3

2.3 Discussion

The most serious approximation in this method is that the simulations are performed in 1-dimension. Previous studies in both two (Fink et al. 2007, 2010; Moll & Woosley 2013) and three dimensions (Moll & Woosley 2013; García-Senz et al. 2018) have shown that double detonation ignitions still occur robustly when multidimensional effects and multiple helium ignitions are considered. Determining the precise values of nucleosynthetic yields will necessitate multi-dimensional simulations with large nuclear networks. However, the advantage of our 1D simulations is that they enable large parameter surveys which can map out the landscape of all possible sub-Chandrasekhar mass explosions and elucidate clear qualitative trends.

There is some discrepancy when comparing our yields from the burnt helium shell to those in the literature. The 1D approximation in our models likely results in more complete shell burning than occurs in nature. Multi-D models show that the helium burns most completely around the initial ignition, but less completely as the burning front travels around the shell (Moll & Woosley 2013). This is the case for the models in Fink et al. (2010) (2D) and García-Senz et al. (2018) (3D) which produce 10 times less ^{56}Ni than our comparable helium shells. However, we show better agreement with the 3D models of burning helium shells in Moll & Woosley (2013) which only produce 20% less ^{56}Ni in the shells than our models. Therefore the amount of radioactive material produced during helium burning in the 1D models should be treated as upper limits to what will occur in nature. We do note that all of the compared models show close agreement in the summed masses of other radioactive material ($Z \geq 22$ not including ^{56}Ni) produced by the helium shells. The exact yields burnt from these shells remains an open question which should be examined in future multi-dimensional studies with careful consideration of the nucleosynthesis of helium and a realistic modeling of shell density profiles expected from accretion.

These hydrodynamic models serve as the foundation of this exploration. Throughout this thesis we take the ejecta models produced in Polin et al. (2019b) (and similar models created beyond the original parameter space using the same methods outlined above) and perform radiative transport calculations in order to examine the observational consequences of double detonation explosions.

Table 2.1: Total Kinetic Energy of the Double Detonation Explosion Models

M_{WD} $[M_\odot]$	0.01 $M_\odot$ He shells	0.05 $M_\odot$ He shells	0.08 $M_\odot$ He shells
0.7	4.6e50	5.6e50	7.0e50
0.8	6.8e50	7.6e50	9.4e50
0.9	8.7e50	9.6e50	1.1e51
1.0	1.1e51	1.2e51	1.4e51
1.1	1.3e51	1.5e51	1.6e51
1.2	1.5e51	1.7e51	1.8e51

Note. — All energies are given in units of $ergs$.

Table 2.2: Model Parameters

M_{WD} [$M_\odot$]	M_{He} [$M_\odot$]	type	δ [cm]	ρ_c [g/cm^3]	R_{ign} [cm]	P_{ign} [$dyne/cm^2$]	ρ_{ign} [g/cm^3]
0.60	0.010	◯	5e06	3.8e06	7.7e08	2.0e20	1.5e04
0.70	0.010	◯	5e06	6.5e06	7.0e08	3.5e20	2.7e04
0.80	0.010	◯	5e06	1.1e07	6.3e08	6.1e20	4.4e04
0.85	0.010	◯	5e06	1.5e07	6.0e08	8.0e20	5.6e04
0.90	0.010	◯	5e06	2.0e07	5.6e08	1.0e21	7.2e04
1.00	0.010	◯	5e06	3.6e07	5.0e08	1.7e21	1.1e05
1.10	0.010	◯	5e06	7.3e07	4.3e08	3.0e21	1.8e05
1.20	0.010	◯	5e06	1.8e08	3.5e08	5.7e21	2.9e05
1.00	0.020	◯	5e06	3.8e07	4.7e08	4.5e21	2.4e05
0.85	0.025	◯	5e06	1.6e07	5.6e08	2.7e21	1.6e05
1.00	0.030	◯	5e06	4.1e07	4.5e08	8.3e21	3.8e05
1.00	0.040	◯	5e06	4.4e07	4.3e08	1.3e22	5.3e05
0.95	0.045	◯	5e06	3.2e07	4.6e08	1.2e22	4.9e05
0.60	0.050	◯	5e06	4.5e06	6.6e08	1.9e21	1.2e05
0.70	0.050	◯	5e06	7.8e06	6.0e08	3.3e21	1.9e05
0.80	0.050	◯	5e06	1.4e07	5.4e08	5.9e21	3.0e05
0.90	0.050	◯	5e06	2.5e07	4.8e08	1.1e22	4.6e05
0.92	0.050	◯	5e06	2.8e07	4.7e08	1.2e22	4.9e05
0.94	0.050	◯	5e06	3.1e07	4.6e08	1.3e22	5.2e05
0.95	0.050	◯	5e06	3.3e07	4.5e08	1.4e22	5.5e05
0.96	0.050	◯	5e06	3.6e07	4.4e08	1.5e22	5.9e05
1.00	0.050	◯	5e06	4.7e07	4.2e08	1.9e22	6.9e05
1.00	0.050	◯	1e07	4.7e07	4.2e08	1.9e22	6.9e05
1.00	0.050	◯	5e06	4.7e07	4.6e08	5.3e21	3.1e05
1.10	0.050	◯	5e06	1.0e08	3.7e08	1.9e22	7.4e05
1.10	0.050	◯	5e06	1.0e08	3.8e08	1.3e22	5.7e05
1.10	0.050	★	5e06	1.0e08	3.5e08	3.8e22	1.1e06
1.20	0.050	◯	5e06	2.7e08	3.1e08	1.9e22	7.7e05
1.20	0.050	★	5e06	2.7e08	2.8e08	9.3e22	2.1e06
0.95	0.055	◯	5e06	3.4e07	4.4e08	1.6e22	6.3e05
1.00	0.060	◯	5e06	5.0e07	4.1e08	1.9e22	7.2e05
1.00	0.070	◯	5e06	5.3e07	4.1e08	1.9e22	7.4e05
0.60	0.080	◯	5e06	5.2e06	6.1e08	4.2e21	2.3e05
0.70	0.080	◯	5e06	9.1e06	5.5e08	7.5e21	3.6e05
0.80	0.080	◯	5e06	1.6e07	4.9e08	1.3e22	5.4e05
0.90	0.080	◯	5e06	2.9e07	4.5e08	1.9e22	7.2e05
0.90	0.080	★	5e06	2.9e07	4.4e08	2.4e22	8.1e05
1.00	0.080	◯	5e06	5.7e07	4.1e08	1.9e22	7.5e05
1.00	0.080	★	5e06	5.7e07	3.8e08	4.6e22	1.3e06
1.10	0.080	◯	5e06	1.3e08	3.5e08	1.9e22	7.7e05
1.10	0.080	★	5e06	1.3e08	3.1e08	9.6e22	2.1e06
1.20	0.080	★	5e06	4.0e08	2.4e08	2.7e23	4.4e06
1.00	0.090	◯	5e06	6.1e07	4.0e08	1.9e22	7.5e05
0.70	0.100	◯	5e06	1.0e07	5.2e08	1.2e22	4.9e05
1.00	0.100	◯	5e06	6.6e07	4.0e08	1.9e22	7.6e05
1.10	0.100	◯	5e06	1.6e08	3.4e08	1.9e22	7.8e05
1.20	0.100	◯	5e06	5.4e08	2.6e08	1.9e22	8.0e05

Note. —
R_{ign}, P_{ign} and ρ_{ign} denote the conditions of the initial model at the location of the helium ignition.
A ◯ indicates a double detonation while a ★ indicates an edge-lit ignition.

Table 2.3: Nucleosynthetic Yields.

M_{WD} [$M_\odot$]	M_{He} [$M_\odot$]	type	M_{tot} $Z \leq 10$ [$M_\odot$]	M_{tot} IME [$M_\odot$]	M_{tot} $Z \geq 22$ [$M_\odot$]	M_{tot} ^{56}Ni [$M_\odot$]	M_{shell} $Z \leq 10$ [$M_\odot$]	M_{shell} IME [$M_\odot$]	M_{shell} $Z \geq 22$ [$M_\odot$]	M_{shell} ^{56}Ni [$M_\odot$]
0.60	0.010	◯	4.8e-01	1.2e-01	4.5e-07	7.2e-08	9.8e-03	3.8e-04	5.1e-12	1.3e-12
0.70	0.010	◯	3.0e-01	4.0e-01	6.5e-04	5.5e-04	8.9e-03	1.0e-03	9.5e-09	1.2e-12
0.80	0.010	◯	2.1e-01	6.1e-01	1.1e-02	9.8e-03	8.0e-03	1.9e-03	5.5e-05	3.1e-12
0.85	0.010	◯	1.5e-01	6.7e-01	3.6e-02	3.3e-02	7.2e-03	2.5e-03	2.7e-04	5.2e-11
0.90	0.010	◯	1.4e-01	6.7e-01	1.2e-01	1.1e-01	6.2e-03	3.1e-03	6.6e-04	6.2e-09
1.00	0.010	◯	7.5e-02	5.4e-01	4.0e-01	3.9e-01	6.1e-03	3.5e-03	3.7e-04	1.1e-07
1.10	0.010	◯	3.4e-02	3.8e-01	6.9e-01	6.7e-01	6.0e-03	3.5e-03	5.1e-05	1.3e-07
1.20	0.010	◯	1.7e-02	2.3e-01	9.6e-01	9.4e-01	2.0e-03	4.1e-03	3.8e-03	2.8e-05
1.00	0.020	◯	7.0e-02	5.3e-01	4.2e-01	4.1e-01	1.2e-02	1.7e-03	5.8e-03	1.5e-03
0.85	0.025	◯	1.4e-01	6.7e-01	5.9e-02	5.2e-02	1.9e-02	1.7e-03	3.9e-03	1.7e-05
1.00	0.030	◯	6.6e-02	5.1e-01	4.6e-01	4.4e-01	1.7e-02	1.9e-03	1.1e-02	6.4e-03
1.00	0.040	◯	6.2e-02	4.9e-01	4.9e-01	4.7e-01	2.0e-02	2.4e-03	1.8e-02	1.2e-02
0.95	0.045	◯	8.0e-02	5.6e-01	3.6e-01	3.4e-01	2.4e-02	1.6e-03	1.9e-02	1.2e-02
0.60	0.050	◯	4.7e-01	2.1e-01	6.7e-05	2.3e-05	5.0e-02	7.1e-06	2.0e-11	5.0e-12
0.70	0.050	◯	2.5e-01	4.9e-01	9.0e-03	2.0e-03	3.6e-02	6.7e-03	6.7e-03	3.1e-06
0.80	0.050	◯	1.8e-01	6.4e-01	4.3e-02	2.8e-02	4.1e-02	1.9e-03	6.7e-03	9.4e-05
0.90	0.050	◯	1.2e-01	6.2e-01	2.3e-01	2.2e-01	4.0e-02	9.9e-04	9.2e-03	2.5e-03
0.92	0.050	◯	9.1e-02	5.9e-01	2.9e-01	2.7e-01	2.7e-02	1.6e-03	2.1e-02	1.2e-02
0.94	0.050	◯	8.2e-02	5.6e-01	3.5e-01	3.3e-01	2.6e-02	2.5e-03	2.1e-02	1.3e-02
0.95	0.050	◯	7.8e-02	5.4e-01	3.8e-01	3.6e-01	2.6e-02	1.9e-03	2.2e-02	1.4e-02
0.96	0.050	◯	7.4e-02	5.3e-01	4.1e-01	3.9e-01	2.5e-02	1.4e-03	2.3e-02	1.5e-02
1.00	0.050	◯	6.7e-02	4.5e-01	5.3e-01	5.0e-01	2.6e-02	8.0e-03	1.6e-02	2.3e-03
1.00	0.050	◯	4.9e-02	4.7e-01	5.3e-01	5.1e-01	2.1e-02	3.7e-03	2.5e-02	1.9e-02
1.00	0.050	◯	5.0e-02	4.7e-01	5.3e-01	5.1e-01	2.1e-02	1.9e-03	2.6e-02	2.2e-02
1.10	0.050	◯	2.4e-02	3.1e-01	8.2e-01	8.0e-01	1.9e-02	1.7e-03	3.0e-02	2.6e-02
1.10	0.050	◯	1.9e-02	3.1e-01	8.3e-01	8.1e-01	1.7e-02	1.4e-03	3.1e-02	3.0e-02
1.10	0.050	★	6.4e-02	2.4e-01	8.5e-01	8.3e-01	1.9e-02	1.9e-03	2.9e-02	2.1e-02
1.20	0.050	◯	1.3e-02	1.5e-01	1.1e00	1.1e00	1.3e-02	8.7e-04	3.6e-02	3.5e-02
1.20	0.050	★	1.4e-02	1.3e-01	1.1e00	1.1e00	1.4e-02	9.0e-04	3.5e-02	3.3e-02
0.95	0.055	◯	7.7e-02	5.3e-01	4.0e-01	3.7e-01	2.7e-02	2.1e-03	2.6e-02	1.2e-02
1.00	0.060	◯	5.3e-02	4.4e-01	5.7e-01	5.4e-01	2.5e-02	2.8e-03	3.2e-02	1.7e-02
1.00	0.070	◯	4.3e-02	4.2e-01	6.0e-01	5.8e-01	2.7e-02	2.7e-03	4.0e-02	3.4e-02
0.60	0.080	◯	3.7e-01	3.0e-01	8.3e-03	1.4e-04	5.9e-02	1.2e-02	8.1e-03	1.2e-07
0.70	0.080	◯	2.2e-01	5.3e-01	3.1e-02	7.1e-03	4.8e-02	6.3e-03	2.6e-02	2.7e-03
0.80	0.080	◯	1.4e-01	6.5e-01	9.5e-02	7.4e-02	4.1e-02	4.0e-03	3.4e-02	1.7e-02
0.90	0.080	◯	8.4e-02	5.5e-01	3.4e-01	3.1e-01	3.6e-02	5.3e-03	3.9e-02	1.3e-02
0.90	0.080	★	1.6e-01	3.9e-01	4.3e-01	4.1e-01	3.3e-02	3.0e-03	4.3e-02	3.0e-02
1.00	0.080	◯	3.6e-02	4.0e-01	6.4e-01	6.2e-01	2.9e-02	1.7e-03	4.9e-02	4.4e-02
1.00	0.080	★	9.2e-02	3.0e-01	6.9e-01	6.7e-01	2.9e-02	1.9e-03	4.8e-02	3.8e-02
1.10	0.080	◯	2.1e-02	2.3e-01	9.3e-01	9.1e-01	2.1e-02	1.4e-03	5.7e-02	5.5e-02
1.10	0.080	★	2.4e-02	1.9e-01	9.6e-01	9.4e-01	2.2e-02	1.3e-03	5.6e-02	5.3e-02
1.20	0.080	★	1.4e-02	6.3e-02	1.2e00	1.2e00	1.4e-02	6.3e-04	6.5e-02	6.4e-02
1.00	0.090	◯	3.1e-02	3.8e-01	6.7e-01	6.5e-01	3.0e-02	2.0e-03	5.8e-02	5.3e-02
0.70	0.100	◯	2.1e-01	5.5e-01	4.9e-02	2.1e-02	6.3e-02	3.6e-03	3.3e-02	9.2e-03
1.00	0.100	◯	3.1e-02	3.6e-01	7.1e-01	7.0e-01	3.1e-02	9.5e-04	6.8e-02	6.3e-02
1.10	0.100	◯	2.3e-02	1.5e-01	1.0e00	1.0e00	2.3e-02	7.3e-04	7.6e-02	7.4e-02
1.20	0.100	◯	1.5e-02	2.3e-02	1.3e00	1.2e00	1.5e-02	1.0e-04	8.5e-02	8.4e-02

Note. — A ◯ indicates a double detonation while a ★ indicates an edge-lit ignition.

Chapter 3

Observational Signatures of Double Detonations in the Photospheric Phase

The content of this chapter is drawn from Polin et al. (2019b), with permission from the co-authors.

In this chapter we take the hydrodynamic ejecta models produced in (Polin et al. 2019b) (and Chapter 2) and perform radiative transport modeling in order to examine the observational signatures of double detonation explosions. Distinct observational signatures of sub-Chandrasekhar mass WD explosions are predicted for two categories of shell size. Thicker-shell models show an early time flux excess, which is caused by the presence of radioactive material in the ashes of the helium shell, and red colors due to these ashes creating significant line blanketing in the UV through the blue portion of the spectrum. Thin shell models reproduce several typical Type Ia supernova signatures. We identify a relationship between Si II velocity and luminosity which, for the first time, identifies a sub-class of observed supernovae that are consistent with these models. This sub-class is further delineated by the absence of carbon in their atmospheres. We suggest that the proposed difference in the ratio of selective to total extinction between the high velocity and normal velocity Type Ia supernovae is not due to differences in the properties of the dust around these events, but is rather an artifact of applying a single extinction correction to two intrinsically different populations of supernovae.

First we describe the radiative transport methods used to produce synthetic light curves and spectra in Section 3.1. These light curves and spectra are examined and compared to real events in sections 3.2 and 3.3 respectively. The results are summarized and future directions are discussed in section 3.4.

3.1 Radiative Transport Methods

After the SN ejecta reaches homologous expansion we use the Sedona code (Kasen et al. 2006) to create synthetic light curves and spectra for each model. Sedona is a multi-dimensional time dependent radiation transport code which uses Monte Carlo methods to propagate photons. The calculations are performed under the assumption of local thermal equilibrium (LTE) to determine ionization and excitation fractions in the ejecta. Energy is generated through three radioactive decay chains: ^{56}Ni$\rightarrow^{56}$Co$\rightarrow^{56}$Fe, ^{48}Cr$\rightarrow^{48}$V$\rightarrow^{48}$Ti and ^{52}Fe$\rightarrow^{52}$Mn$\rightarrow^{52}$Cr. While SNe Ia light curves are primarily powered by the radioactive decay of ^{56}Ni, the double detonation scenario can create a large amount of radioactive ^{48}Cr and ^{52}Fe during helium burning (see Figure 2.3). The radioactive material present in the outer most ejecta can drastically effect the early features of these events, and thus the inclusion of these additional radioactive decay chains is vital to properly model the early signatures of a double detonation explosion.

3.1.1 Local Thermal Equilibrium: the Validity and Limitations of LTE Transport

In this work we employ the assumption of local thermal equilibrium (LTE) while calculating the photospheric light curves and spectra of our double detonation models. The LTE approximation is appropriate to use in situations where the ionization and excitation states are determined by thermal processes, and thus can be calculated using the Saha ionization and Boltzmann excitation equations. The LTE approximation can be used for both blackbody photons (where radiative transitions dominate) and regimes where the mean free path for collisions between the gas particles are short compared to that of the photons (where collisions dominate).

We can think of SNe ejecta as being split into two regimes, those below and above the photosphere. Below the photosphere the ejecta are optically thick. Here photons are trapped in the ejecta and can be modeled as a blackbody distribution. The LTE assumption should be a good approximation in this regime. Above the photosphere the ejecta are more disperse and collisions between gas particles and photons may be insufficient to maintain equilibrium. Here the LTE solution will start to fall apart as the spectrum deviates from a blackbody, however these deviations should be small for the early part of the SN evolution. Used safely in this epoch the LTE assumption has been shown to produce reasonable results, deviating from the NLTE solution quantitatively rather than qualitatively. For example, Baron et al. (1996) show that in Type Ia SN models the LTE calculations reproduce the values of the atomic level populations near and below the SN photosphere.

Many groups have examined how the LTE assumption effects the observational signatures of Type Ia SNe. Jack et al. (2011) explore how the light curves of the W7 pure deflagration model (Nomoto et al. 1984) differ under a LTE assumption from the full NLTE solution. Throughout the light curve rise the LTE and NLTE approaches show reasonable agreement. The LTE approximation is 0.01 mag brighter in the B-band than the NLTE solution at time

of peak brightness. However, over time the LTE and NLTE solutions diverge, particularly in the I-band, which is comprised of longer wavelengths which are the first to become optically thin. Nugent (1997) also examines the W7 model, this time to determine the spectroscopic differences in the LTE assumption from the NLTE calculations. The spectrum of the W7 model at 20 days looks qualitatively similar in both LTE and NLTE as far as the shape of the continuum is concerned, however the LTE solutions struggles to produce enough flux in the longer wavelengths (relating to the same I-band discrepancy shown in Jack et al. (2011)). The exact strengths of individual absorption lines also varies. The LTE result showed minor discrepancies in Si II and Ca II, but showed significantly weaker O I absorption from all examined depths in the ejecta.

Our models are less massive than the W7 model (which explodes near the Chandrasekhar mass limit) but the SNe ejecta reach similar velocities. Therefore, we expect that our models reach a region where a significant part of the ejecta becomes optically thin earlier than the W7 model. Given these constraints we conclude that the LTE assumption employed is appropriate to produce reasonable observables from first light through roughly 1 week after time of peak. We particularly expect the qualitative trends we point out to remain robust. At later times, however, NLTE methods would have to be used to model the proper light curves and spectra for double detonations.

In Chapter 4 we examine the nebular emission spectra of our models while accounting for NLTE effects, however the methods used in that chapter require the full ejecta to be optically thin. This is only a safe assumption in the nebular phase, beginning ∼150 days after explosion. In the intermediate regime (∼20-100 days post maximum) non-thermal effects are important, but the spectra can not yet be simplified to only emission lines. To model this region full NLTE transport will need to be performed in the future, but such calculations are beyond the scope of this thesis.

3.2 Light Curves

The radiative transport calculations from Sedona provide synthetic light curves and spectra of each model. For the remainder of this paper, models will be separated into two categories: thin helium shells and thick helium shells. The former likely evolve from a degenerate helium WD binary companion (Bildsten et al. 2007; Shen & Bildsten 2014) and look more like standard SNe Ia. The later evolve from a non-degenerate helium star companion (Woosley & Weaver 1994; Livne 1990; Nomoto 1982b), exhibit more exotic observable signatures, and thus should be considered a sub-class of their own - with potentially only one of these events convincingly seen to date (Jiang et al. 2017).

Figure 3.1 shows the g-band light curves for models with the extrema of helium shell masses explored in this survey: the very thick shells, 0.08 $M_\odot$, and the very thin shells, 0.01 $M_\odot$. The presence of radioactive material from the burning of the helium shell can create an excess in the flux at early times in the light curves of the models. The thin shells in Figure 3.1 do not produce enough radioactive material from the shell burning to

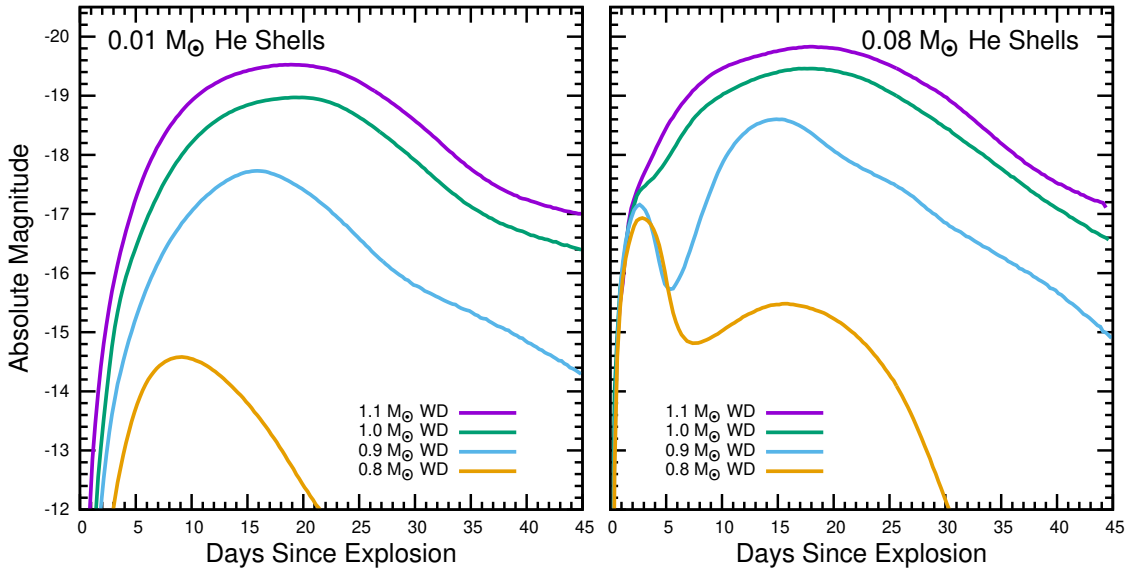

Figure 3.1: g-band light curves of double detonation explosions for thin helium shells (0.01 $M_\odot$) on the left and thick helium shells (0.08 $M_\odot$) on the right. The figure shows a 1.1 $M_\odot$ WD in purple, a 1.0 $M_\odot$ WD in green, a 0.9 $M_\odot$ WD in blue and a 0.8 $M_\odot$ WD in orange. The thick helium shell models on right exhibit an early time flux excess due to radioactive material (^{48}Cr, ^{52}Fe, and ^{56}Ni) in the outermost ejecta, while the thin shell models on the left exhibit a smooth rise.

exhibit this early time excess, and the early rise looks like those typical of SNe Ia. The thick shells, however, produce a large amount of heavy, radioactive elements having $Z \geq 22$ in the outermost ejecta, resulting in a significant excess in the first few days after explosion due to additional radioactive heating. The result is a bi-modal light curve with the first peak, a few days after explosion, powered primarily by radioactive material in the outermost ejecta, followed by a more standard ^{56}Ni powered rise typical of thermonuclear SNe Ia light curves. However the time of peak brightness will occur later than a pure ^{56}Ni powered rise due to the decay of ^{48}V (a daughter species of the ^{48}Cr leftover from the helium shell) which has a half-life of 15.97 days.

For models with enough mass in the helium shell the early flux excess can be observed in surveys that explore the light curves of SNe 4 to 5 magnitudes below peak brightness. See table 3.1 for the magnitudes at both peak and early excess (when presented) for all models. When exhibited, this flux excess is present across all observable bands with the greatest differences occurring in the near-UV (See Figure 3.2).

As a result the colors shown in Figure 3.3 can become significantly red directly after the flux excess, before trending bluer again for the ^{56}Ni powered rise. This figure depicts the $g-r$ and $g-i$ colors for 1.0 $M_\odot$ with several different mass helium shells. The early red evolution

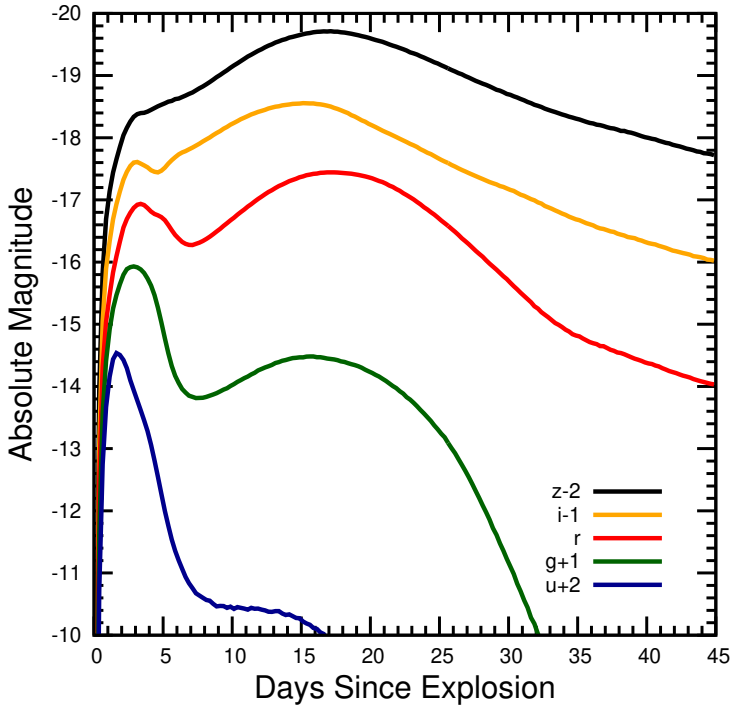

Figure 3.2: ugriz colors for a thick helium shell model; a 0.8 $M_\odot$ WD with a 0.08 $M_\odot$ helium shell. For this model the radioactive material produced by the shell is comparable to the amount produced by the WD. The early excess flux created from the decay of the outermost radioactive material is similar in magnitude to the ^{56}Ni powered peak. However the early flux excess is not uniform across the different bands.

is a direct prediction that can identify a double detonation explosion, even when the helium shell is thin and the flux excess is not large. We note the change in behavior between the 0.06 and 0.08 $M_\odot$ helium shells on the 1.0 $M_\odot$ WD in Figure 3.3. This trend of a bluer feature for larger shells (on the same underlying WD) is caused by the additional heating from the radioactive material produced during helium burning. The 1.0 $M_\odot$ WDs shells above 0.06 $M_\odot$ produce enough radioactive material to cause significant heating at early time. Large shells on smaller WDs, however, can still appear quite red (see Figure 3.2). This observational signature of a sub-Chandrasekhar mass Ia explosion can be detected photometrically though high cadence multi-band observations at very early times.

While qualitatively similar to the results seen in the double detonation models presented in Noebauer et al. (2017), the $g - r$ colors of our models are noticeably redder than theirs, likely due to differences in how the radiation transport is handled in STELLA (Blinnikov et al. 2000) compared to Sedona.

Jiang et al. (2017) present evidence for a SN Ia trigger by a helium flash. The characteristics of SN 2016jhr are a kink in the early light curve, coupled with a color which evolves from

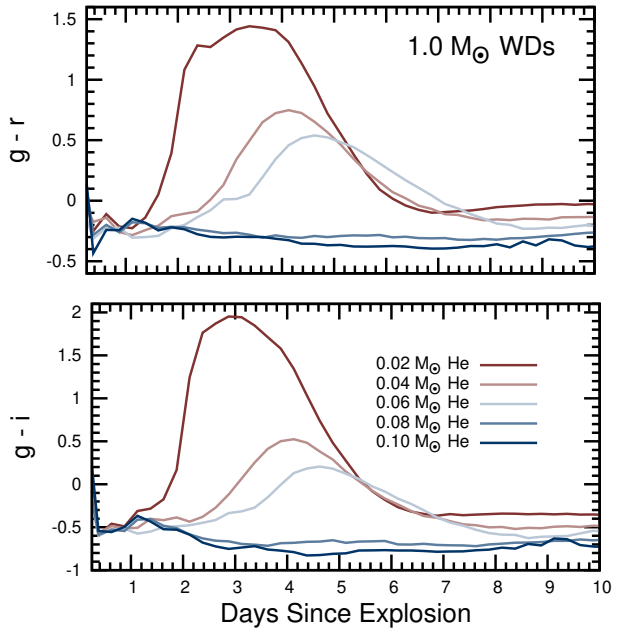

Figure 3.3: g-r and g-i colors for a 1.0 $M_\odot$ WD with varying helium shell masses. It is interesting to note that models with less pronounced early excess peaks show the most significant reddening. This is due to the production of additional radioactive material by the heavier shell, on the same mass of underlying WD, heating the supernova at early times though radioactive decay.

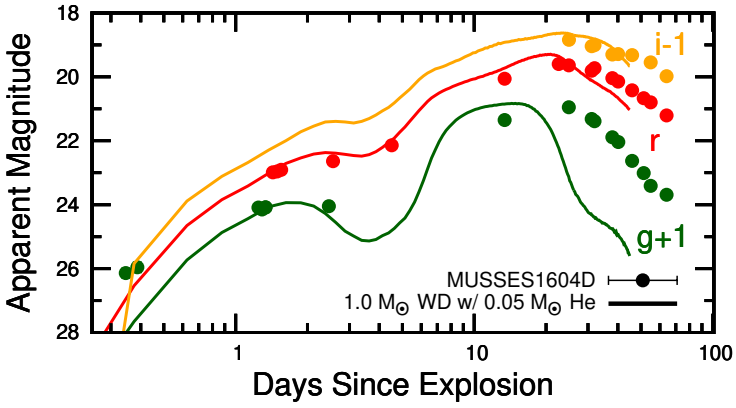

Figure 3.4: SN 2016jhr (MUSSES1604D) (Jiang et al. 2017) plotted against this survey's best fit model for the early flux excess, a 1.0 $M_\odot$ WD with a 0.05 $M_\odot$ helium shell. *i*-band (-1) is plotted in yellow, *r*-band in red, and *g*-band (+1) is green. While a double detonation explosion can reproduce the magnitudes at peak and during the early flux excess, the overall width is too narrow in all bands, most noticeably in *g*-band.

Table 3.1: Observables from Synthetic Light Curves.

M_{WD}	M_{He}	type	V-mag excess	V-mag peak	B-mag excess	B-mag peak	$\Delta m_{15,V}$	B-V
0.70	0.010	◯		-11.58		-10.36	3.20	1.22
0.80	0.010	◯		-15.22		-14.20	2.29	1.03
0.85	0.010	◯		-16.59		-15.84	1.63	0.75
0.90	0.010	◯		-17.81		-17.56	1.33	0.25
1.00	0.010	◯		-18.97		-18.86	1.09	0.12
1.10	0.010	◯		-19.51		-19.42	0.91	0.09
1.20	0.010	◯		-19.83		-19.76	0.72	0.07
1.00	0.020	◯	-15.34	-19.00	-15.26	-18.96	1.22	0.04
0.85	0.025	◯	-14.13	-17.01	-13.42	-14.81	2.01	2.20
1.00	0.030	◯	-15.95	-19.06	-15.90	-19.02	1.22	0.04
1.00	0.040	◯	-16.40	-19.13	-16.31	-19.09	1.22	0.04
0.95	0.045	◯	-16.61	-18.88	-16.54	-18.18	0.98	0.70
0.60	0.050	◯		-7.01		-4.48	2.75	2.53
0.70	0.050	◯	-14.65	-11.96	-14.07	-9.36	4.46	2.60
0.80	0.050	◯	-9.75	-16.17	-9.87	-13.70	4.27	2.47
0.90	0.050	◯	-16.31	-18.54	-16.34	-17.91	1.29	0.63
1.00	0.050	◯	-16.05	-19.00	-15.61	-18.73	1.10	0.27
1.00	0.050	◯	-15.70	-19.00	-15.19	-18.73	1.07	0.28
1.00	0.050	◯	-16.66	-19.22	-16.57	-19.18	1.26	0.05
1.10	0.050	◯	-16.96	-19.68	-16.93	-19.61	0.90	0.06
1.10	0.050	◯	-17.08	-19.68	-17.11	-19.63	0.83	0.05
1.10	0.050	★	-11.27	-19.73	-11.51	-19.66	0.82	0.06
1.20	0.050	◯	-9.57	-19.93	-9.63	-19.87	0.58	0.06
1.20	0.050	★	-9.96	-19.97	-10.05	-19.89	0.65	0.08
0.95	0.055	◯	-16.70	-18.89	-16.65	-18.30	1.01	0.59
1.00	0.060	◯	-17.06	-18.81	-16.93	-18.87	1.08	-0.06
1.00	0.070	◯	-17.24	-19.32	-17.08	-19.29	1.18	0.03
0.60	0.080	◯	-13.55	-11.98	-12.36	-10.14	6.55	1.85
0.70	0.080	◯	-16.43	-14.43	-16.42	-12.14	6.14	2.29
0.80	0.080	◯	-16.93	-17.06	-16.75	-14.47	3.65	2.59
0.90	0.080	◯	-16.95	-18.81	-16.93	-18.06	1.12	0.75
0.90	0.080	★	-15.95	-19.01	-15.92	-18.95	1.04	0.06
1.00	0.080	◯	-17.49	-19.38	-17.42	-19.35	1.20	0.03
1.00	0.080	★	-11.11	-19.51	-11.34	-19.48	0.94	0.03
1.10	0.080	◯	-17.31	-19.79	-17.34	-19.73	0.79	0.06
1.10	0.080	★	-8.80	-19.84	-8.56	-19.79	0.76	0.06
1.20	0.080	★	-8.79	-20.01	-6.81	-19.96	0.55	0.05
1.00	0.090	◯	-17.58	-19.41	-17.54	-19.39	1.16	0.02
0.70	0.100	◯	-16.99	-15.12	-16.85	-12.29	5.86	2.83
1.00	0.100	◯	-17.73	-18.86	-17.73	-18.95	1.13	-0.10
1.10	0.100	◯	-8.56	-19.89	-7.68	-19.84	0.68	0.05
1.20	0.100	◯	-9.20	-20.01	-8.61	-19.98	0.45	0.03

Note. — A ◯ indicates a double detonation while a ★ indicates an edge-lit ignition.

the blue to the red. This is similar to the behavior of many of our models (see Figure 3.4), though in our parameter sweep we do not find a perfect match to this SN Ia. We do note that this SN Ia is similar to the very rare class of SNe Ia which include SN 2006bt (Foley et al. 2010) and PTF10ops (Maguire et al. 2011) - SNe Ia which have broad light curves that are incongruent with their peak brightness with respect to the Phillips relationship (Phillips 1993).

3.3 Spectra

This section examines the synthetic spectra produced for our models with `Sedona`. Again, models are grouped into two categories: thick shell models and thin shell models. The former exhibit peculiar features due to the radioactive material in their outermost ejecta that serve to distinguish them from a normal SN Ia. The later reproduce several typical SN Ia signatures.

3.3.1 Thick Shell Models: Predictions for Future Searches

The top panel of Figure 3.5 shows the spectra at g-band peak for several models with 0.08 $M_\odot$ helium shells. The spectra at g-band peak exhibit significant line blanketing at low wavelengths due to the ashes of the burnt helium shell. Models with 0.08 $M_\odot$ helium on WDs less than 0.8 $M_\odot$ are completely line blanketed for wavelengths less than 5200 Å.

The bottom panel of Figure 3.5 shows an example spectrum taken at the time of the early flux excess due to radioactive decay of material created from the burnt helium shell (typically 2-3 days after explosion). These early spectra all look qualitatively similar: a blue continuum which is mostly featureless above 4500 Å while bluer wavelengths show a Ti II trough (∼4000-4300 Å) and a Ca II H&K absorption feature (∼3700 Å). Because spectra at this early flux excess all look similar only one example (from the 0.8 $M_\odot$ WD) is included in the plot.

We note that 3-D simulations of deflagration driven Chandrasekhar mass CO WD explosions have also produced ^{56}Ni mixed into the outer layers of SN ejecta (Fink et al. 2014). While these explosions also produce red, sub-luminous, light curves they lack the early flux excess and extreme UV line blanketing seen in our thick shell spectra and thus would be distinguishable from a sub-Chandrasekhar explosion.

At the time of publication Polin et al. (2019b) predicted these spectral signatures of double detonations driven by thick helium shells, which at the time had yet to be seen in an observed SN Ia. Since then the discovery of SN 2018byg (ZTF 18aaqeasu) has confirmed the possibility of these explosions occurring in nature. See Chapter 5 for a more in depth discussion of this discovery and its role in supporting this theory.

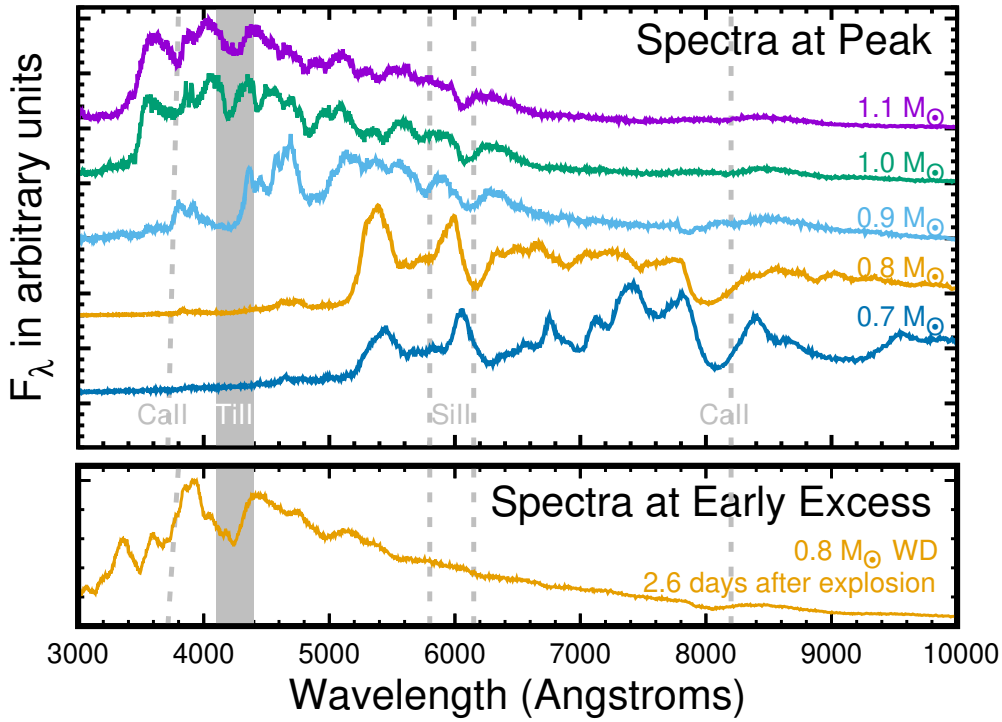

Figure 3.5: Spectra of the double detonations with thick (0.08 $M_\odot$) helium shells at peak in the top panel and an example spectrum during an early excess flux peak in the bottom panel, at which time for all models the spectra look qualitatively the same. The spectra of the thick shell models exhibit significant line blanketing at low wavelengths due to the ashes of the burnt helium shell. Models with 0.08 $M_\odot$ helium on WDs less than 0.8 $M_\odot$ are completely line blanketed for wavelengths less than 5200 Å. The spectra taken at early excess is almost featureless with the exception of a Ti II trough present from 4000-4300 Å. These predicted signatures have yet to be seen in an observed SN Ia.

3.3.2 Thin Shell Models: Relationship to Observed SNe Ia

The very thin shell models in this survey, those with 0.01 $M_\odot$ helium on their surface, exhibit similar characteristics to many normal SNe Ia. In Figure 3.6 we present the spectra of these models at g-band peak ordered by total mass. The thin shell models exhibit many of the characteristics expected from the spectroscopic series in Nugent et al. (1995). The models show the characteristic change in the ratio of the Si II lines. The 5800 Å feature decreases in strength with respect to the 6150 Å feature, as the luminosity (and mass) of the models increase. As the luminosity (mass) of the models increase, we also see Fe II transitioning to Fe III. Lastly, we see Ti II features begin to appear in low luminosity (mass) models.

As noted by Shen et al. (2018a) and seen in Figure 3.7, the thin shell WDs with mass 0.85 $M_\odot$ are able to reproduce the features seen in the sub-luminous SN 1991bg class of

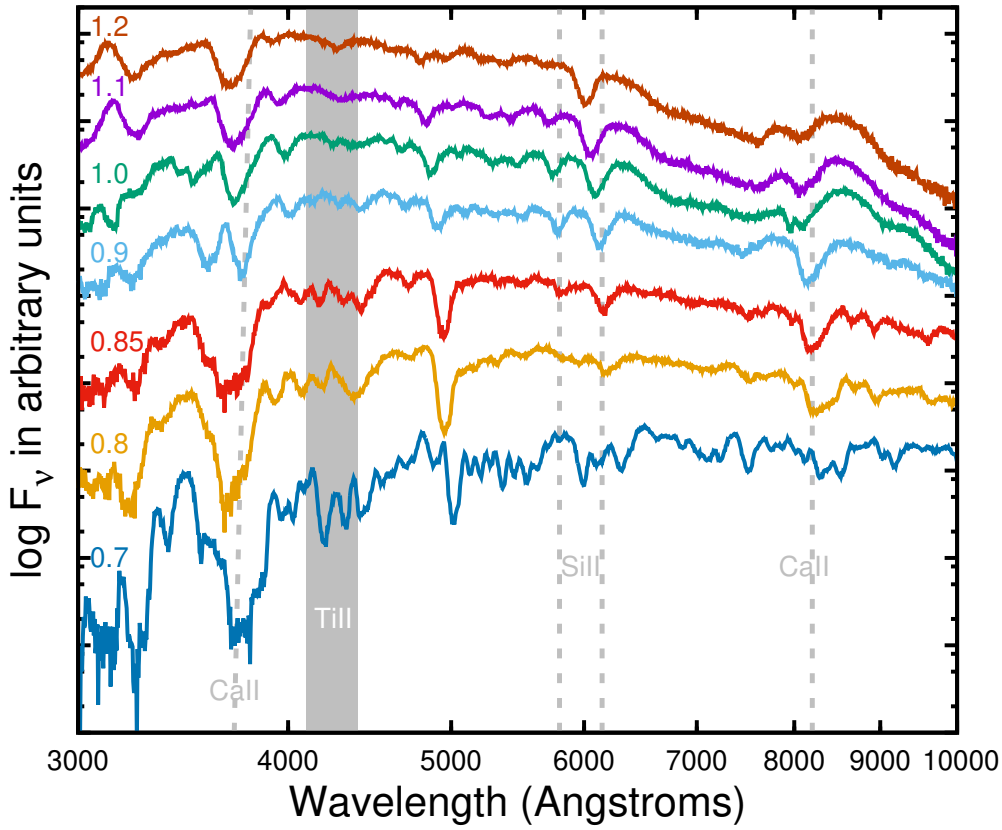

Figure 3.6: A peak-brightness spectral series similar to that in Nugent et al. (1995), following just the supernovae formed through the double detonation process with helium shells of 0.01 $M_\odot$. We note that the velocity of the Si II line at 6150 Å is faster for more massive (and more luminous) events. This points to an overall mass-luminosity-velocity relationship the origins of which we discuss in Section 3.3.3.

objects. Interestingly, just below this mass the features do not resemble those of any known supernovae.

Given the search conducted by Li et al. (2011a) and the sheer number of 1991bg-like SNe Ia they discovered, we believe that they would have been sensitive to finding SNe Ia slightly below this mass given that their luminosity cut-off was 1-2 magnitudes fainter in their search than the peak brightness for the 1991bg-like objects ($M_B \sim -17.25$). Coupled with the mass function for CO WDs increasing below this mass (Hollands et al. 2018), it is thus likely that the 0.85 $M_\odot$ WDs represent some minimal total mass in the ignition of sub-Chandrasekhar mass explosions, or that there is an entirely separate mechanism for these supernovae.

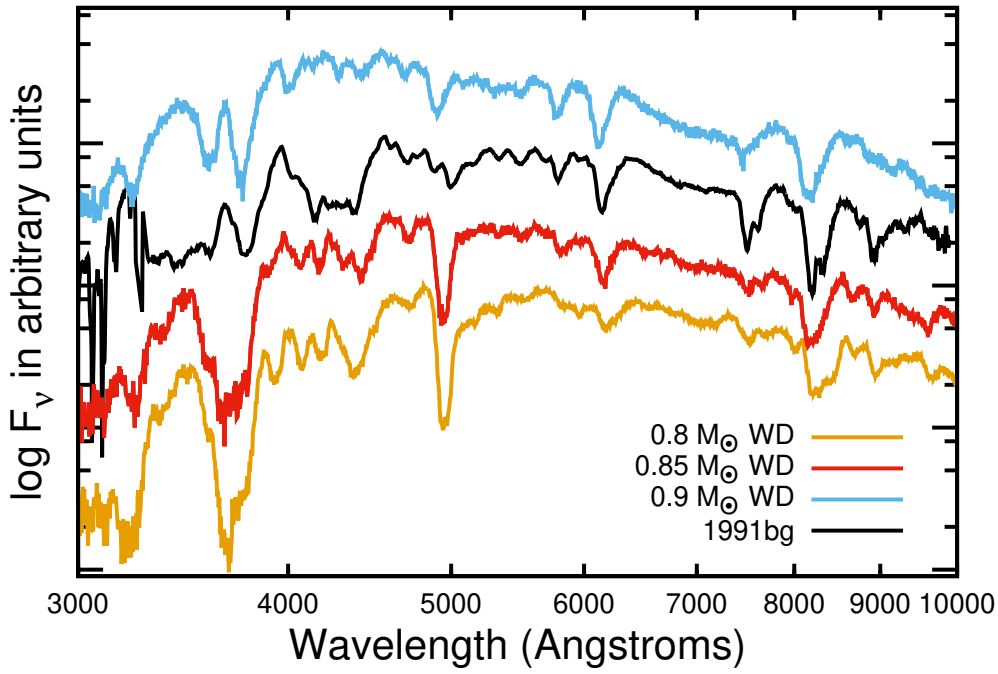

Figure 3.7: A comparison of SN 1991bg to the 0.8, 0.85 and 0.90 $M_\odot$ WDs with helium shells of 0.01 $M_\odot$. The number of SNe Ia like SN 1991bg (Filippenko et al. 1992b; Li et al. 2011a) and the sensitivity of our models to total mass imply that either there is some natural floor to exploding SNe Ia at this mass ($M_{tot} \sim 0.85$ $M_\odot$) or that these SNe are created by another mechanism.

3.3.3 Thin Shell Models: Implications of Kinetic Energy — Mass Relationship

One of the interesting properties of the sub-Chandrasekhar class of models is that there is an implicit relationship between the mass of the WD and the total ^{56}Ni created. Unlike in the case of a traditional Chandrasekhar mass explosion where the amount of ^{56}Ni produced is a function of the duration of the deflagration phase and the location of the deflagration-detonation transition, the sub-Chandrasekhar mass explosions do not go through a deflagration phase, and as pure detonations the amount of ^{56}Ni produced is solely a function of the total mass (and central density) of the progenitor. For the models which resemble observed SNe Ia (0.85 $M_\odot < M_{WD} <$ 1.2 $M_\odot$), the gravitational binding energy only increases by a factor of 3.5 while the ^{56}Ni mass increases by two orders of magnitude over this range in mass. Consequently this further implies a direct relationship between the mass and the kinetic energy, as the kinetic energy in these explosions is a direct result of the CO synthesized to heavier elements in the explosion minus the gravitational binding energy of the WD. This can be seen in Figure 3.6 and in Figure 15 of Shen et al. (2018a) where the Si II

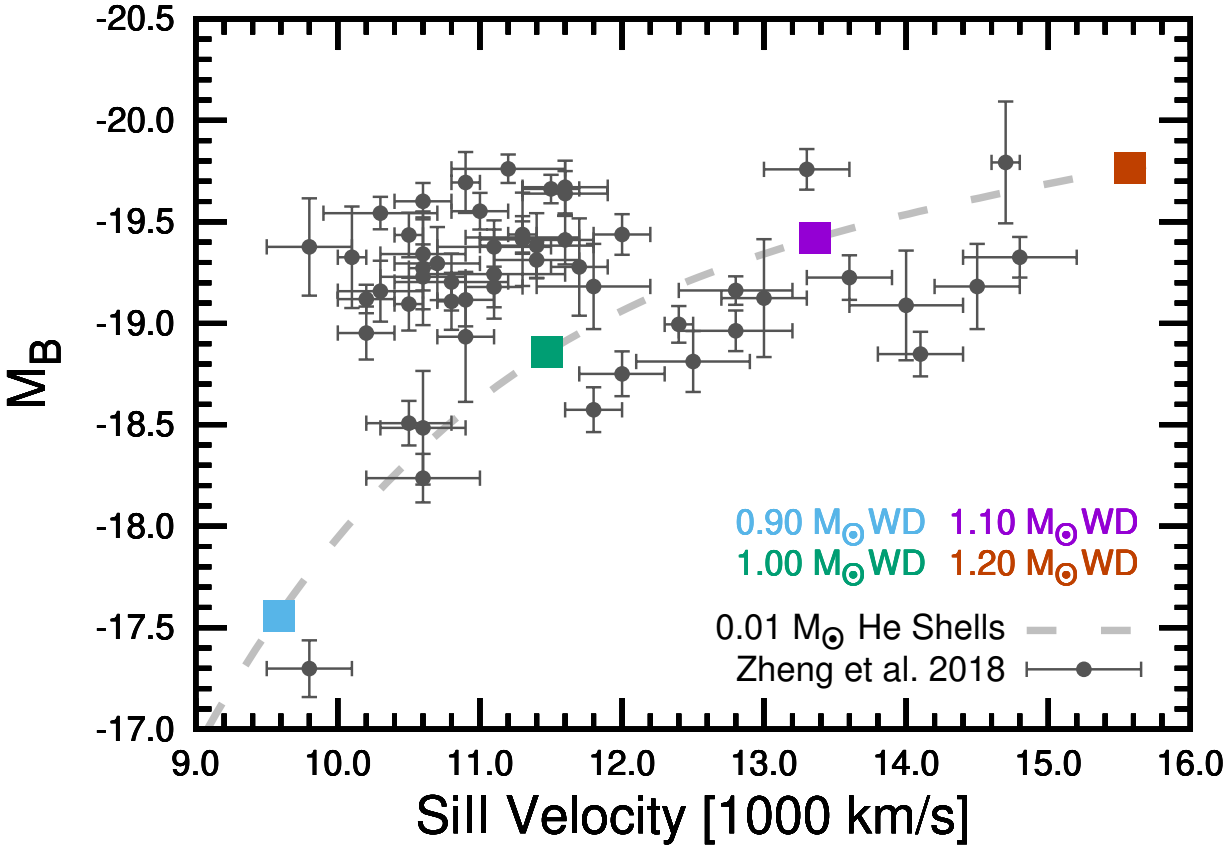

Figure 3.8: A plot of the Si II velocity vs. M_B (both at B-band peak) for those SNe Ia found in Zheng et al. (2018) and our thin shelled models which are connected by a spline fit (dashed line) to guide the eye. We note there is a cluster of SNe Ia that follow this relationship and a tight bunch that are offset and at lower velocities, given their luminosity, from our models.

velocity is proportional to the mass of the WD. While we have only explored WD with 50-50 carbon-oxygen fractions, Shen et al. (2018a) shows that when one explodes WDs with ratios of 30-70, the velocity drops by a few hundred km/s and the luminosities decrease by $\sim 10\%$. Thus, even spanning the full possible range in the permissible ratio of carbon to oxygen, there will exist a very tight relationship between luminosity and the Si II velocity.

In Figure 3.8 we explore this further by plotting our models on top of the extinction corrected observed SNe Ia found in Zheng et al. (2018) in a plot of M_B vs. the velocity of Si II. What becomes immediately apparent given the location of our models, is that there appears to be two separate clusters of SNe Ia. The first cluster traces our models and follows the relationship between brightness and velocity that is a natural byproduct of the sub-Chandrasekhar class of explosions. The second cluster is offset from this relationship, quite tightly bunched, and is considerably slower given their median luminosity than our models.

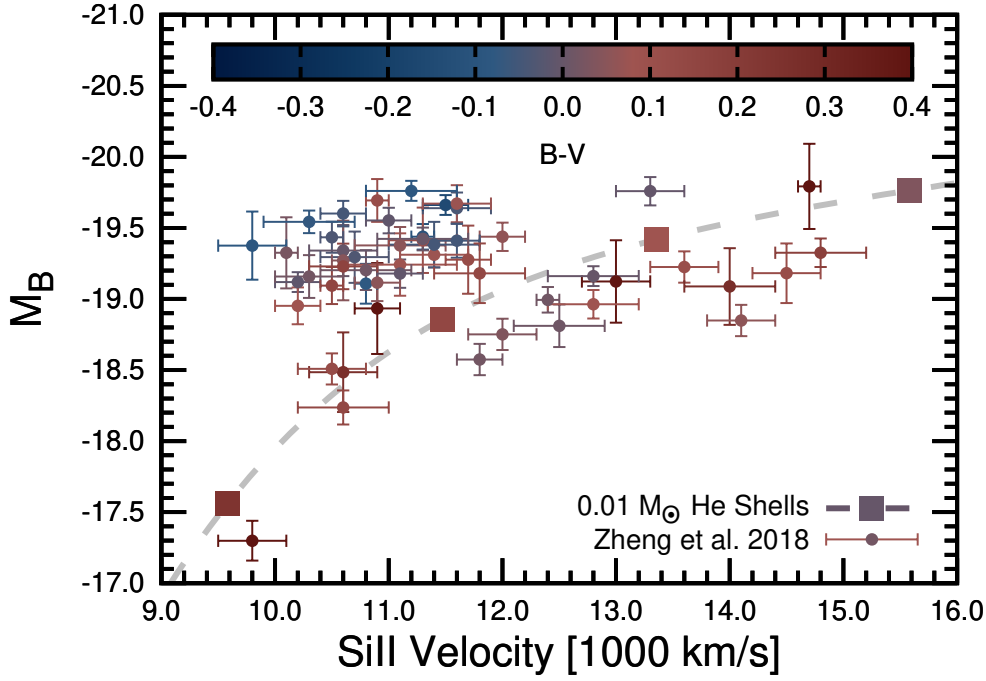

Figure 3.9: A plot of the Si II velocity vs. M_B (both at B-band peak) for the models and the observed SNe Ia of Zheng et al. (2018). The color scale shows the $B_{max} - V_{max}$ colors for each SN Ia, though for the observed SNe Ia we have only corrected for MW extinction. Note that the models are significantly redder than the colors seen for those SNe Ia found in the clump to the upper left, while the SNe Ia that follow the monotonic relationship between velocity and brightness have similar colors to the models.

This second cluster likely represents explosions at the Chandrasekhar limit. The difference in velocity of this clump from our models, at the same luminosity, is what one would expect if these were near the Chandrasekhar limit. This is a combination of the effect of more gravitational binding energy for these WD as well as the differences in the underlying explosion mechanism. Photometric evidence has already pointed to the need for sub-Chandrasekhar mass SNe Ia. Scalzo et al. (2014) show empirical fits to the light curves of the SNLS and SDSS SNe Ia which necessitate 30% of these events originate from sub-Chandrasekhar progenitors. Furthermore, Goldstein & Kasen (2018) show that light curve fits to low-luminosity events require a population of sub-Chandrasekhar explosion mechanisms. Here, we demonstrate, for the first time, both photometric *and* spectroscopic evidence to identify a sub-class of sub-Chandrasekhar SNe Ia which span the range of normal to sub-luminous SNe Ia.

This is not the first time that these supernovae have been called out as being different. Wang et al. (2009a) separates out observed SNe Ia into “normal" and “high-velocity" groupings, split at 11,800 km/s, arguing that these clusters have different dust environments and

thus their extinction corrections should be different. Foley & Kasen (2011) argued that the intrinsic colors for these two groups are different, that there is a tight correlation between velocity and color, and that these two groups are offset from each other in color space. In Figure 3.9 we highlight the color properties of these two clusters of supernovae and our models. It should be noted that while the majority of SNe Ia with peak Si II velocities in excess of 11,800 km/s follow our sub-Chandrasekhar models, there is a significant population of SNe Ia at lower velocity (as well as the 1991bg-like SNe Ia) which do as well. Thus making a single cut at one velocity insufficient to delineate these two populations.

What is further indicative of two separate mechanisms is that some members of the putative clump of Chandrasekhar mass SNe Ia show uncorrected colors bluer than any of our models, while the higher velocity SNe Ia are similar to, or redder than, our models (which can be accounted for by normal extinction due to dust). This further supports the clustering of the observed SNe Ia into these groups, though we note that we have employed a single extinction correction (following Zheng et al. (2018)) in the calculation of M_B and more work here needs to be done to carefully sub-classify and identify individual SNe Ia as being in one group or another. What this does imply is that corrections for extinction due to dust must take into account the intrinsic colors of the sub-classes of SNe Ia, and that this can not be simply done with a single velocity cut to separate these groups. Furthermore it obviates the need for different R_V's for the high-velocity group of SNe Ia.

Finally, we note a potential prediction of our models with respect to the division between these two clusters of SNe Ia. In all of our models that match the observed SNe Ia (the thin shell models with 0.85 $M_\odot < M_{WD} <$ 1.2 $M_\odot$), the amount of unburnt carbon is quite minimal with only 0.001 $M_\odot$ in the 1991bg-like events dropping to 10^{-5} $M_\odot$ or less for the more normal SNe Ia. The efficiency of carbon-burning is a characteristic of the sub-Chandrasekhar models, though more work will have to be done with multi-dimensional simulations to verify this property. Even still, examining several 1-D Chandrasekhar-mass models shows that the amount of unburnt carbon can be quite substantial. The pure deflagration model W7 of Nomoto et al. (1984) and the pulsating delayed detonation models seen in Hoeflich et al. (1995) typically have ∼0.03 $M_\odot$ of carbon left over after explosion.

3.4 Discussion

We have presented the results and analysis of a survey of 1-D sub-Chandrasekhar mass WD explosion models. These models can be separated into two categories, those with thin and thick helium shells. The thick helium shell models are considerably different from the SNe Ia observed at time of publication, with the possible exception of the SN 2006bt and PTF10ops like supernovae. The following characteristics summarize their properties:

– A detectable early excess in flux in the SNe Ia light curves during the first few days after explosion caused by radioactive material burned in the helium shell.

- Significant blanketing in the UV and the blue portion of the optical spectra near peak due to the Fe-peak elements in the helium shell ashes.
- The very early spectra show a handful of spectroscopic features in the near-UV through 5000Å, but are otherwise featureless.
- A distinct red-to-blue evolution of the optical colors shortly after explosion

These signatures were later all exhibited by the prototype event: SN 2018byg (see Chapter 5 for more details).

The models with thin helium shells exhibit light curves and spectral features similar to normal SNe Ia. We show an inherent correlation between mass, brightness and velocity of the spectral features exhibited by these models. Noting this, and comparing to a recent set of well-observed SNe Ia, we see further evidence for at least two distinct populations of SNe Ia either having Chandrasekhar-like masses or sub-Chandrasekhar masses.

The implications for using SNe Ia as cosmological probes are two-fold. First, it is likely that additional light curve features and/or a spectrum will be needed to sub-classify these events. Specifically we urge observers to try to obtain very early color information to point to evidence of helium shells (shown in Figure 3.3), as well as the more commonly obtained spectrum at time of peak brightness which allows us to identify those events which follow our luminosity-velocity relationship. Second, as the intrinsic colors of these two populations are different, this will necessitate different extinction corrections for each sub-class. Evidence supporting the latter has likely already been seen in cosmological data, as we discuss below.

These two classes of SNe Ia will likely require different light curve corrections in order to properly use them as standard candles. For example, if we take our model of a 1.0 $M_{\odot}$ WD with a 0.01 $M_{\odot}$ He shell and try to naively determine its absolute magnitude by measuring the width of the light curve and placing it on the Phillips relation, we would calculate that the peak magnitude should sit around -16.5 mag. In reality the light curve peaks at about two magnitudes brighter than this at -18.8 mag, a typical brightness for a normal SN Ia. Part of this discrepancy is likely due to our LTE treatment of the radiative transport calculations, which under-represents the flux at later times, and thus exaggerates our Δm_{15} values (see Section 3.1.1). However, it is likely that the sub-Chandrasekhar mass double detonations will continue to exhibit a more complicated width-luminosity relationship as we improve our modeling methods.

The width of a SN Ia light curve is determined by the opacity of the ejecta which drives the diffusion time for photons to reach the photosphere. The standard SN Ia relationship depends on there only being one free parameter in the SN ejecta, the mass of ^{56}Ni, which heats the Chandrasekhar mass ejecta and raises the opacity. In double detonation explosions there are two factors which determine the opacity of the ejecta: the mass of ^{56}Ni produced in the explosion, which again heats the ejecta raising the opacity, and the mass of the ejecta. A higher mass ejecta will have a higher opacity, and thus a longer diffusion time and wider light curve. Both of these factors will combine to drive the width-luminosity relationship for double detonation explosions.

We expect, therefore, that the two populations of SNe Ia, those deriving of Chandrasekhar mass origin and the sub-Chandrasekhar double detonation explosions, will exhibit two distinct relationships of luminosity and light curve shape. It has been known for some time that the populations of SNe Ia in star forming and dead galaxies are different, and in fact a correction to the luminosity of each is common practice in any of the current cosmological measurements from SNe Ia. Rigault et al. (2018) find evidence for such a distinction when associating SNe Type Ia with the local star formation rate (SFR) of their host environments. They find that the light curve width is strongly correlated with the SFR. Younger hosts produce SNe Ia that are homogenous in shape, while older hosts have a population of SNe Ia with more variation in their light curve widths. Recently, Smith et al. (2020), support these results as they too see a strong correlation between light curve width and host environment while analyzing the 206 spectroscopically confirmed SNe Type Ia discovered by the Dark Energy Survey Supernova Program (DES-SN). It is now well established that there are, at least, two populations of SNe Type Ia, potentially: the Chandrasekhar mass explosions in the younger hosts and the double detonations in the older hosts, each requiring different luminosity corrections in order to use them for cosmology.

This work has laid the foundation for future multi-D studies of these explosions which may reveal distinct line-of-sight differences that could be probed by spectropolarimetry, allowing us to further disentangle the potential progenitor systems for SNe Ia. Furthermore, the effects of even minimal mixing in the outermost ejecta during hydrodynamic evolution can lead to changes in the early flux excess present in our thick shell models. Future studies will probe how much mixing is realistically achievable through higher dimensional simulations, carefully examine nucleosynthetic yields from the burning helium shells, and place limits on the amount of unburnt carbon that remains after explosion.

Chapter 4

Nebular Phase Double Detonations: NLTE Radiative Transport Modeling

The content of this chapter is drawn from Polin et al. (2019a), with permission from the co-authors.

In this chapter we again take the hydrodynamical simulations presented in Chapter 2 (and Polin et al. 2019b) and examine their observational signatures in the nebular phase. Previously our observables were limited to those occurring in the photospheric phase owing to the assumption of local thermal equilibrium (LTE) in our transport methods, which is only valid in the optically thick regimes. Here we use non-LTE (NLTE) radiative transport modeling to examine observational signatures of sub-Chandrasekhar mass double detonation explosions in the nebular phase (beginning $\sim$150 days after explosion). Results range from spectra that look like typical and subluminous Type Ia supernovae (SNe) for higher mass progenitors to spectra that look like Ca-rich transients for lower mass progenitors. This ignition mechanism produces an inherent relationship between emission features and the progenitor mass as the ratio of the nebular [Ca II]/[Fe III] emission lines increases with decreasing white dwarf (WD) mass. Examining the [Ca II]/[Fe III] nebular line ratio in a sample of observed SNe we find further evidence for the two distinct classes of SNe Ia identified in Polin et al. (2019b) by their relationship between Si II velocity and B-band magnitude, both at time of peak brightness. This suggests that SNe Ia arise from more than one progenitor channel, and provides an empirical method for classifying events based on their physical origin.

In Section 4.1 we describe the methods used to model nebular spectra and detail the parameter space of models we explore. We examine the synthetic spectra and qualitatively compare them to the trends of Type Ia SNe in Section 4.2. In Section 4.3 we discuss the strong [Ca II] emission as the dominant feature in the modeled spectra. We compare the models to an existing set of observed nebular SNe Type Ia in Section 4.4 and discuss the overarching implications of this study in Section 4.5.

4.1 Methods

We begin with the homologous ejecta profiles produced by Polin et al. (2019b) and use the NLTE radiative transport code `SedoNeb`, developed by Botyánszki & Kasen (2017), to produce synthetic spectra in the nebular phase.

4.1.1 Initial Ejecta Profiles

Polin et al. (2019b) explored a parameter space of double detonation models and their observational signatures in the photospheric phase. We begin with the ejecta models that were produced using the massively parallel compressible hydrodynamics code `CASTRO` (Almgren et al. 2010). We examine all models from 0.7-1.2 $M_\odot$ WDs with 0.01-0.1 $M_\odot$ He shells (35 models in total) and perform NLTE radiative transport calculations to produce synthetic spectra in the nebular phase. We then compare our results to data by using some of the photospheric properties simulated by Polin et al. (2019b) using the radiative transport code `Sedona` (Kasen et al. 2006).

4.1.2 NLTE Radiative Transport Methods

Botyánszki & Kasen (2017) have developed a three dimesnional (3D), NLTE, radiative transfer tool to model nebular spectra. The process involves first using the radiative transport code, `Sedona` (Kasen et al. 2006), to model the gamma-ray transport of radioactive decay products to determine the energy deposition rate over time. We then use the nebular code to solve the full NLTE rate equations while taking non-thermal excitations and ionizations into account. Then, assuming homologous expansion, the line emission is integrated along the chosen line of sight to find the wavelength-dependent flux.

Some physical assumptions are made during this process. First, we assume that the gas temperature and level populations have reached equilibrium on a timescale much shorter than the expansion timescale. Next, we assume that by the epochs considered, the entire ejecta has become optically thin. This is a safe assumption for wavelengths of interest at epochs $\gtrsim$ 100 days after explosion, although the ejecta may remain optically thick in the ultraviolet for a longer time (Botyánszki & Kasen 2017).

4.2 Nebular Spectra

In this Section we explore the spectral series produced by our simulations and discuss a qualitative comparison to the observed population of SNe Type Ia in the nebular phase.

4.2.1 Summary of Results

We take each model from Polin et al. (2019b) and produce spectra for 150-450 days from explosion in increments of 50 days.

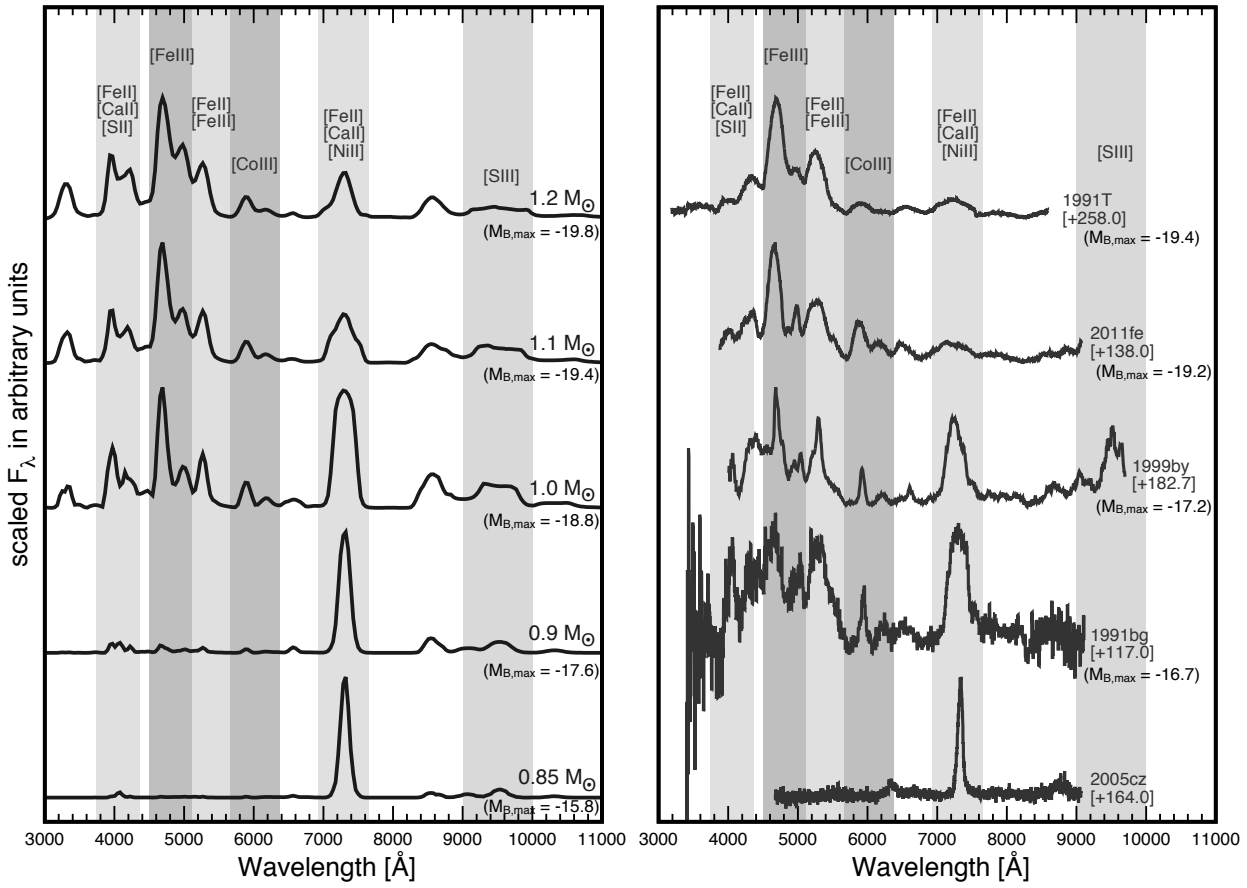

Figure 4.1: *Left*: Nebular spectra of all models with 0.01 $M_\odot$ He shells at 150 days after explosion. Models are arranged in decreasing mass from top to bottom, with labels on the right indicating the mass of the underlying WD, and peak B-band magnutide for each. Strong [Ca II] emission appears in all models. For models that produce less ^{56}Ni (and thus less [Fe II] and [Fe III] emission) the [Ca II] line at 7290 Å is the predominant feature, reminiscent of Ca-rich transients. *Right*: Observed sequence of nebular SNe Type Ia ordered from the most luminous (SN 1991T) to the least luminous (SN 1991bg), as well an example Ca-rich transient (SN 2005cz) at the bottom.

The left panel of Figure 4.1 shows example spectra at 150 days from explosion, ranging from our most massive WD, 1.2 $M_{\odot}$, and decreasing in mass to a 0.85 $M_{\odot}$ WD at the bottom, all with 0.01 $M_{\odot}$ of helium on their surface. We first note that the spectra lack features that distinguish the mass of the helium shell. This result is not entirely surprising as nebular spectra are probes of the internal structure of SNe ejecta, and the inner ejecta of the double detonation models is primarily a function of the total mass of the progenitor ($M_{WD} + M_{He}$). Instead we focus on features that arise as we vary the total mass of the system.

Qualitatively the produced sequence reflects the trends seen in observed nebular SNe Type Ia (see the right panel of Figure 4.1). The more massive progenitors produce spectra with strong Fe lines (∼4500-5600 Å), while also showing [Co III] emission lines (∼5800 - 6200 Å). However, even our brightest model overproduces [Ca II] emission at 7290 Å when compared to the brightest SNe Type Ia (SN 1991T and SN 2011fe). As we examine models with lower masses the spectra show increasingly weaker and narrower Fe emission until, for low enough mass progenitors, the majority of the cooling is through the forbidden [Ca II] emission line at 7290 Å. This too is a trend we see reproduced in the observed SNe Type Ia. Fe emission lines grow narrower for lower luminosity events (Mazzali et al. 1998), and the subluminous, 1991bg-like, SNe Ia show strong emission features around 7290 Å that can reach comparable strengths to their Fe emission (see SN 1991bg and SN 1999by in the right panel of Figure 4.1). Our lowest mass models are reminiscent of the nebular spectrum of a Ca-rich transient. We further examine the implications of the [Ca II] emission in Section 4.3.

4.2.2 Normal Type Ia SNe

In Figure 4.2 we compare our most massive (and most luminous) model to the normal Type Ia SN 2011fe and the W7 pure deflagration model for Type Ia SNe (Nomoto et al. 1984). At a glance the W7 model is a much better fit for a normal Type Ia SN than the double detonation model. While both models reproduce the strength and width of the Fe emission lines in the 4500-5500 Å range, the W7 model does a better job of fitting the emission feature at 7290 Å. This result is not surprising as the W7 model is a decent match to the peak brightness and light curve width of normal SNe Type Ia (Nomoto et al. 1984), while our double detonation models also showed some discrepancies with the observed properties in the photospheric phase (Polin et al. 2019b).

Our results are mostly consistent with previous modeling of SN 2011fe performed by Mazzali et al. (2015). They also note an overproduction of [Ca II] emission seen in nebular spectra produced by a sub-Chandrasekhar model in Mazzali et al. (2015). Mazzali et al. (2015) propose a successful model for the nebular signatures of SN 2011fe originating from a Chandrasekhar mass object with the innermost ejecta populated by stable Fe group species. This stable Fe is required to reproduce the observed [Fe II]/[Fe III] ratio (as seen in the relative strengths of the 5270 Å and 4658 Å Fe emission lines, respectively). The sub-Chandrasekhar mass model is further ruled out by its density profile, which would be less dense in the central regions during burning and produce very little stable Fe, and thus under produce [Fe II] emission. While we agree that the [Ca II] emission is in conflict with the

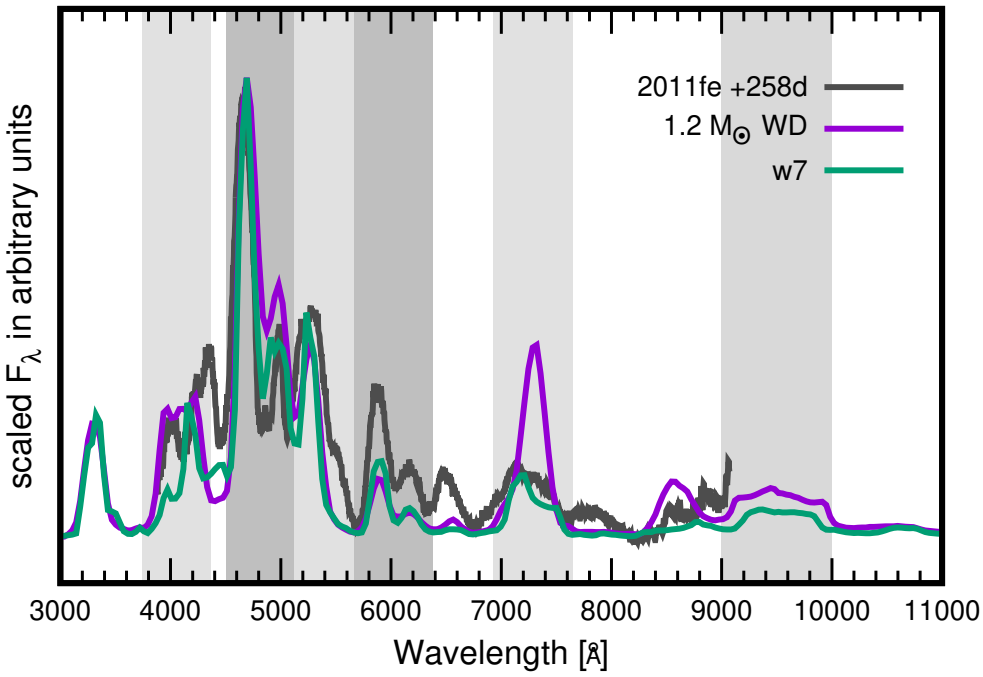

Figure 4.2: The normal Type Ia SN 2011fe at 258 days from peak (Mazzali et al. 2015) compared with our most luminous (and most massive) model (1.2 $M_{\odot}$) in purple and the W7 model (Nomoto et al. 1984) in green. While our model produces a reasonable match to the strength and ratios of the Fe emission lines, it overproduces Ca emission when compared to normal SNe Ia. The W7 model which contains far less ^{40}Ca in its ejecta is a better fit.

sub-Chandrasekhar model for SN 2011fe, it is important to note that our models do produce the relative strengths of the 5270 Å and 4658 Å lines without this stable Fe present in the ejecta.

The 7290 Å feature is very sensitive to [Ca II] emission, but not exclusively. The double peaked nature of this emission feature in the W7 model (and in 2011fe) indicates there is very little contribution from [Ca II], but rather the feature is dominated by [Fe II] and [Ni II], while the Gaussian shape of the emission from our double detonation model at this wavelength indicates this emission feature in our models is dominated by [Ca II], which only is resolvable as a doublet for low ejecta velocities. Therefore we conclude (and agree with literature) that for normal SNe Type Ia the emission feature at 7200 Å likely has very little contribution from [Ca II] emission, and instead is primarily [Fe II] and [Ni II].

Recently Flörs et al. (2019) performed a study of nebular spectra produced by one-zone NLTE models, where the ejecta was composed of varying ratios of Fe, Ni, and Co. When fitting to a sample of normal Type Ia SNe they find that they can fit the feature at 7290 Å in normal SNe Type Ia with only [Fe II] and [Ni II] emission, and no contribution from [Ca II].

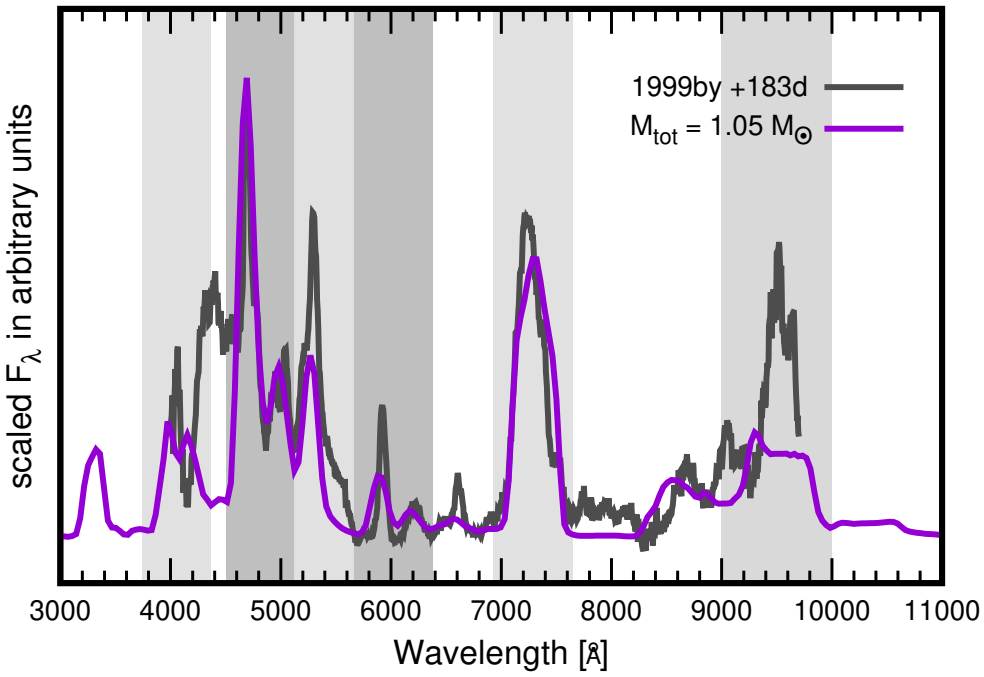

Figure 4.3: SN 1999by (a subluminous, 91bg-like SN Ia) compared with our model for a progenitor with a total mass of 1.05 $M_{\odot}$. Our model reproduces the strength of the emission feature at 7290 Å, but struggles with some of the features at the very blue and very red ends of the spectrum.

While this is likely the case for normal SNe Ia, the inferred masses of Ni and Fe indicated by the fits point to a sub-Chandrasekhar origin (by comparing to the nucleosynthetic yields of Ni and Fe for the sub-Chandrasekhar mass models of Shen et al. (2018a)). However, we find that the ^{40}Ca present in such models will produce flux in this region, which is not seen in these normal SNe Ia [1]. See Section 4.3 for a more detailed discussion on the Shen et al. (2018a) models.

4.2.3 Subluminous Type Ia SNe

The double detonation model provides a better fit to the nebular Ca emission seen in subluminous, or 91bg-like, SNe Type Ia. The bottom panel of Figure 4.3 shows a model comparison to SN 1999by (Silverman et al. 2012), a 91bg-like SN. We choose SN 1999by over SN 1991bg because of its better signal to noise ratio, particularly for wavelengths less than 6000 Å where the Fe emission features are prominent. Our model naturally produces the

[1]Here we define normal SNe Ia as SN 2011fe-like objects of magnitudes -19 mag and normal velocities ($v_{SiII} \approx$ 11,000 km/s). See Section 4.4 for more details.

strength and width of the [Fe II] and [Fe III] emission peaks as well as the strength of the 7290 Å emission feature (produced by [Ca II] in our models).

Mazzali & Hachinger (2012) investigate the nebular spectra of SN 1991bg using tomographic methods to determine an abundance and density profile for the ejecta. This study shows that lower central densities are required to reproduce the narrow Fe line emission features seen in this subluminous event, and these densities are consistent with both a sub-Chandrasekhar mass model and a WD merger model. However, they rule out the sub-Chandrasekhar model owing to a poor photospheric match to SN 1991bg. Our models, however, are a good fit for subluminous SNe Ia in the photospheric phase (Polin et al. 2019b), likely because we are comparing spectra for a lower mass object than the one chosen by Mazzali & Hachinger (2012).

It is worth also discussing the discrepancies in this fit. Two emission features are underproduced by our models, one at ∼4400 Å and one at ∼9500 Å. The 4400 Å emission is due to [Fe II] with a small contribution from [S II]. The fact that our models underproduce flux at this wavelength could be due to the stable Fe arguments made for SN 2011fe (see Section 4.2.2). However, this feature is also underrepresented in the Chandrasekhar mass models produced by Mazzali et al. (2015). More likely this discrepancy is a result of a limitation in the atomic data. The feature at 9500 Å is more puzzling. The emission in this region is primarily due to forbidden [S II] emission (Botyánszki & Kasen 2017). It is unclear why we underproduce this emission. It is possible that this is due to too little sulfur produced at the requisite densities in the ejecta. However, we do note that past studies have been successful in modeling the strength of the [S II] emission of SN 1999by with a sub-Chandrasekhar mass model, ignited as a pure central detonation with no helium on its surface, but those models also overproduced the [Ca II] emission at 7290 Å (Blondin et al. 2018).

4.3 [Ca II] Emission

Here we examine the striking feature in the synthesized nebular spectra: the [Ca II] emission line at 7290 Å. Figure 4.4 shows how the ratio of [Ca II] to [Fe III] λ4658 emission lines varies systematically with WD mass. The results can be fit with a sum of two exponentials, one representing a region of parameter space where the spectra are dominated by Ca emission (models with a total mass $\lesssim 0.98\ M_\odot$) and one describing the Fe dominated spectra (models with a total mass $\gtrsim 1.1\ M_\odot$). The transition between the two regimes occurs where the amount of intermediate mass elements produced by the progenitor is comparable to the mass of ^{56}Ni produced. This occurs for a progenitor of ∼1.0 $M_\odot$ (see Figure 2.2). For progenitors with masses greater than 1.0 $M_\odot$ the gains in ^{56}Ni are no longer exponentially increasing with the total mass and the relationship between Fe and Ca emission stays nominally constant.

The left panel of Figure4.4 shows an example of this fitting process for all models at 150 days after explosion. The right panel of Figure 4.4 shows the compiled fits across all nebular times with the thickness of the line being bound on top by the fit at day 450 and the bottom by day 150 post explosion. The shaded grey region represents an estimate of

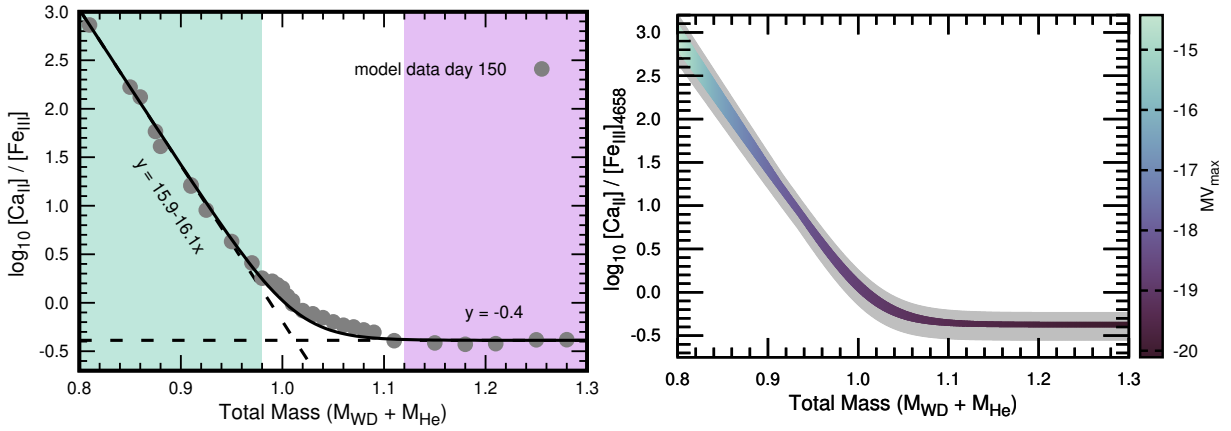

Figure 4.4: *Left*: The relationship between [Ca II]/[Fe III] to the total mass of the progenitor. Grey points show data for all models at 150 days after explosion. The two exponential fits delineate two regions of parameter space: one dominated by [Ca II] emission (shaded in green) and one with strong [Fe II] and [Fe III] emission features (shaded in purple). *Right*: The results of the same fits but for all nebular times. The width of the colored line represents the variation over modeled times. The curve is bounded on the bottom by models at 150 days after explosion and on top at day 450. The grey region represents the error bars due to uncertainties in atomic data, which is reported to be ∼30% in Botyánszki & Kasen (2017). Only a small variation in this ratio is measured over nebular times.

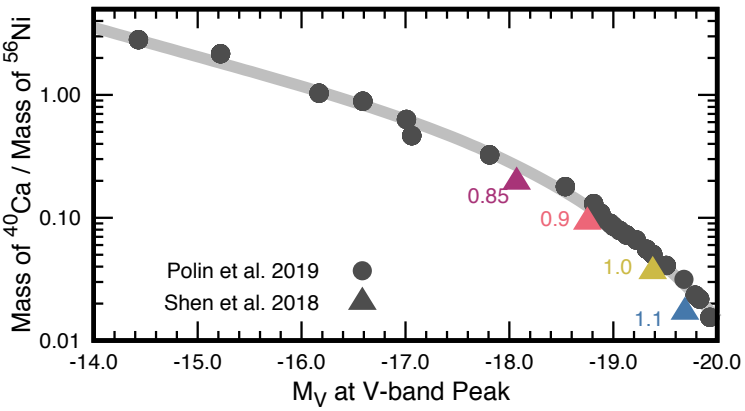

Figure 4.5: The ratio of the masses of ^{40}Ca to ^{56}Ni as a function of V-band magnitude for the Polin et al. (2019b) and Shen et al. (2018a) models. We show good agreement in composition yields when comparing models of similar peak brightness.

uncertainties in the modeled spectra due to uncertainties in atomic data (Botyánszki & Kasen 2017). We show only small variations in this modeled ratio over nebular times, making this measurement a good quantity to compare to data, as some flexibility in observational epoch may be allowed.

How much to trust this prediction boils down to how confident we are about the quantities of Ca and Fe group elements in the modeled SN ejecta. In Figure 4.5 we compare our ejecta models to those of Shen et al. (2018a) who used a sophisticated nuclear network to post-process yields for the detonations of bare sub-Chandrasekhar mass WDs (which lack helium on their surface and are ignited by a central detonation). We plot the ratio of ^{40}Ca to ^{56}Ni in the ejecta vs the V-band magnitude at time of V-band peak for all of our models (grey circles) and the Shen et al. (2018a) models (colored triangles). We choose the V-band for this comparison because it is most similar to the bolometric magnitude and it is free from any line blanketing effects caused by the helium shell ashes in our models, so we are free to compare them to the Shen et al. (2018a) models which lack helium shells. We see that the Shen et al. (2018a) models fall onto the relationship we map out relating the photospheric signatures (M_V) to the ejecta variables that control the [Ca II] emission in the nebular phase (the masses of ^{40}Ca and ^{56}Ni). The masses of these models do not perfectly align (the Shen et al. (2018a) 0.85 $M_\odot$ model looks like our 0.9 $M_\odot$ model) as mentioned by Polin et al. (2019b). However, the overall relationship is consistent. Given the mass ratios of ^{40}Ca and ^{56}Ni in the Shen et al. (2018a) models we expect to see this strong [Ca II] emission feature even for updated nuclear networks. Owing to the close agreement shown in Figure 4.5, we expect to see similar nebular spectra from models in both studies that correspond to the same peak luminosity.

4.4 Comparison to Data

In this Section we compare our model parameters to a set of 37 observed nebular SNe, and determine how the nebular phase can further help to identify SNe as deriving from double detonation progenitors.

4.4.1 Population of Observed Nebular SNe

We select a population of Type Ia SNe observed in the nebular phase by searching WISeREP, a public repository of SNe photometry and spectra (Yaron & Gal-Yam 2012), and selecting all SNe Type Ia observed between 120 and 320 days after peak brightness. We include all Types of SNe Ia (e.g, 91T-like, 91bg-like, and peculiar) as well as normal SNe Ia. We also searched the open supernova catalog (Guillochon et al. 2017) for any remaining SNe with nebular spectra from the population in Zheng et al. (2018). The result is 37 SNe Type Ia observed in the nebular phase, all of which are plotted in Figures 4.6 and 4.7. See Table 4.1 for a list of all SNe and associated references.

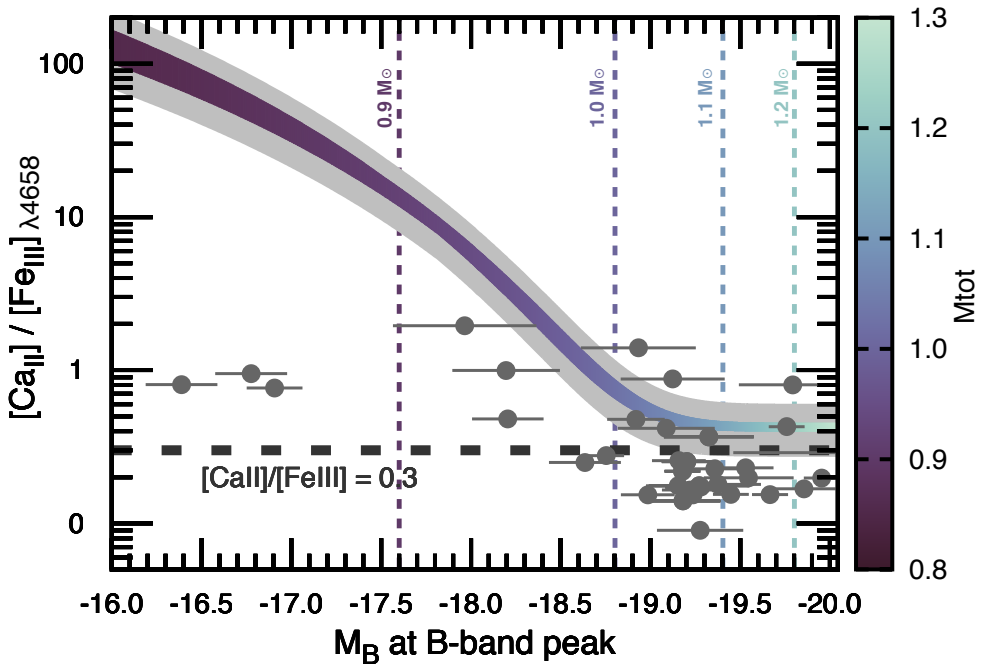

Figure 4.6: The modeled relationship between [Ca II]/[Fe III] λ4658 and M_B (at time of B-band peak) plotted with the nebular SNe data. The modeled relationship fits a family of SNe with magnitudes brighter than -19.0 mag, but no less luminous SNe fall on the modeled region. However, we do see a rise in the strength of the [Ca II] line (with respect to the [Fe III] line) occurring for SNe with magnitudes less than -19.0 mag matching the predicted behavior. The horizontal grey dashed line represents the minimum value for [Ca II]/[Fe III] expected from our models while considering the grey error regions.

4.4.2 [Ca II]/[Fe III] Ratio as a Function of Magnitude

In Figure 4.6 we compare the observed SNe data to our models by plotting the [Ca II]/[Fe III] ratio as a function of B-band magnitude at B-band peak. We convert between the total mass of our models and the B-band magnitude according to the results of the thin helium shell magnitudes modeled in the photospheric phase by Polin et al. (2019b).

Again the grey region represents the uncertainties in atomic data from Botyánszki & Kasen (2017). The results show a trend in the increase of [Ca II] emission for masses $\lesssim 0.98$ $M_\odot$ as predicted by our models. The magnitude of the [Ca II] features is overpredicted by our models at these lower masses. For more luminous SNe (magnitudes brighter than -19.0) we see examples of SNe with comparable and even more extreme [Ca II]/[Fe III] ratios than our models predict. On the low luminosity end we overpredict the strength of the [Ca II] line compared to the observed SNe Type Ia.

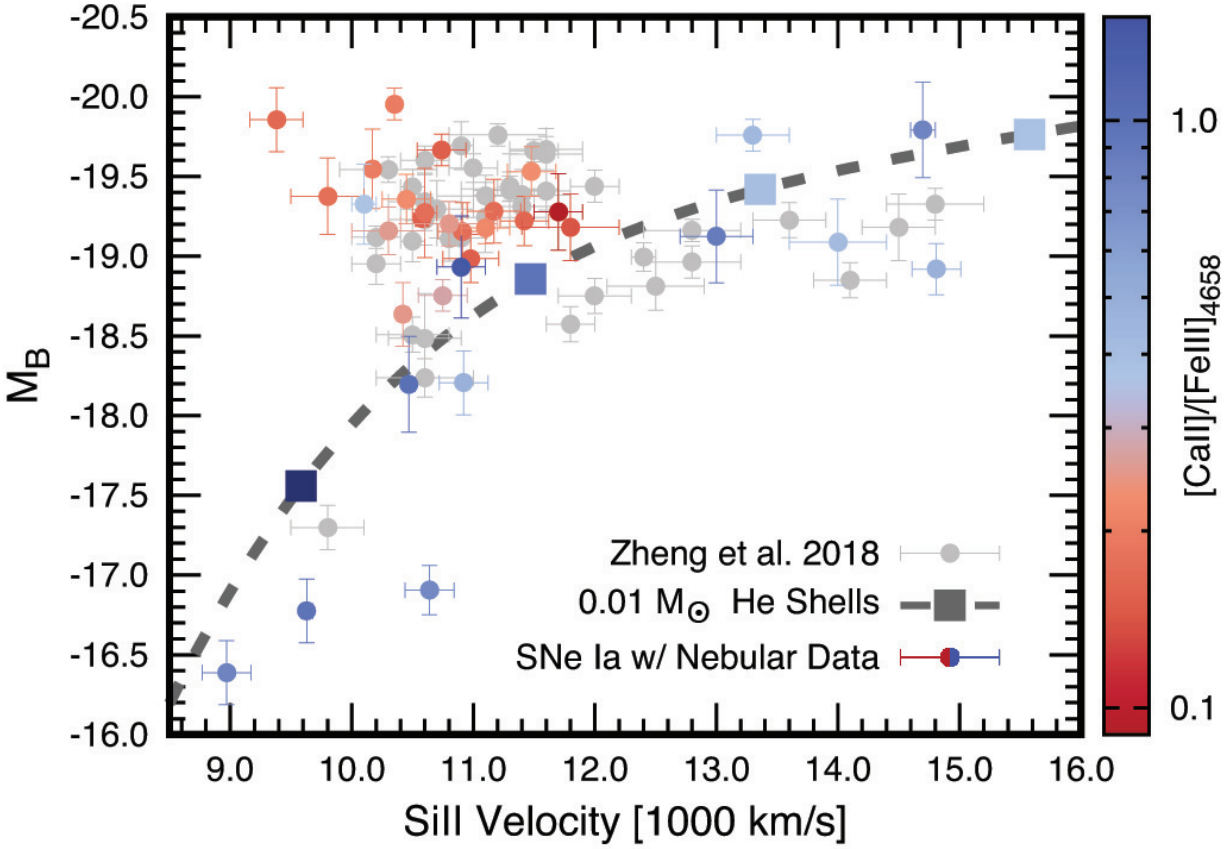

Figure 4.7: B-band magnitude vs. Si II velocity (both at time of B-band peak brightness) for an observed population of SNe Type Ia. Polin et al. (2019b) suggest that this relationship is evidence of two classes of SNe Ia; those that follow the modeled relationship may be identified as sub-Chandrasekhar mass progenitors and those that lie in the cluster as Chandrasekhar mass origin. All of the SNe that follow the modeled relationship have a stronger contribution of [Ca II] emission than those in the cluster, supporting the hypothesis that these are the SNe Type Ia originating from a double detonation mechanism. The colorbar transition from red to blue is placed at a value of [Ca II]/[Fe III]=0.3, corresponding to the minimum expected value from our models.

4.4.3 Si II Velocity Relationship: Which SNe Ia are Double Detonations?

Here we examine the consistency of our nebular predictions with the population of SNe Type Ia that Polin et al. (2019b) point to as the likely candidates for sub-Chandrasekhar mass double detonations. This population is identified by their relationship between Si II velocity and B-band magnitude, both at time of B-band peak. Polin et al. (2019b) identify two distinct populations of SNe Type Ia. One group follows the relationship modeled by the double

detonation models, and contains SNe at both high and low Si II velocities. These are the SNe Type Ia that may originate from a sub-Chandrasekhar mass double detonation progenitor. The other group clusters tightly around $M_B \sim$ -19.5 mag and $v_{SiII} \sim$ 11,000 km/s outside of the allowed relationship for double detonations. Recently Cikota et al. (2019) examined this relationship using an additional population of SNe Ia and show that this trend persists in their data, although the outliers are not as easily identifiable around the Chandrasekhar mass cluster. Furthermore, when they examine spectropolarimetry measurements of the Si II line polarization they yet again find a distinction between the cluster (which have lower polarization measurements) and the SNe that follow the predicted sub-Chandrasekhar mass relationship (which have higher polarization measurements).

We reproduce this plot in Figure 4.7 with all of our nebular data colored by [Ca II]/[Fe III] emission. Grey points show the Zheng et al. (2018) data for which no nebular spectra were available. We see that this trend of outliers is further delineated by their nebular features. All of the Si II velocity outliers that lie along the modeled sub-Chandrasekhar mass sequence show a [Ca II]/[Fe III] ratio greater than 0.3 while the majority of the SNe in the cluster show a weaker [Ca II] contribution. This cutoff is the same as indicated by the minimal expected value for the ratio of [Ca II]/[Fe III] (see the dashed line in Figure 4.6). The 0.01 $M_\odot$ helium shell models are plotted as squares along a spline fit to the model data shown as a dashed grey line. From left to right the plotted models are 0.9 $M_\odot$, 1.0 $M_\odot$, 1.1 $M_\odot$, and 1.2 $M_\odot$ WDs. The 0.9 $M_\odot$ model, having [Ca II]/[Fe III] $\sim$ 10 does overproduce [Ca II] emission when compared to any observed SNe Type Ia, however higher mass models are consistent with the data. We stress that these objects are now delineated by four different features: velocity, color (Polin et al. 2019b), polarization (Cikota et al. 2019), and nebular [Ca II] emission. We are confident that we now distinguish two distinct classes of SNe Type Ia that differ by their physical origin.

4.5 Discussion

In this study we performed a systematic survey of double detonation models in the nebular phase. We showed that these models can qualitatively reproduce subluminous SNe Ia spectra in the nebular phase, but overproduce [Ca II] emission compared to most normal SNe Type Ia. The ratio of [Ca II] to [Fe III] emission as a function of total mass can be used as a diagnostic to determine if a SN Ia can result from a sub-Chandrasekhar mass progenitor. When we examine this ratio compared to the peak B-band magnitude of our models it further supports the conclusions of Polin et al. (2019b) that a population of SNe Type Ia with sub-Chandrasekhar mass double detonation progenitors can be identified by their relationship between Si II velocity and B-band magnitude. This is now the fourth axis by which these groups differentiate from each other: the luminosity-magnitude relationship (Polin et al. 2019b), the peak colors (Polin et al. 2019b), the spectrapolarimetry measurements (Cikota et al. 2019) and now the nebular features differentiate these two groups of SNe. This strongly supports that two distinct classes of SNe Type Ia can be identified by where they fall on this

Table 4.1: List of SNe with Nebular Spectra.

SN	Figures	Database	Citation(s)
SNe from Zheng et al. (2018):			
2000cx	4.6,4.7	OSC	Silverman et al. (2012), Li et al. (2001)
2001ep	4.6,4.7	OSC	Silverman et al. (2012)
2002bo	4.6,4.7	OSC	Blondin et al. (2012), Matheson et al. (2008)
2002dj	4.6,4.7	OSC	Pignata et al. (2008)
2002er	4.6,4.7	WISeREP	Kotak et al. (2005)
2002fk	4.6,4.7	OSC	Hicken et al. (2009)
2003cg	4.6,4.7	OSC	Elias-Rosa et al. (2006)
2004dt	4.6,4.7	OSC	Silverman et al. (2012)
2004eo	4.6,4.7	WISeREP	Pastorello et al. (2007)
2005cf	4.6,4.7	WISeREP	Wang et al. (2009b)
2005ki	4.6,4.7	WISeREP	Folatelli et al. (2013)
2006X	4.6,4.7	WISeREP	Wang et al. (2008)
2007af	4.6,4.7	WISeREP	Silverman et al. (2012)
2007le	4.6,4.7	OSC	Silverman et al. (2012)
Additional Nebular SNe Type Ia:			
1986G	4.6,4.7	WISeREP	Cristiani et al. (1992)
1990N	4.6,4.7	WISeREP	Gómez & López (1998)
1991T	4.1,4.6,4.7	WISeREP	Gómez & López (1998)
1991bg	4.1,4.6,4.7	OSC	Turatto et al. (1996)
1994ae	4.6,4.7	WISeREP	Silverman et al. (2012)
1995D	4.6,4.7	WISeREP	Blondin et al. (2012)
1996X	4.6,4.7	WISeREP	Salvo et al. (2001)
1998aq	4.6,4.7	WISeREP	Branch et al. (2003)
1998bp	4.6,4.7	WISeREP	Silverman et al. (2012)
1998bu	4.6,4.7	WISeREP	Matheson et al. (2008)
1999aa	4.6,4.7	WISeREP	Silverman et al. (2012)
1999by	4.1,4.3,4.6,4.7	WISeREP	Silverman et al. (2012)
2000E	4.6,4.7	WISeREP	Blondin et al. (2012)
2002cs	4.6,4.7	WISeREP	Silverman et al. (2012)
2002dp	4.6,4.7	WISeREP	Silverman et al. (2012)
2003du	4.6,4.7	WISeREP	Anupama et al. (2005)
2003hv	4.6,4.7	WISeREP	Leloudas et al. (2009)
2005ke	4.6,4.7	WISeREP	Folatelli et al. (2013)
2006D	4.6,4.7	WISeREP	Silverman et al. (2012)
2007if	4.6,4.7	WISeREP	Blondin et al. (2012)
2008A	4.6,4.7	WISeREP	McCully et al. (2014)
2008Q	4.6,4.7	WISeREP	Silverman et al. (2012)
2011fe	4.1,4.2,4.6,4.7	WISeREP	Mazzali et al. (2015)
Additional Spectra:			
2005cz (Ca-rich transient)	4.1	OSC	Kawabata et al. (2010)

Note. — The OSC refers to the Open Supernova Catalog (Guillochon et al. 2017), and the figures column refers to the figure in which the spectrum or data taken from the spectrum appear.

relationship.

Nebular spectra are a powerful probe of the internal structure of SNe, including any asymmetries in the geometry of the ejecta. This study has been performed with 1D hydrodynamic models and we plan to perform future studies to examine the consequences of any asymmetries that may be present in multidimensional simulations.

Chapter 5

The Discovery of Double Detonations Triggered by Thick Helium Shells

During my tenure at Berkeley the first example was found of a transient which exhibits all of our predictions for the signatures of a double detonation triggered by a thick helium shell. To date there are only three strong candidates for these thick shell explosions. This section serves to summarize these discoveries and the role our double detonation models played in the process of identifying these events.

5.1 SN 2018byg (ZTF 18aaqeasu)

The content of this chapter is drawn from De et al. (2019), with permission from the co-authors.

Here, we discuss the discovery of SN 2018byg (SN 2018byg/ATLAS 18pqq), a peculiar Type I SN, consistent with being a helium-shell double-detonation. With a rise time of $\sim$ 18 days from explosion, the transient reached a peak absolute magnitude of $M_R \sim -18.2$ mag, exhibiting a light curve akin to sub-luminous SN 1991bg-like Type Ia supernovae, albeit with an excess of flux throughout the rise time. Spectra taken near peak light exhibit prominent Si absorption features together with an unusually red color ($g-r \sim 2$ mag) arising from nearly complete line blanketing of flux blue-wards of 5000 Å. This behavior is unlike any previously observed thermonuclear transient. Spectra taken at and after $\sim$ 30 days from peak light reveal evidence of a thermonuclear detonation event dominated by Fe-group nucleosynthesis. We show that the peculiar properties of SN 2018byg are consistent with the detonation of a massive ($\sim 0.15\,M_\odot$) helium shell on a sub-Chandrasekhar mass ($\sim 0.75\,M_\odot$) WD. These observations provide evidence of a likely rare class of thermonuclear supernovae arising from double detonations triggered by massive helium shells.

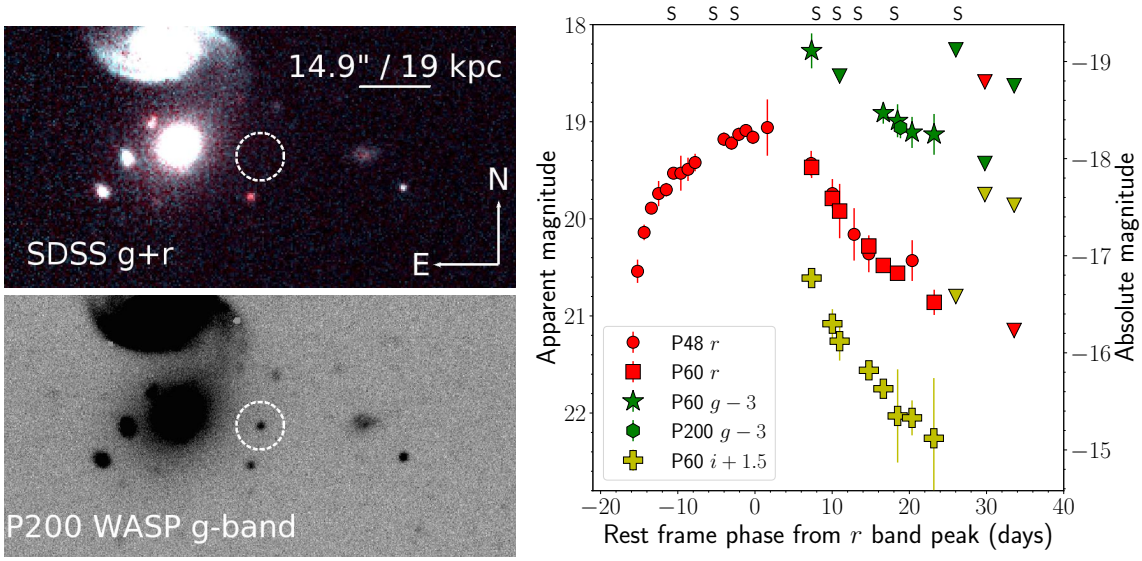

Figure 5.1: (Left) Detection field and host galaxy of SN 2018byg. The top panel is an archival SDSS image of the region while the lower panel shows an image taken while the SN was bright. The location of the transient is marked with the white circle - it is at a projected offset of $\sim 17.2''$corresponding to a physical projected distance of 21.9 kpc at the host galaxy redshift. (Right) Multi-color light curves of SN 2018byg. The inverted triangles are upper limits. The epochs of spectroscopy are marked with 'S' on the top axis. Figure taken from De et al. (2019) with permission of the co-authors.

5.1.1 Photometric Properties

The photometry and location for SN 2018by are shown in Figure 5.1, photometric observations began around 15 days before peak brightness in the r-band and were joined by g- and i-band observations at time of peak brightness. This event was sub-luminous compared to normal Type Ia SNe, exhibiting a maximum r-band magnitude of -18.2mag, more akin to a 91bg-like Ia. We compare the r-band photometry to both normal and 91bg-like SNe Ia in Figure 5.2. The source exhibited an initial fast rise (at < -10 days from peak) of about 0.4 mag per day, similar to the normal Type Ia SNe but subsequently slowed in its rise transitioning to a sub-luminous SN Ia light curve.

Although we do not have multi-color photometric coverage before the peak of the r-band light curve, we use our well sampled sequence of spectra to construct pre-peak color curves for the transient. Figure 5.2 we shows our $g-r$ and $r-i$ color curves of the transient constructed by performing synthetic photometry on the spectra, while adding a 10% uncertainty on the measurements to account for potential inaccuracies in flux calibration. While the colors of SN 2018byg are consistent with other SNe Ia in the region post maximum light the early g-r colors are redder than a typical sub-luminous Ia by approximately 1.5 mag. Both the flux excess throughout the early rise, and early red colors, serve to distinguish SN 2018byg from

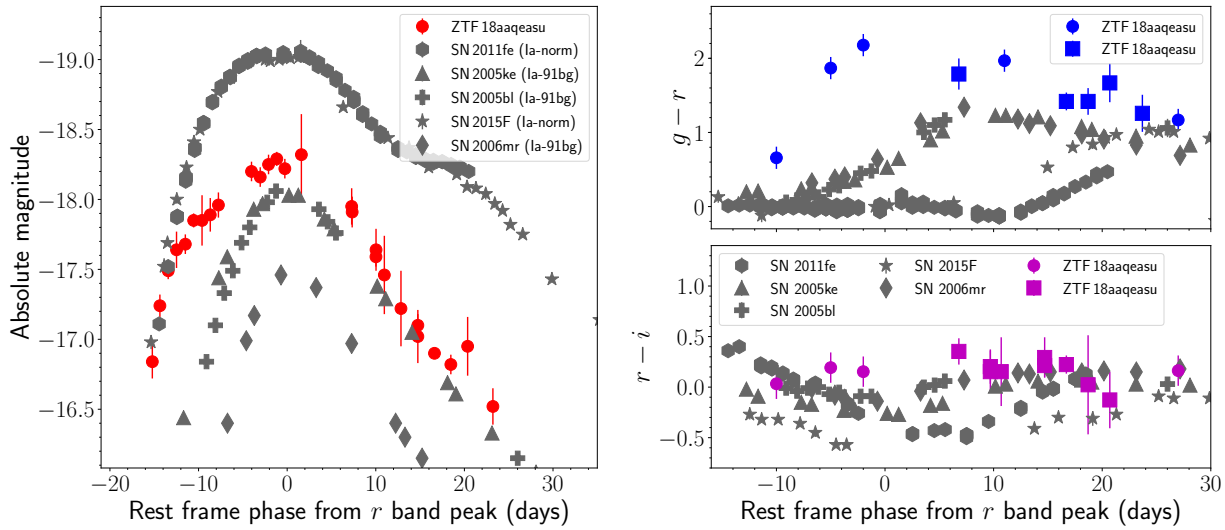

Figure 5.2: (Left) Comparison of the r-band light curve of SN 2018byg to other normal and sub-luminous Type Ia SNe. The r-band light exhibits an excess in flux in the early rise not present in other SNe Ia, before reaching a peak magnitude consistant with 91bg-like SNe Ia and a typical decline. (Right) Comparison of the $g-r$ and $r-i$ color evolution of SN 2018byg (circles are colors derived from spectra while squares denote colors from photometry) to the same sample of SNe as in the left panel. Figure taken from De et al. (2019) with permission of the co-authors.

other sub-luminous SNe Ia photometrically.

5.1.2 Spectroscopic Properties

SN 2018byg becomes more peculiar when examined spectroscopically. Figure 5.3 shows the spectroscopic evolution of this event with spectra taken from -10 days before r-band peak to $+52$ days. The earliest spectrum exhibits a blue continuum, with broad absorption features bluewards for 5000Å, and a broad Ca II absorption feature at 8500 Å. Figure 5.4 shows the spectra of SN18byg compared with other SNe Ia. We note that this earliest spectrum differs from that of any other Ia sub-class, lacking the Si II features characteristic of the normal and sub-luminous SNe Ia at this epoch. While 91T-like SNe Ia also lack these Si II features, SN 2018byg exhibits stronger Fe-group absorption features and blanketing in the blue parts of the spectrum.

By the time SN 2018byg reaches peak brightness the spectrum does develop IME absorption features, mainly the Si II doublet. Using the minimum of the Si II P-Cygni profile, we measure a photospheric velocity of $\sim 10,500\,\mathrm{km/s}$. The peak spectrum also exhibits a deep, broad, high velocity ($\sim 25,000\,\mathrm{km/s}$) Ca II absorption feature at 7500–8500 Å. What is most unusual about the peak spectrum of SN 2018byg is that the bluer parts of the spectrum

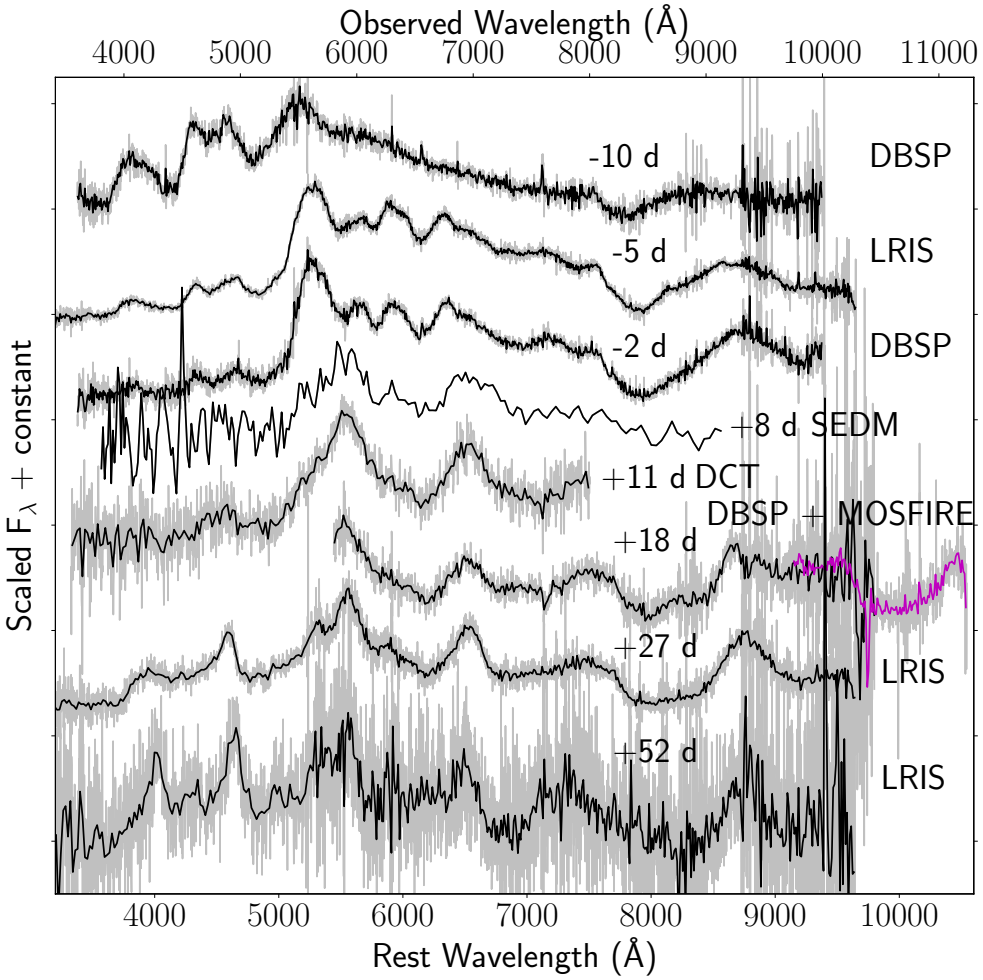

Figure 5.3: Spectroscopic sequence of SN 2018byg. Phases with respect to r-band peak and instruments used are indicated next to each spectrum. The black lines are binned from the raw spectra shown in gray lines. SN 2018byg exhibits strong line blanketing in the blue part of the spectrum throughout it's evolution. Figure taken from De et al. (2019) with permission of the co-authors.

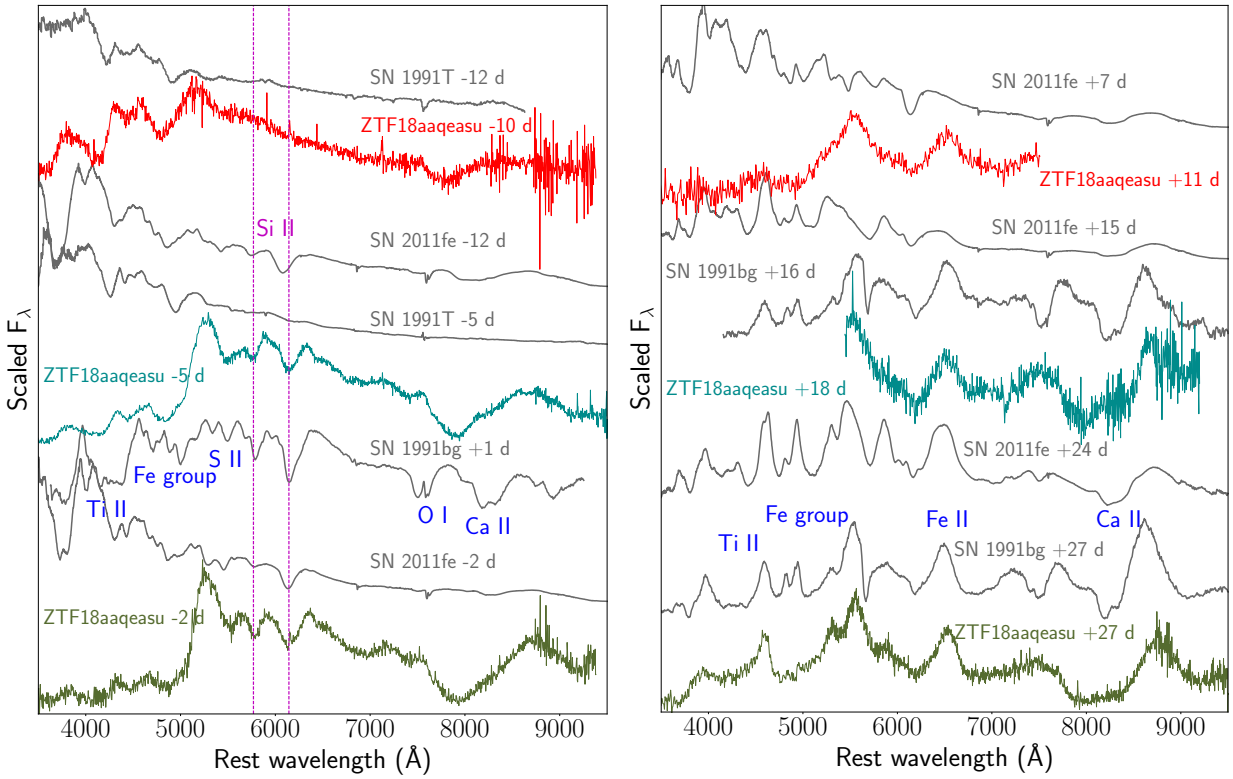

Figure 5.4: Comparison of the pre-maximum (left) and post-maximum (right) spectra of SN 2018byg (ZTF18aaqeasu) to the normal Type Ia SN 2011fe (Maguire et al. 2014), the over-luminous SN 1991T (Filippenko et al. 1992a) and the sub-luminous SN 1991bg (Filippenko et al. 1992b). The magenta dashed lines in the left panel indicate Si II lines at a velocity of 10,000 km s^{-1}. Prominent emission / absorption features are marked in both panels. Spectroscopic data for the comparison SNe were obtained from the WISEReP repository (Yaron & Gal-Yam 2012). Figure taken from De et al. (2019) with permission of the co-authors.

exhibit unusually strong line blanketing features leading to nearly complete absorption of flux blue-wards of 5000 Å. Comparing with the sub-luminous Type Ia SN 1991bg at a similar phase, we attribute this absorption to complete line blanketing by Fe group elements and Ti II. To our knowledge, such strong line blanketing features (and consequent red $g-r$ colors) have never been previously seen in any variant of a Type Ia SN at peak light.

Post-maximum spectra starting from ~ 10 days after peak begin to develop broad emission features suggesting a transition to the optically thin phase. The only NIR spectrum taken at +18 days exhibits a deep absorption feature at ~ 9950 Å. If associated with He I at 1.083 μm, the corresponding absorption velocity would be $\sim 26,000$ km/s. Spectra obtained at ~ 27 and ~ 52 days after peak are similar to the Type Ia SN 1991bg at similar phases, and exhibit emission lines of Fe group elements, Ti II and Ca II. The late-time similarities and Fe-group dominated nucleosynthesis suggest a thermonuclear origin of the explosion, consistent with SN 2018byg representing an unusual variant of a Type Ia-like SN. However, the peculiar spectral features observed at peak light are unique to SN 2018byg and warrant further inspection with respect to a possible explosion mechanism.

5.1.3 Model Comparisons

SN 2018byg exhibits features unlike any typical Ia both photometrically and spectroscopically. Any suggested progenitor must explain the early flux excess in the r-band photometry, as well as the significantly line blanketed spectrum (and consequently the early red colors). These are all features predicted in Polin et al. (2019b) (and discussed in Chapter 3) as "smoking gun" signatures of a double detonation explosion triggered by a thick helium shell ignition. Here we examine this progenitor as a possible origin for SN 2018byg.

The strong line blanketing features of Fe group elements observed in the peak spectra suggest that the outer layers of the ejecta are unusually rich in Fe group elements. The presence of such radioactive material in the outer ejecta would also be consistent with the fast rise observed in the early light curve (Piro & Nakar 2014), and is a hallmark signature of the decay of radioactive elements in the outermost ejecta (primarily ^{48}Cr and ^{52}Fe with half-lives of 0.90 days and 0.35 days respectively) for an explosion powered by a He shell detonation (e.g. Nugent et al. 1997; Kromer et al. 2010; Polin et al. 2019b). This scenario would naturally explain the high velocity Ca II features observed near peak light, as a known He detonation product in the outer layers of the ejecta (Fink et al. 2010; Kromer et al. 2010; Polin et al. 2019b).

We begin the modeling process with photometry alone. For any given (well resolved) light curve there is only one model within our parameter space of double detonations that will fit the photometric evolution. The peak of the light curve is determined entirely by the amount of ^{56}Ni produced in the center of the explosion, which is consequently determined by the total mass of the progenitor (M_{WD}+M_{He}). The magnitude of the early flux excess is determined by the radioactive material (^{48}Cr, ^{52}Fe, and ^{56}Ni) produced in the shell burning which is simply a function of the density at the base of the helium shell (determined by both

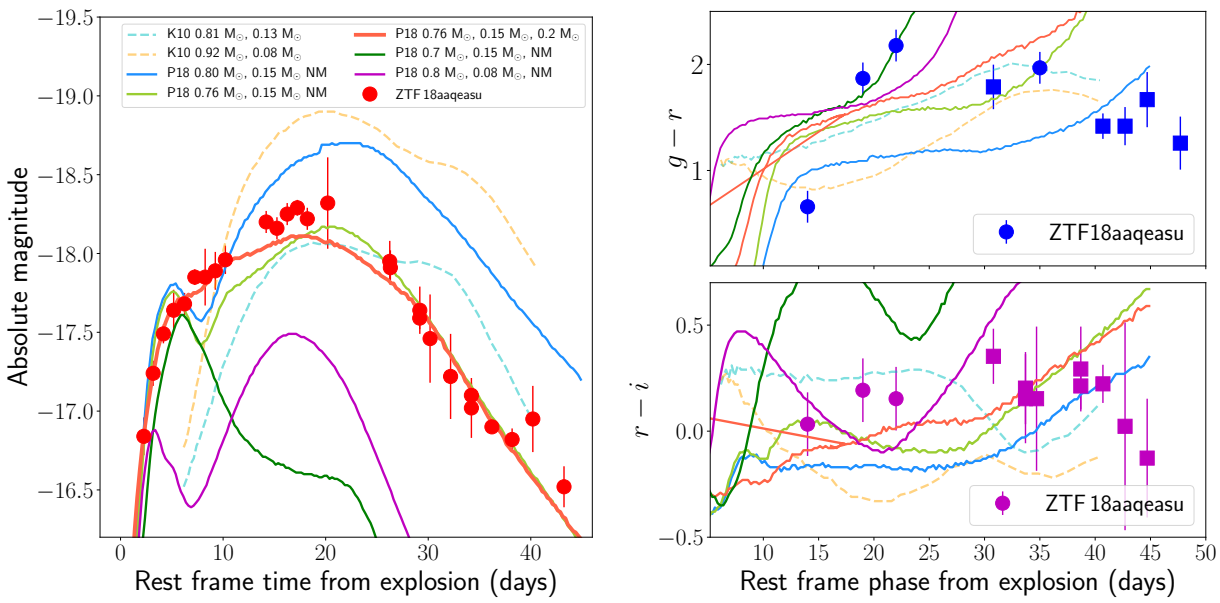

Figure 5.5: Comparison of the photometric evolution of SN 2018byg with that of the He shell double detonation models in Kromer et al. (2010) (K10; dashed lines) and Polin et al. (2019b) (P18; solid lines). The model parameters are indicated in the legend as (WD mass, shell mass, mixing length), and where NM stands for No Mixing. The left panel shows the r-band evolution while the right panels show the $g-r$ and $r-i$ color evolution with the same color schemes for the models. On the right panel, circles denote colors derived from the spectra while squares denote colors derived from photometry. We find a best fit model for a 0.76 $M_\odot$ WD with a 0.15 $M_\odot$ helium shell and mixing length of 0.2 $M_\odot$. Figure taken from De et al. (2019) with permission of the co-authors.

M_{WD} and M_{He}). So for a given light curve there is only one M_{WD}+M_{He} combination that will match its evolution.

We compare the light curves to the larger grid of shell and WD masses presented in the simulations of Polin et al. (2019b), including additional simulations performed to match the data as solid lines in Figure 5.5. We note that a model involving a fixed WD mass of 0.8 $M_\odot$ and a shell of 0.15 $M_\odot$ shell reasonably reproduces the early rise, while the same WD with a smaller 0.08 $M_\odot$ shell under-predicts the r-band luminosity on the early rise. We then constrain the WD mass to be between 0.7 and 0.8 $M_\odot$ by noting that models involving a 0.8 $M_\odot$ WD and 0.7 $M_\odot$ WD (each with a 0.15 $M_\odot$ shell) have a higher and lower peak luminosity than SN 2018byg respectively. With these constraints, we find that a model with a 0.76 $M_\odot$ WD and a 0.15 $M_\odot$ shell reproduces the overall r-band evolution. The corresponding synthesized ^{56}Ni mass is 0.18 $M_\odot$.

The light curves in these models also exhibit an early peak and decline, arising from the decay of radioactive material in the outer ejecta and the assumption of no mixing. Although

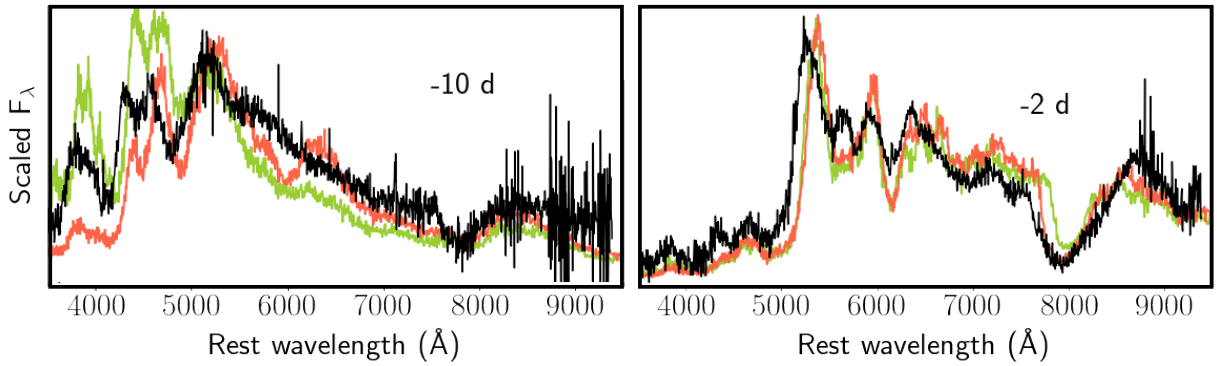

Figure 5.6: Comparison of the spectra of SN 2018byg at and before peak light (shown as black lines) to models of He shell double detonations from Polin et al. (2019b) for two cases of ejecta mixing (mixed in green and unmixed in red) with the best fit WD and shell mass from the light curves (a 0.76 $M_\odot$ WD w/ 0.15 $M_\odot$ helium shell). In both panels, the epochs of spectroscopic comparison are indicated according to the phase of the light curve (days from r-band peak). Figure taken from De et al. (2019) with permission of the co-authors.

we do observe signatures of a fast rising early peak, we do not have evidence of a decline as in the models, suggesting a possible influence of mixing in the ejecta. Hence, we also show an additional model with the best-fit WD mass and shell mass, but with ejecta mixed across a region of $0.18\,M_\odot$ that is applied before performing the radiative transport. This model reproduces the early-time rise and the overall light curve. Although the red colors of the source near peak light are also well reproduced, the models become redder with time much faster than observed in the data. These discrepancies likely arise due to assumptions of local thermodynamic equilibrium (LTE) in `Sedona`, which break down as the starts to become optically thin at ~ 20 days after peak light.

Once a preferred model was determined via comparison to the photometry we compared the spectroscopic properties of SN 2018byg to simulated double detonation. We find a match to the observed spectra both before and at peak light (Figure 5.6). In the case of the early spectra (~ 10 days before peak), the models exhibit blue continua in the unmixed case similar to the data, although the absorption features become more prominent in the case of mixed ejecta as expected. The peak light spectra (~ 2 days before peak) are well reproduced both in terms of line velocities and strengths, and are not appreciably affected by mixing in the ejecta. Taken together, we find that a model involving the detonation of a $\sim 0.15\,M_\odot$ He shell on a $\sim 0.75\,M_\odot$ WD reproduces the observed signatures of the event after including mixing of $\sim 0.2\,M_\odot$ in the outer ejecta. Figure 5.7 summarizes both the photometric and spectroscopic comparisons with our favored model.

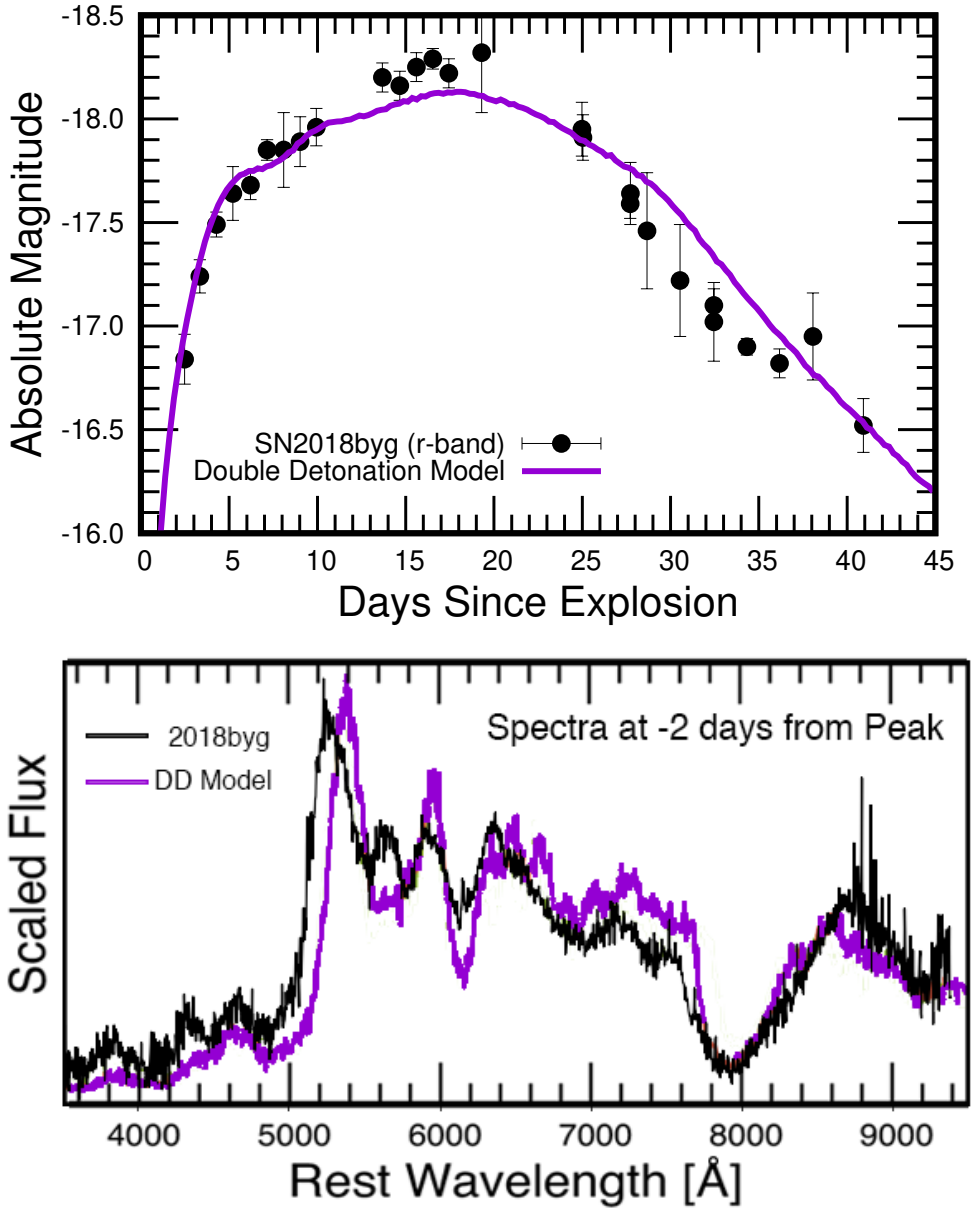

Figure 5.7: Light curve (top) and peak spectra (bottom) from De et al. (2019) showing our best fit model (purple) compared with the observed data for SN 2018byg (black). Our modeled light curve shows a good match to the magnitude of both the early flux excess (at ∼5 days) and the peak luminosity (at ∼17 days). Our synthetic spectrum shows the ashes blanketing wavelengths less than 5000 Å and also produces absorption features at the observed strengths and velocities.

5.1.4 Discussion

We have presented observations of the transient SN 2018byg, and have shown it to be a unique supernova. While its photometric and nucleosynthetic properties share several similarities to subluminous Type Ia SNe, its peak photospheric spectra are marked by extremely strong line blanketing features and red colors, unlike any previously observed Type Ia SN. By comparing the data to a grid of models, we show that the observed properties can be well explained by the detonation of a massive ($\sim 0.15\,M_\odot$) He shell on a sub-Chandrasekhar mass ($\sim 0.75\,M_\odot$) white dwarf. In particular, it is important to note that the He shell mass inferred is much larger than the thin He shells required to explain the properties of the broader population of Type Ia SNe ($\lesssim 0.01\,M_\odot$;Kromer et al. 2010; Sim et al. 2010; Shen et al. 2018a; Polin et al. 2019b).

The inferred shell and core masses are consistent with what is predicted in the well studied He burning star donor scenario of a $0.48\,M_\odot$ sdB star losing matter to a C/O WD (Nomoto 1982b; Woosley & Weaver 1994; Woosley & Kasen 2011). While much of the early work assumed a constant accretion rate, more recent calculations (Brooks et al. 2015; Bauer et al. 2017) have self consistently calculated the evolution of the donor with mass loss and a self-consistent varying accretion rate. The properties inferred for SN 2018byg are remarkably close to the recent calculation of Bauer et al. (2017) for the evolution of the known sdB + WD binary CD $-30°11223$ (Geier et al. 2013), with Bauer et al. (2017) finding a He shell mass of $0.16\,M_\odot$ on the initial WD of mass $0.76\,M_\odot$ at the time of detonation. As this is the forward evolution of a known system, it's possible to say that CD $-30°11223$ is indeed an example of the progenitor of SN 2018byg-like events.

The relatively luminous and slow evolving light curve of SN 2018byg (compared to e.g. SN 1991bg-like events) suggests that similar events should be easily detectable in a reasonably large volume of the local universe (out to $z \sim 0.1$ for a limiting magnitude of $r = 20.5\,\mathrm{mag}$). However, no such event has been reported in previous studies of large samples of thermonuclear SNe (e.g., Hicken et al. 2009; Maguire et al. 2014; Krisciunas et al. 2017; Scolnic et al. 2018). To date, tentative evidence for only one other example of a relatively thin He shell detonation has been presented in Jiang et al. (2017) (see also Polin et al. 2019b), although their modeling implies a more massive WD with a smaller He shell than is needed to explain SN 2018byg. Thus, SN 2018byg being the first of its kind suggests that massive He shell double detonations must be intrinsically rare in the population of thermonuclear SNe.

5.1.5 Nebular Modeling and Potential Connection to Ca-rich Transients

The content of this section is drawn from (Polin et al. 2019a), with permission from the co-authors.

SN 2018byg (ZTF18aaqeasu) (De et al. 2019) was a peculiar Type I SN found in the outskirts of its host galaxy. Features in both the light curve and spectra distinguished this

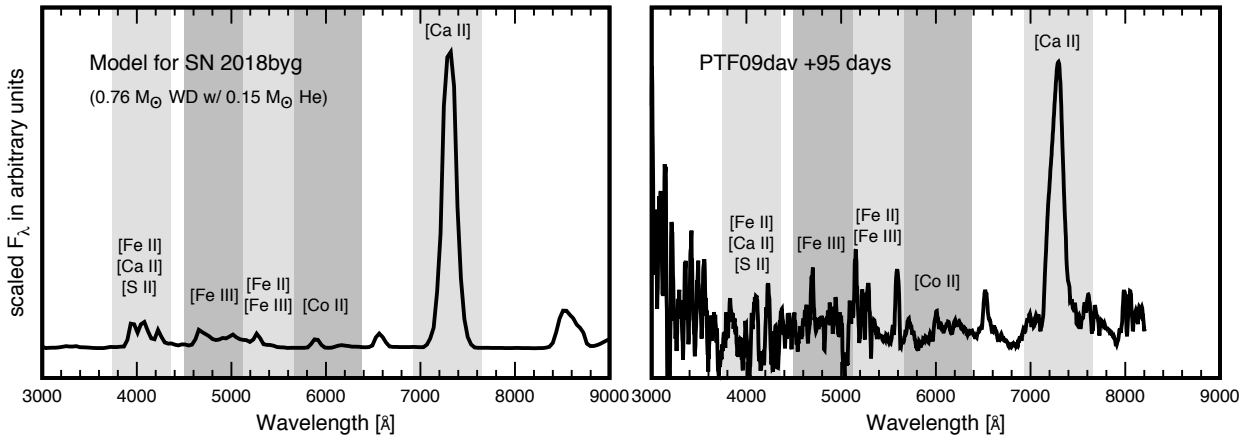

Figure 5.8: *Left:* The Polin et al. (2019b) model used to fit SN 2018byg (ZTF18aaqeasu) in the photospheric phase followed through to the nebular phase. We predict that this peculiar event would fall into the regime where the nebular spectrum is dominated by [Ca II] emission. *Right:* PTF09dav, a Ia-like Ca-rich transient, shown at +95 days from peak light when the nebular spectrum cools primarily through [Ca II] emission.

as an unusual event. The light curve exhibited a rapid rise that turned out to be an excess in flux over the first few days post explosion. Spectra taken during this time show a blue continuum with some broad absorption features bluer than 5000 Å. At peak the r-band photometry reached a maximum brightness of -18.27 ± 0.04 mag, sub-luminous for a Type Ia, but typical for a 91bg-like Type Ia. The spectra at peak best serve to distinguish this event as unusual. The blue part of the spectrum exhibited extreme line blanketing, nearly extinguishing all flux for wavelengths less than 5000 Å, and wavelengths red of this sharp cutoff exhibit absorption features from Si II and a broad Ca II absorption feature. These were all features predicted by Polin et al. (2019b) as "smoking gun" signatures of a double detonation resulting from the ignition of a thick helium shell.

De et al. (2019) presented a custom model which was created following the methods of Polin et al. (2019b) which showed all of these peculiarities for a 0.76 $M_{\odot}$ WD with a 0.15 $M_{\odot}$ helium shell. In the model the early flux excess was produced by the radioactive decay of elements produced during the burning of the massive helium shell, and the extreme line blanketing was caused by those same optically thick helium ashes which reside in the outer most SN ejecta. The velocity and strength of the Ca II absorption feature was well modeled, with the 0.035 $M_{\odot}$ of ^{40}Ca produced during nucleosynthesis.

In Figure 5.8 we show the consequences of running the model for SN 2018byg into the nebular phase. The total mass of the model (0.9 $M_{\odot}$) places it in the [Ca II] dominated regime. While no nebular spectra were taken for this event, we propose that the result would have categorized this event as Ca-rich. We predict that the next such 18byg-like event should exhibit strong [Ca II] emission features in the nebular phase.

Chapter 6

Relating Double Detonations to Ca-Rich Transients

Our work modeling sub-Chandrasekhar mass WD explosions in the nebular phase revealed that an order of magnitude less Ca is required to produce a Ca-rich transient than was previously accepted in the literature (Polin et al. 2019a). In Section 6.1 we discuss those results and the implications for the understanding of Ca-rich SNe. In Section 6.2 we discuss SN 2016hnk, a peculiar Ca-rich SN which resembles SN 2018byg in origin and indicates we are on the right track when linking double detonations to Ca-rich features in the nebular phase.

6.1 Implications of Nebular Double Detonations for Ca-Rich Transients

The content of this section is drawn from Polin et al. (2019a), with permission from the co-authors.

Here we examine the implications of our results for Ca-rich transients. ^{40}Ca is produced via the double detonation mechanism in quantities greater than in a standard Chandrasekhar mass model for a Type Ia SN. For example the W7 model has 0.01 $M_{\odot}$ ^{40}Ca whereas our models can produce up to a factor of four times that amount. This occurs because less massive WDs have larger radii and lower densities than more massive WDs. So, our models allow for an more burning within these lower density regions that produce IMEs than in a Chandrasekhar mass WD. Figure 6.1 shows the mass of ^{40}Ca produced as a function of total model mass (most of which is created during the burning of the WD rather than from the helium shell). The amount of ^{40}Ca synthesized increases with total mass total mass of the progenitor until we reach a mass of 1.0 $M_{\odot}$. At this point the amount of ^{40}Ca in the ejecta peaks and begins decreasing as we continue to increase the progenitor mass. This occurs because as we increase the density of the progenitors, α-chain burning becomes more

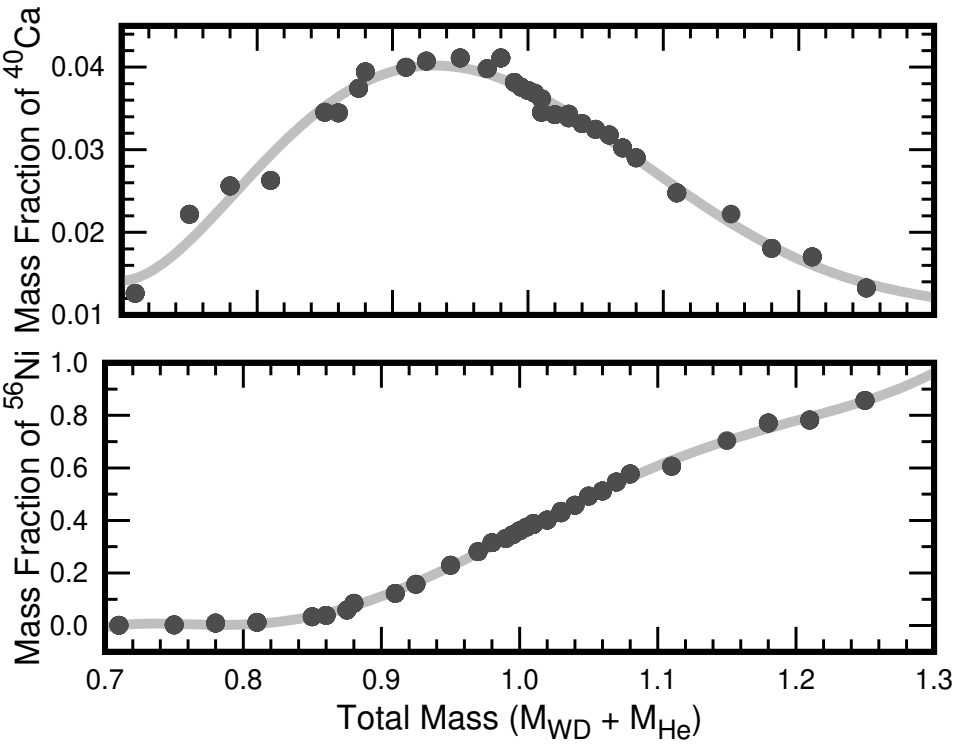

Figure 6.1: Mass fractions of ^{40}Ca (top) and ^{56}Ni (bottom) summed from the modeled ejecta masses. Nebular spectra appear Ca-rich (cool primarily through [Ca II]) for mass fractions as high as X_{Ca} =0.04 and as low as X_{Ca} =0.01. While the majority of the ejecta mass is produced during the burning of the WD, a small amount of both ^{56}Ni and ^{40}Ca are produced by the helium shell. As a result the grey line depicts the general trend dominated by the core yields while individual models scatter above and below this line due to small deviations arising from the synthesis of small amounts of material produced in the shells.

complete. So, for very low mass progenitors much of the final ejecta is composed of elements lighter than calcium. As we increase the mass (and density) of the progenitor more and more of those lighter elements continue to burn into calcium. However, we eventually reach a point where the progenitors are heavy (and dense) enough that the ejecta burns into calcium, then keeps burning into heavier elements.

Whether or not a model would be categorized as a Ca-rich SN if observed during the nebular phase is dependent on two parameters: the amount of ^{40}Ca in the ejecta, and the amount of Fe group elements. It is not sufficient to have Ca in the ejecta; in fact, it is more important that the ejecta lack Fe group elements through which to cool.

Our understanding of Ca-rich transients is limited by the small number of observed events; however, current constraints made by fitting light curve shapes place ejecta mass estimates of order $\sim$0.5 $M_{\odot}$ (Kasliwal et al. 2012). The question remains: how rich in Ca

do these events need to be? The prototype event, SN 2005E, was originally modeled with an ejecta mass of 0.3 $M_\odot$ and 0.14 $M_\odot$ of ^{40}Ca in the ejecta (X_{Ca}=0.47) (Perets et al. 2010). More recently, Dessart & Hillier (2015) modeled a helium shell detonation model (one where the shell burning does not cause an ignition of the underlying WD) and showed that the nebular spectra appeared Ca-rich with an ejecta mass of 0.2 $M_\odot$ having produced 0.03 $M_\odot$ Ca (X_{Ca}=0.15); moreover, the nebular spectrum continued to cool through [Ca II] when that mass fraction was halved.

While the models focused on by Polin et al. (2019b) are not a good match to Ca-rich transients in the photospheric phase, they provide important insight into the puzzle of the origin of such events. When we examine our double detonation models which would be characterized as Ca-rich (those with a total mass less than $\sim$0.9 $M_\odot$), we see spectra that primarily cool through [Ca II] emission with a significantly smaller mass of Ca required. Figure 6.1 shows that as little as 0.02 $M_\odot$ ^{40}Ca (or 0.01 by mass fraction) can produce a Ca-rich event. This is an order of magnitude less than the percentages provided in the previous literature.

Very low mass ($\lesssim$ 0.7 $M_\odot$) double detonation progenitors were not explored by Polin et al. (2019b), so we cannot rule out the low mass part of this parameter space as a possible progenitor for some Ca-rich gap transients. This region of double detonations is worth exploring. However, NLTE radiative transport calculations would be required throughout the photospheric phase to determine if features such as He absorption seen in many of the Ca-rich population can be explained by this model. We leave it as a future exercise to examine if very low mass double detonations (should they disrupt their underlying CO WD) can act as potential progenitors for these Ca-rich transients.

Our study gives important insight into the progenitors of Ca-rich transients, as we show that very little Ca is needed in the SN ejecta to produce a nebular spectrum that cools predominantly through the forbidden [Ca II] emission line. We predict that future events like SN 2018byg could be classified as Ca-rich in the nebular phase, but we caution the use of this diagnostic to group SNe as their photospheric spectra can be wildly disparate.

6.2 SN 2016hnk

The content of this section is drawn from Jacobson-Galan et al. (2019), with permission from the co-authors.

In this section we discuss the observations, analysis, and modeling of the peculiar thermonuclear transient SN 2016hnk. Upon discovery, this object was originally classified as a SN Ia with photometric and spectroscopic similarities to both SN 1991bg and the Ca-rich transient PTF09dav. Sell et al. (2018) identified the object as a candidate Ca-rich gap transient.

We present observations and modeling of SN 2016hnk, a Ca-rich SN that is consistent with being the result of a He-shell double-detonation explosion of a CO white dwarf. We

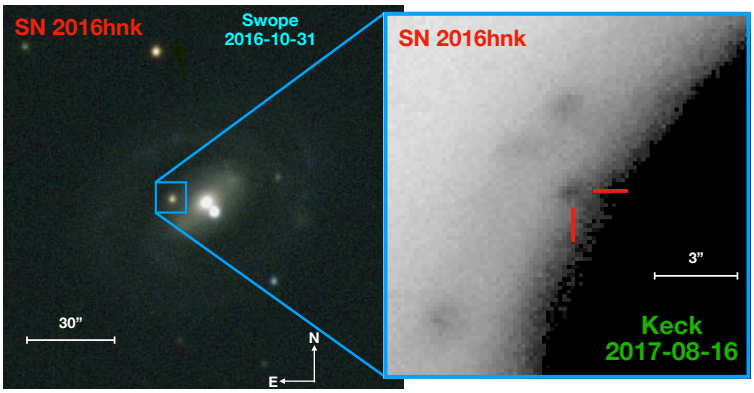

Figure 6.2: *Left:* RGB false-color image of SN 2016hnk taken by the Swope telescope two days after B-band maximum. RGB image generated using r-, V-, & B-bands. *Right:* I-band Keck LRIS image at +291d. Source marked in red. The location of SN 2016hnk serves to distinguish it from most Ca-rich transients which mostly occur significantly offset from their hosts. Figure taken from Jacobson-Galan et al. (2019) with permission of the co-authors.

find that SN 2016hnk is intrinsically red relative to typical thermonuclear SNe and has a relatively low peak luminosity ($M_B = -15.4$ mag), setting it apart from low-luminosity Type Ia supernovae (SNe Ia). SN 2016hnk has a fast-rising light curve that is consistent with other Ca-rich transients ($t_r = 15$ d). The photospheric spectra show strong, high-velocity, Ca II absorption and significant line blanketing at $\lambda < 5000$ Å, making it distinct from typical (SN 2005E-like) Ca-rich SNe. SN 2016hnk is remarkably similar to SN 2018byg, which was modeled as a He-shell double-detonation explosion. We demonstrate that the spectra and light curves of SN 2016hnk are well modeled by the detonation of a 0.02 $M_\odot$ helium shell on the surface of a 0.85 $M_\odot$ CO white dwarf. This analysis highlights the second observed case of a He-shell double-detonation and suggests a specific thermonuclear explosion that is physically distinct from the typical Ca-rich SNe that are defined simply by their low luminosities and strong [Ca II] emission.

6.2.1 Observational Properties

We plot the photometry of SN 2016hnk in the right panel of Figure 6.3. Photometry for this subluminous event begins around the time of peak brightness and data are available in five different color bands. The most peculiar aspect about SN 2016hnk photometrically is the very slow decline in the B- and g-bands beginning around 15 days after r-band maximum.

The spectral sequence of SN 2016hnk is shown in the left panel of Figure 6.3. The earliest spectra are taken around peak brightness, where they exhibit strong absorption features from intermediate mass elements (IMEs) including Si II, S II, O I, a broad Ca II absorption feature, and line blanketed features in the blue part of the spectrum. All of these are reminiscent of SN 2018byg and the predictions for double detonations triggered by thick He shell ignitions.

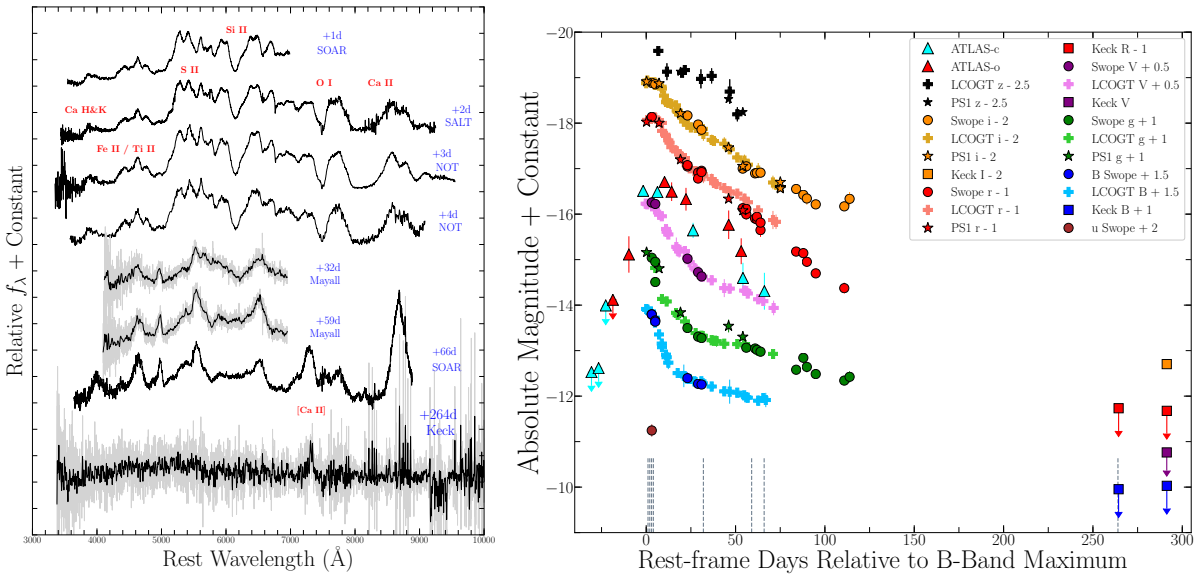

Figure 6.3: *Left:* Spectral observations of SN 2016hnk with phases (blue) marked with respect to B-band maximum. Raw spectra are shown in gray and spectra smoothed with Gaussian filters in black lines. *Right:* Optical light curves of SN 2016hnk with respect to B-band maximum. The epochs of our spectral observations are marked by grey dashed lines. Figure taken from Jacobson-Galan et al. (2019) with permission of the co-authors.

Spectroscopic follow up observations continue into the nebular phase where the only emission feature at +264 days is that of the forbidden [Ca II] cooling line at ∼7200 Å, also a feature predicted for double detonations in this subluminous regime.

Figure 6.4 shows SN 2016hnk compared with SN 2018byg. When note similarities in both the photometric and the spectrosopic evolution, indicating the need to examine this event as having originated from a double detonation.

6.2.2 Explosion Models

The observed spectroscopic and photometric properties of SN 2016hnk suggest a different explosion scenario than typical SNe Ia. The prominence of high velocity (∼18,000 km/s) intermediate mass elements such as Ca II in SN 2016hnk indicates a potential helium detonation (Fink et al. 2010; Kromer et al. 2010). Such a scenario can produce a large amount of Fe-group elements in the outer regions of the SN ejecta that causes significant line blanketing near maximum light, in addition to a fast rising light curve (Shen et al. 2018a; Polin et al. 2019b). These expected signatures of helium shell detonation on a CO WD are consistent with the observed spectral features and light curve evolution of SN 2016hnk.

We model the light curve and spectra of SN 2016hnk using the grid of different helium shell detonation scenarios derived from Polin et al. (2019b). Our simulations track the double

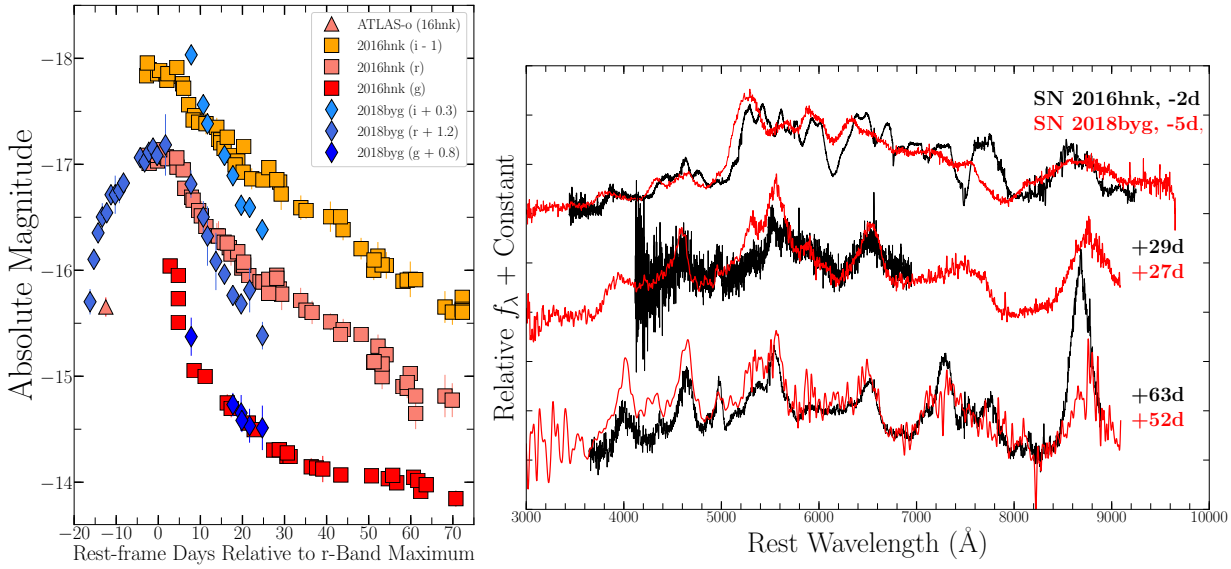

Figure 6.4: *Left:* Light curve comparison of r- and g-band photometry for each object relative to r-band maximum. SN 2018byg has been shifted in magnitude to match SN 2016hnk. *Right:* Spectral comparison of SNe 2016hnk and SN 2018byg at multiple epochs. Phases relative to r-band maximum. The spectroscopic evolution of SN 2016hnk is remarkably similar to that of SN 2018byg which we think to be of double detonation origin. Figure taken from Jacobson-Galan et al. (2019) with permission of the co-authors.

detonation of a 50% carbon + 50% oxygen, $\sim 0.8\ M_\odot$ WD with $\sim 0.03\ M_\odot$ of helium on the surface.

In Figure 6.5, we compare the helium shell model light curves to our V, g, r, i band photometry. We find that helium shell detonation with a total mass of $0.87\ M_\odot$ (WD + helium shell) can reproduce the peak absolute magnitudes in all bands as well as the early-time light curve decline. Additional constraints cannot be placed on the very early-time light curve evolution owing to the limited pre-maximum data for SN 2016hnk. However, we do include ATLAS o- and c-band data for comparison with the r/i- and V-bands, respectively. The pre-maximum o-band data point in Figure 6.5 appears to be most consistent with the best fitting, non-mixed $0.85{+}0.02\ M_\odot$ model (green line), but it is also within the phase uncertainties of the $0.85{+}0.02\ M_\odot$ mixed N100 model (dotted violet-red line).

The divergence between the models and SN 2016hnk at ∼25 days post explosion may be attributed to a variety of factors within the explosion. Firstly, for a similar model, the LTE assumptions made while performing the radiative transport calculations may be less representative of the conditions within the ejecta of SN 2016hnk than SN 2018byg, which is modeled to have a higher total mass than SN 2016hnk ($0.91\ M_\odot$ vs. $0.82\ M_\odot$), and may take longer to become optically thin. An LTE condition is not applicable once the ejecta begins to become optically thin, which typically occurs ∼30 days after explosion for sub-Chandrasekhar

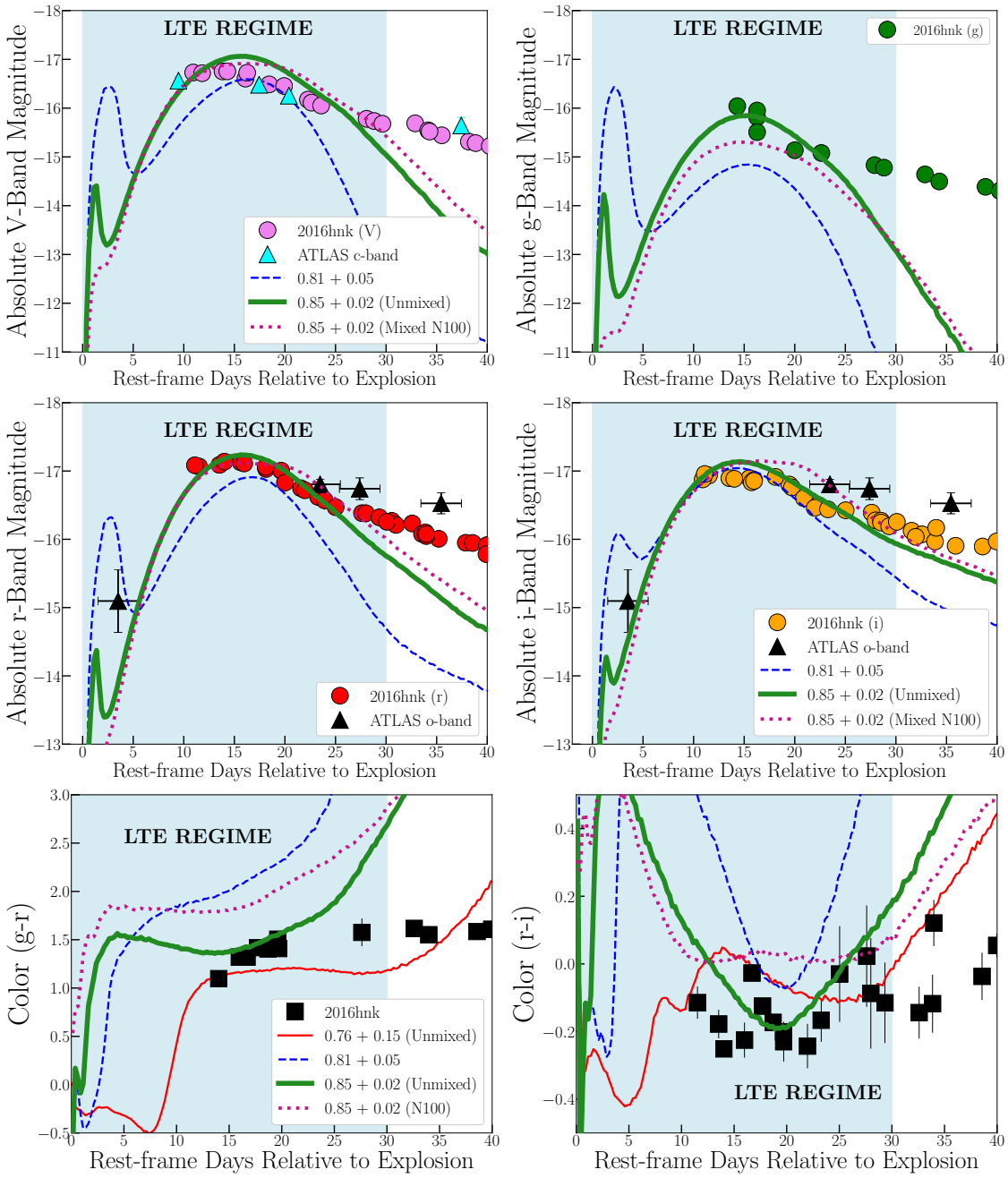

Figure 6.5: Light curve comparison to double detonation helium shell models presented by Polin et al. (2019b). The LTE regime (i.e., where the models are most reliable) is shown by shaded light blue region. Best fitting 0.85+0.02 model has no mixing of ejecta and is shown in forest green. Same model but with mixing (N100) shown in violet-red. Left to right: *V*, *g*, *r*, *i* band photometry. *Bottom:* *g*-*r* and *r*-*i* color comparison to helium shell models. Figure taken from Jacobson-Galan et al. (2019) with permission of the co-authors.

mass ejecta (light blue shaded region in Figure 6.5). A more detailed treatment of non-LTE (NLTE) conditions could explain the slower light curve decline in SN 2016hnk. Furthermore, our 1D helium shell model does not account for additional physics such as asymmetries or external emission components that could have influenced the increased light curve flux relative to the models. Nonetheless, while the model is an approximation of the SN explosion physics, it provides a reasonable match to the observables with only two free parameters (the mass of the helium shell and the mass of the underlying WD).

In Figure 6.5(c) we compare g-r and r-i colors of SN 2016hnk to various helium shell models from Polin et al. (2019b). Overall both mixed and unmixed models have bluer colors than those observed in SN 2016hnk. However, in the LTE regime the models are consistent to within 0.3 mag of SN 2016hnk's g-r and r-i color evolution. We cannot constrain the helium shell mass further given the lack of pre-maximum color information.

As shown in the top panel of Figure 6.6, the photospheric spectra of SN 2016hnk are best reproduced by a detonation model involving a 0.85 $M_\odot$ WD and 0.02 $M_\odot$ helium shell. This model has a total synthesized ^{56}Ni yield of 0.045 $M_\odot$. For reference, we compare SN 2016hnk to another model spectra from Polin et al. (2019b) with the same total mass, but a larger shell mass in Figures 6.6. Our best fit model reproduces SN 2016hnk's spectral signatures at time of peak brightness, including the line blanketed blue region, and the strength and velocity of the Ca II absorption feature around 8,000 Å. We do note that the model struggles to reproduce the strength of the O I absorption feature around 7,600 Å, however as discussed in Section 3.1.1, this is a known weakness that we expect to occur owing to the LTE assumption made in the radiative transport calculations (Baron et al. 1996; Nugent 1997).

We track the evolution of the best-fitting models with respect to observations in a spectral time-series presented in Figure 6.7(a). In Figure 6.7(b) we present Si II and Ca II velocities for SNe 2005ke, 2016hnk, and 2018byg with respect to the same line velocities from the best-fitting helium shell model. In both figures we demonstrate a time-dependent consistency between the complete spectral profile, as well as individual ion velocities, observed in SN 2016hnk and the 0.85 $M_\odot$ WD plus 0.02 $M_\odot$ helium shell model.

Using the nebular companion to `Sedona`, `SedoNeb` (Botyánszki et al. 2018), we are able to examine our best-fitting 0.85 + 0.02 $M_\odot$ model in the nebular phase following the methods outlined by Polin et al. (2019a) (discussed in Chapter 4), which investigates the nebular features of double detonations and shows that low mass scenarios would appear Ca-rich in the nebular phase. These methods require the SN ejecta to be fully optically thin in the desired wavelengths in order to produce a nebular spectrum. In this way we are able to examine the observational signatures of our model in the nebular phase (beginning ∼150 days after explosion). The resulting spectrum is shown in the bottom panel of Figure 6.6 as a green line. This model is consistent with the nebular spectrum of SN 2016hnk at +264 day after time of peak brightness, with [Ca II] emission being the dominant feature in both the simulation and observation.

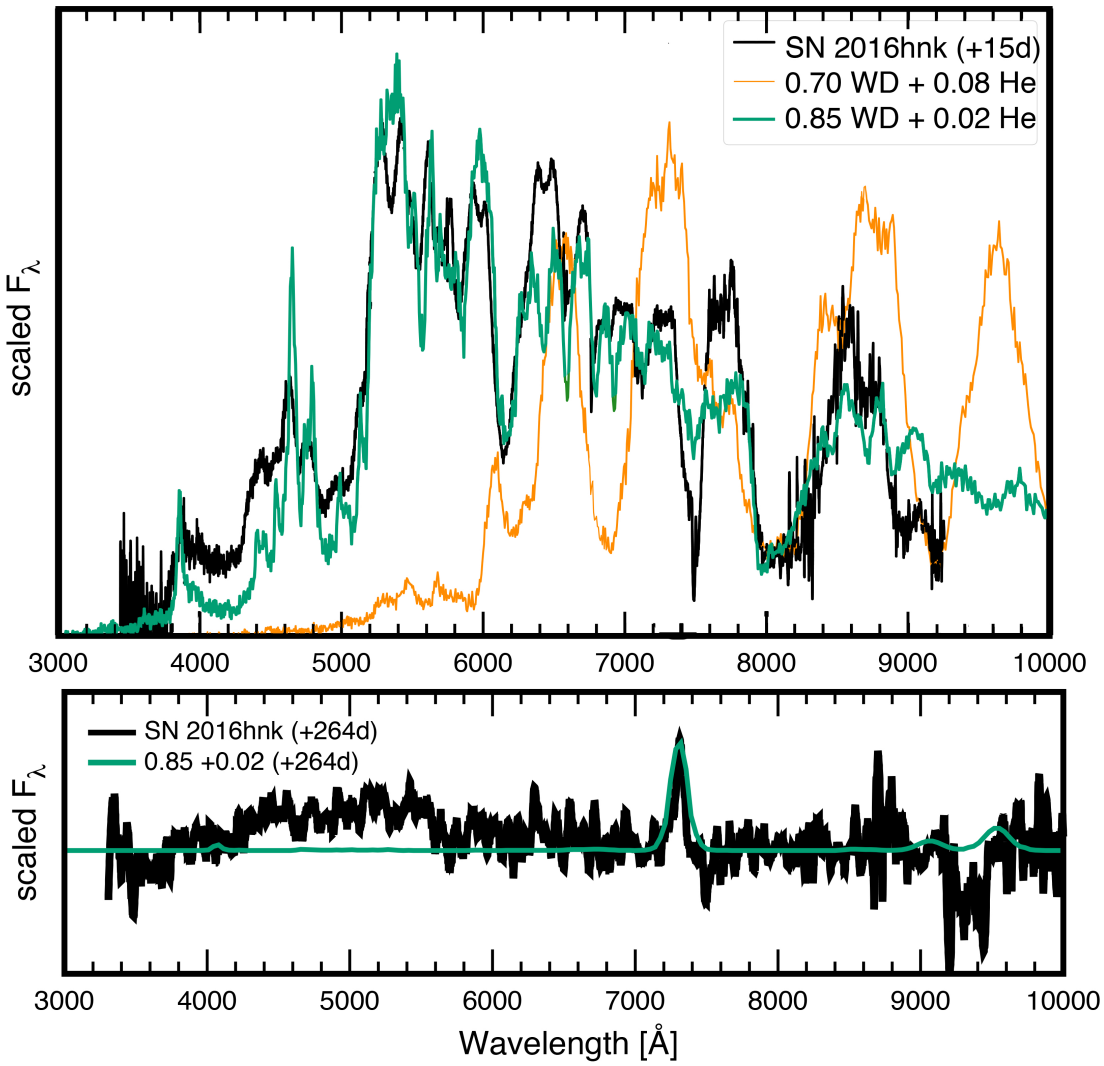

Figure 6.6: *Top:* Photospheric model comparison of SN 2016hnk (black) and double detonation models from Polin et al. (2019b). The best-fitting, 0.85+0.02 model is shown in green, and a model of a similar total mass but higher shell mass is shown in yellow to rule out helium shells larger than we present. Phases presented are with respect to explosion. *Bottom:* Nebular comparison of SN 2016hnk and best fitting 0.85+0.02 helium shell nebular model from Polin et al. (2019a). Phases are also with respect to estimated explosion date. Our 0.85+0.02 model matches the spectroscopic signatures of SN 2016hnk at time of peak brightness as well as in the nebular phase. Data taken from Jacobson-Galan et al. (2019).

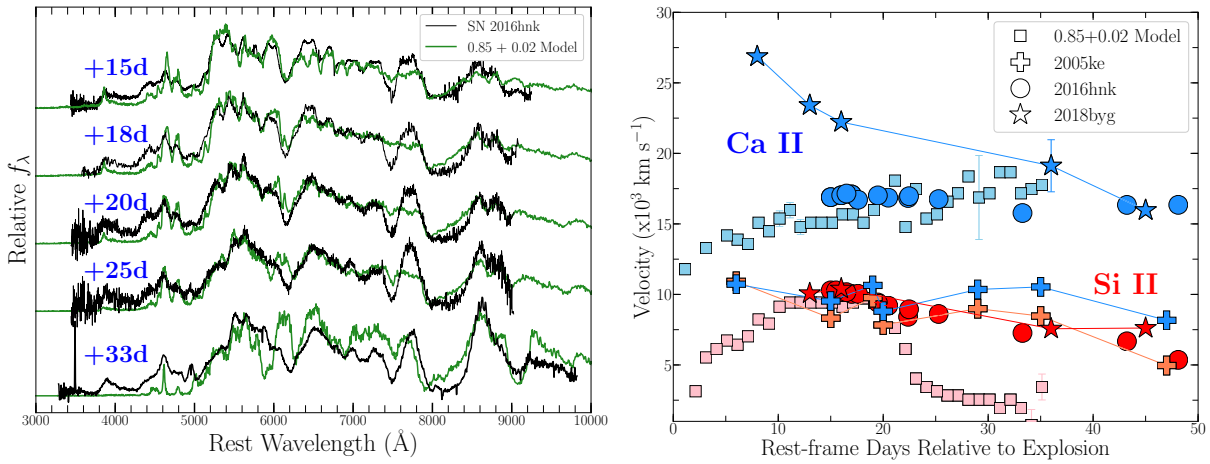

Figure 6.7: (a) Spectral time-series of SN 2016hnk (black) and the best-fitting helium shell detonation model (green) with phases relative to explosion. (b) The evolution of Ca II and Si II velocities, calculated from fitted absorption minima, are presented for SN 2005ke (plus signs), SN 2016hnk (circles), and SN 2018byg (stars) with respect to those derived from best-fitting model spectra (squares). Figure taken from Jacobson-Galan et al. (2019) with permission of the co-authors.

6.2.3 Discussion

The photometric and spectroscopic evolution of SN 2016hnk is remarkably similar to that of SN 2018byg. Both events are modeled successfully using the suite of simulations produced by Polin et al. (2019b). We find SN 2016hnk to be consistent with the detonation of a 0.85 $M_\odot$ WD with a 0.02 $M_\odot$ helium shell, a lower ejecta mass event than SN 2018byg, but trigger by a substantially less massive He shell. This constitutes the second observed event consistent with those of a double detonation triggered by a thick helium shell.

This is the first potential thick helium shell double detonation that we are able to compare to the models in both epochs as the nebular spectrum of SN 2018byg was unable to be obtained. We find in SN 2016hnk the confirmation that low mass double detonations should appear Ca-rich in the nebular phase, lending credence to our insights about the composition of these Ca-rich events.

Chapter 7

Double Detonations within the Population of Observed Type Ia Supernovae

The earlier discussion of observations in this thesis focused on the known thick helium shell double detonations; however, the thin helium shell double detonations can also still occur, and may be hiding amongst the observed population of SNe Type Ia. Here we discuss the impact our understanding of double detonation progenitors has had on the process of observing Type Ia SNe.

The promise of distinctive early features of double detonations has encouraged the ongoing trend of attempting to discover SNe as early as possible. We begin by discussing the search for, and populations of, SNe Type Ia with early flux excesses, as well as alternate possible progenitors for such features. We then discuss the results of ZTF's infant SN Ia program and its implications for the rates of double detonations within the population of observed SNe Type Ia.

7.1 Early Flux Excesses in Type Ia Supernovae

Current technological advancements have improved our ability to discover SNe earlier, and with a higher temporal cadence than ever before. This has led to the discovery of a few Type Ia SNe, SN 2017cbv (Hosseinzadeh et al. 2017) and SN 2018oh (Shappee et al. 2019; Dimitriadis et al. 2019), which exhibit flux excess in the earliest observed times. While this is a signature discussed in this thesis for thick helium shell double detonations, there are a number of other possibilities for the source of these early flux excesses.

Alternative methods of producing early flux excesses include, and are likely not limited to, interaction between the SN ejecta and a binary companion (Kasen 2010), interaction between the SN ejecta and circumstellar material (Dessart et al. 2014; Piro & Morozova 2016), shock cooling following shock breakout (Piro et al. 2010; Rabinak & Waxman 2011),

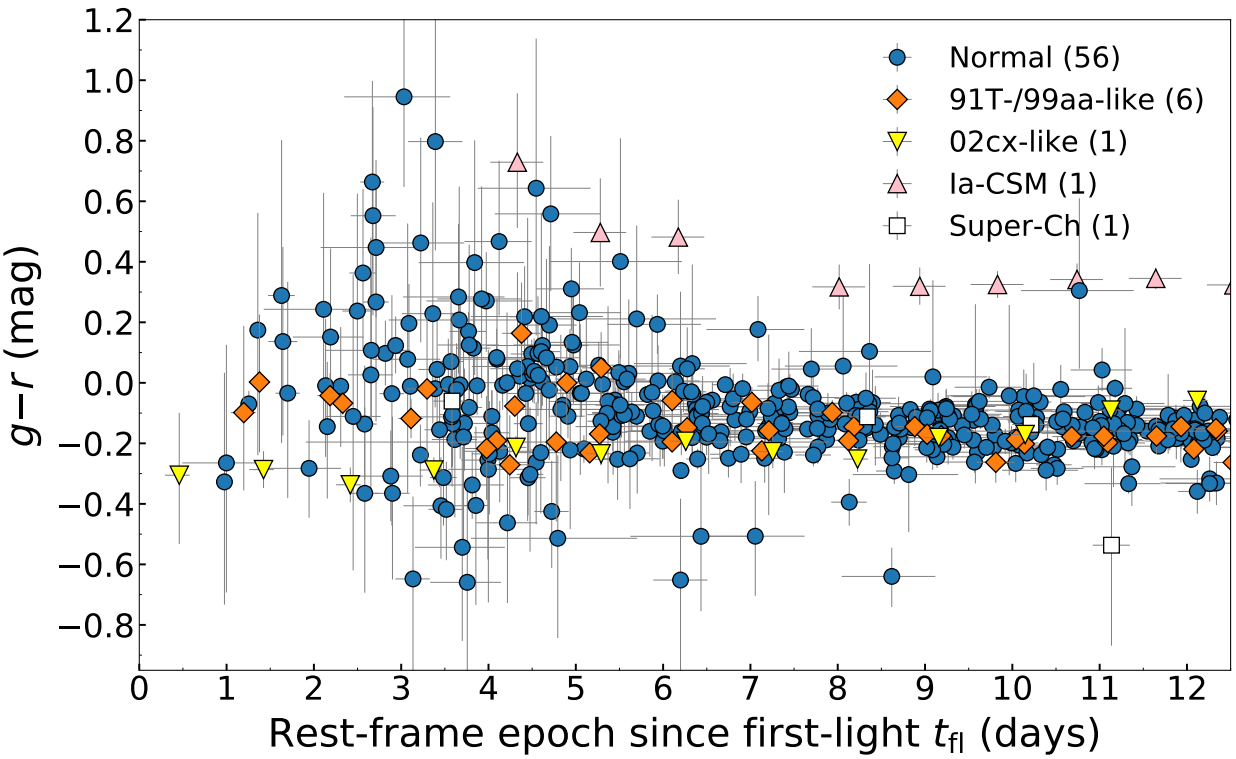

Figure 7.1: Evolution of $g-r$ colors for the 65 SNe Ia discovered by ZTF within 5 days from first-light t_{fl}. The sample includes 56 spectroscopically normal SNe Ia (blue circles), six overluminous 91T-/99aa-like SNe Ia (orange diamonds), one "02cx-like" SN (yellow triangles down), one "Ia-CSM" SN (pink triangle up), and one "super-Chandrasekhar" SN (white squares). Colors are corrected for reddening (both Milky Way and host galaxy) and K-correction. Figure taken from Bulla et al. (2020) with permission of the co-authors.

and clumps of ^{56}Ni in the outer SN ejecta (Shappee et al. 2019; Dimitriadis et al. 2019). The distinguishing factor between all of these flux excesses lies in their color evolution. The red to blue to red color evolution predicted by Polin et al. (2019b) and discussed in Chapter 3 is so far unique to double detonation explosions, and we therefore express the need not just for early observations of Type Ia SNe, but for early photometry taken in multiple bands. This happens to be precisely the goal of ZTF's infant SN Ia program.

7.2 Early Type Ia SNe Discovered by ZTF

Here we discuss the ZTF infant SN Ia program and its implications for the percentage of SNe Type Ia created via the double detonation explosion mechanism. Throughout 2018, ZTF performed an infant SN Ia program with the goal of detecting SNe Type Ia during the

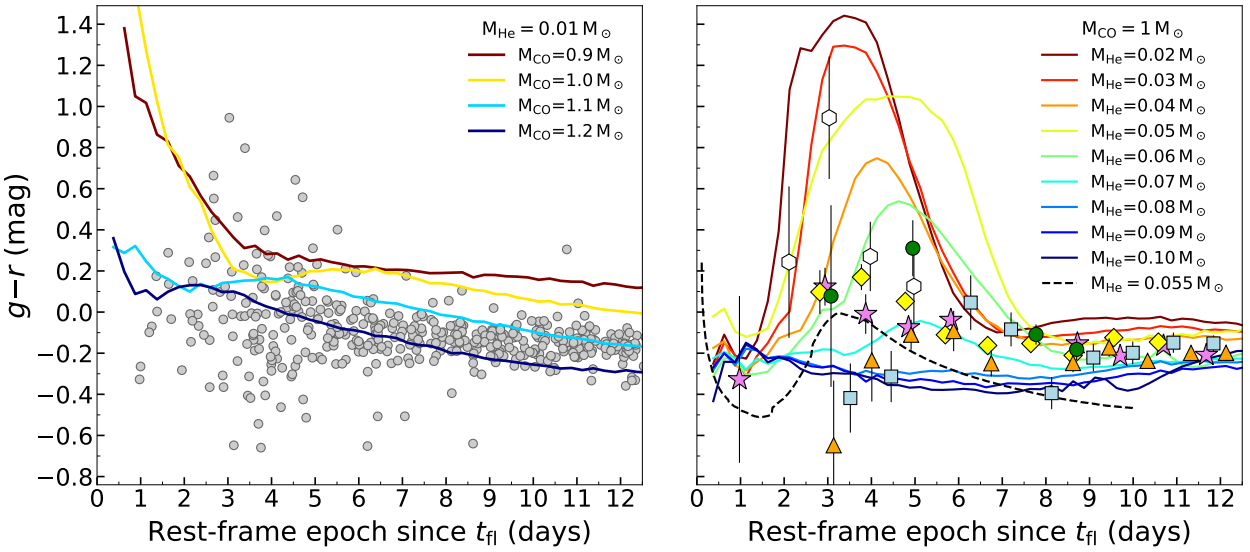

Figure 7.2: Comparison of our ZTF sample to "double-detonation" models. *Left panel*: the full ZTF sample (grey points) compared to models from Polin et al. (2019b) with fixed helium mass $M_{\rm He} = 0.01\,M_\odot$ and carbon-oxygen mass varying in the range $M_{CO} \in [0.9, 1.2]\,M_\odot$. *Right panel*: models with fixed carbon-oxygen mass $M_{CO} = 1.0\,M_\odot$ and varying helium masses. Models from Polin et al. (2019b, solid lines) have helium masses varying in the range $M_{He} \in [0.02, 0.10]\,M_\odot$ (from dark red to dark blue). The six events in the ZTF sample showing possible "red bumps," ZTF18abcflnz (SN 2018cuw), ZTF18abxxssh (SN 2018gvj), ZTF18abcrxoj (SN 2018cvw), ZTF18abgxvra (SN 2018efb), ZTF18abckujq (SN 2018cvf), and ZTF18aapqwyv (SN 2018bhc) are highlighted with yellow diamonds, light-blue squares, violet stars, orange triangles, green circles, and white hexagons, respectively. Figure taken from Bulla et al. (2020) with permission of the co-authors.

first few days after explosion, and following up these discoveries with multiple photometric bands to allow for color information. A total of 127 SNe Ia were discovered, 50 of which were detected at least 14 days prior to the time of maximum light (Yao et al. 2019). 65 of these events were discovered within 5 days of first light. This sample is approximately three times the size of any previously in literature. We show the early $g-r$ colors of these infant SNe Ia plotted in Figure 7.1.

We determine our time of first light, t_{fl}, by fitting the early time flux in both g (f_g), and r (f_r) bands as:

$$f_i(t) = C + H[t_{fl}]A_i(t - t_{fl})^{\alpha_i} \qquad i = g, r$$

Where A_i is a scale factor, H is the heaviside function, α_i is a power-law index, and t is time. For each SN in our sample Miller et al. (2020) provide two options for α_i. One assuming that $\alpha_i = \alpha_g = \alpha_r = 2$, implementing the popular t^2 rise of the fireball model

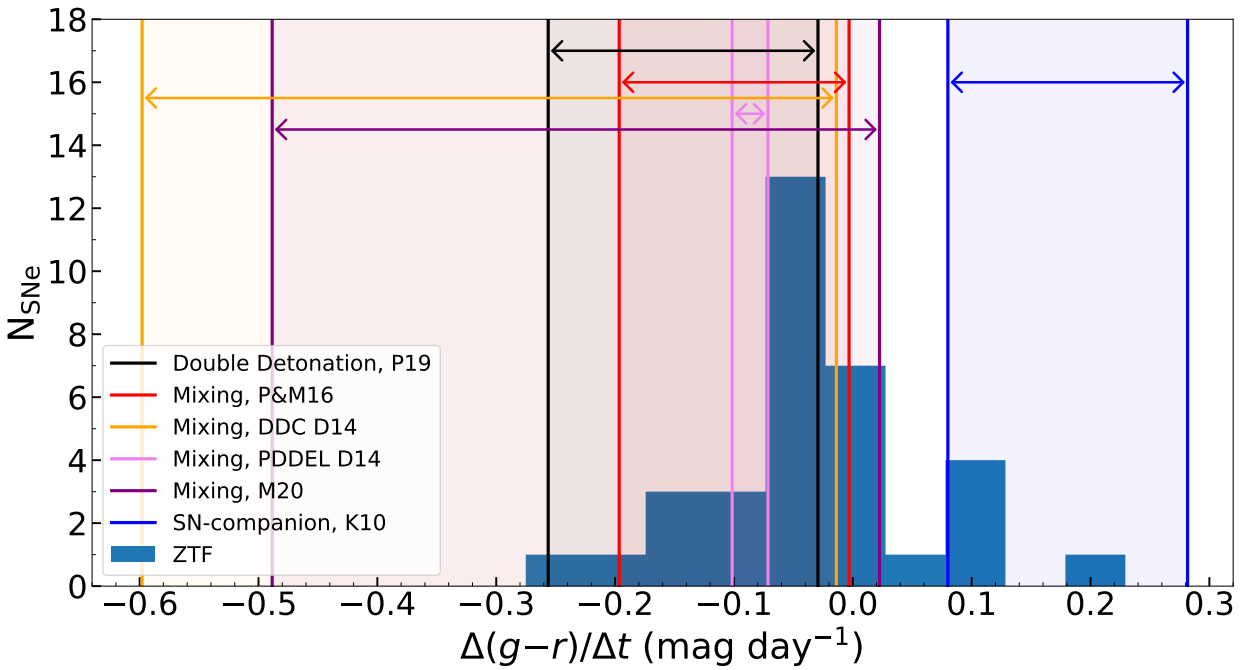

Figure 7.3: Comparison between observed and modelled slopes in the first 6 days since first light. The distribution refers to the linear slopes measured for 34 SNe Ia with at least three detections in the first 6 days. The range spanned by each series of models is shown with a shaded area and with a horizontal arrow. Mixing models are from Piro & Morozova (2016, red), Dessart et al. (2014, orange and violet), and Magee et al. (2020, purple), with an increasing amount of mixing from left to right (vertical lines). The range spanned by the four SN-companion interaction models from Kasen (2010) is shown in blue, while that from "double-detonation" models of Polin et al. (2019b) with $M_{\rm He} = 0.01\,M_\odot$ in black. Figure taken from Bulla et al. (2020) with permission of the co-authors.

(Riess et al. 1999), and one allowing $\alpha_g \neq \alpha_r$ where the power-law indicies are determined using a MCMC method. For each SN we choose the α_i's which provide the best fit to the early rise under the condition that $t_{fl,g} = t_{fl,r} = t_{fl}$. Although in reality $t_{fl,i}$ may actually differ slightly, we assume that the time of first light in both bands is the same because we expect that difference to be smaller than our temporal cadence.

In Bulla et al. (2020) we examine the early color evolution of these 65 events to determine the allowed progenitor mechanisms within this sample. Figure 7.2 shows the observed population from ZTF compared with our double detonation models. We find a total of six events that show the early red bump associated with thick helium shell explosions, shown in the right panel of Figure 7.2 compared with the double detonation models of a 1.0 $M_\odot$ WD with varying He shell mass plotted as colored lines. All six of these events display $g-r$ colors that are relatively blue at the time of detection, evolve to redder colors, and reach a peak

3-6 days after the time of first light before turning over to bluer colors. Additionally, one of these events, ZTF18abxxssh (SN 2018gvj), is associated with a strong early flux excess in its light curve (Yao et al. 2019), giving another point in favor of this event originating from the double detonation mechanism. The detection in six out of 65 SNe suggests a "red bump" might occur in ∼9% of the cases; however, this only constitutes the thick helium shell explosions.

Thin helium shell explosions produce far less ash in the outer ejecta layers and thus the reddening of the later times is less significant. They also produce less radioactive material for the helium shells and thus start off cooler. The result is the very rapid red to blue transition plotted in the left panel of Figure 7.2, which shows the double detonation models from Polin et al. (2019b) with 0.01 $M_{\odot}$ He shells plotted as colored lines. Figure 7.2 depicts the number of events allowed with each progenitor model discussed in Section 7.1. We find that the double detonation models can explain the range in slopes of the early color evolution for ∼60% of the observed events.

7.3 The Potential Lack of Carbon Features in Double Detonation Explosions

The content of this chapter is drawn from Polin et al. (2019b), with permission from the co-authors.

Another signature of a double detonation progenitor may be the lack of a carbon absorption feature in the SN spectra. Our 1D double detonation models are very efficient at carbon burning. The amount of unburnt carbon remaining in the ejecta is quite minimal, with only 0.001 $M_{\odot}$ in the SN 1991bg-like events dropping to 10^{-5} $M_{\odot}$ or less for the more normal SNe Ia. The efficiency of carbon burning is a characteristic of the sub-Chandrasekhar double detonation models, though more work will have to be done with multi-dimensional simulations to verify this property. However, this may not be a purely a consequence of our 1D methods. Examining several 1D Chandrasekhar mass models shows that the amount of unburnt carbon can be quite substantial. The pure deflagration model W7 of Nomoto et al. (1984) and the pulsating delayed detonation models seen in Hoeflich et al. (1995) typically have ∼0.03 $M_{\odot}$ of carbon left over after explosion.

Observationally there may be evidence for this as well. Maguire et al. (2014) note that carbon spectral features are not ubiquitous in well observed SNe Ia, and that ∼40% show no hint of C II features in their spectra when observed at times earlier than −10 days before peak brightness. What is interesting here is that none of the high-velocity SNe Ia in their sample show signs of carbon in the spectra. Furthermore, Parrent et al. (2011) show that most of the objects in their sample that exhibit the C II 6580 Å absorption features are of the low-velocity gradient subtype. Thomas et al. (2011) argue that the lack of carbon in high velocity SNe Ia might be due to to line blending effects. However, our models would

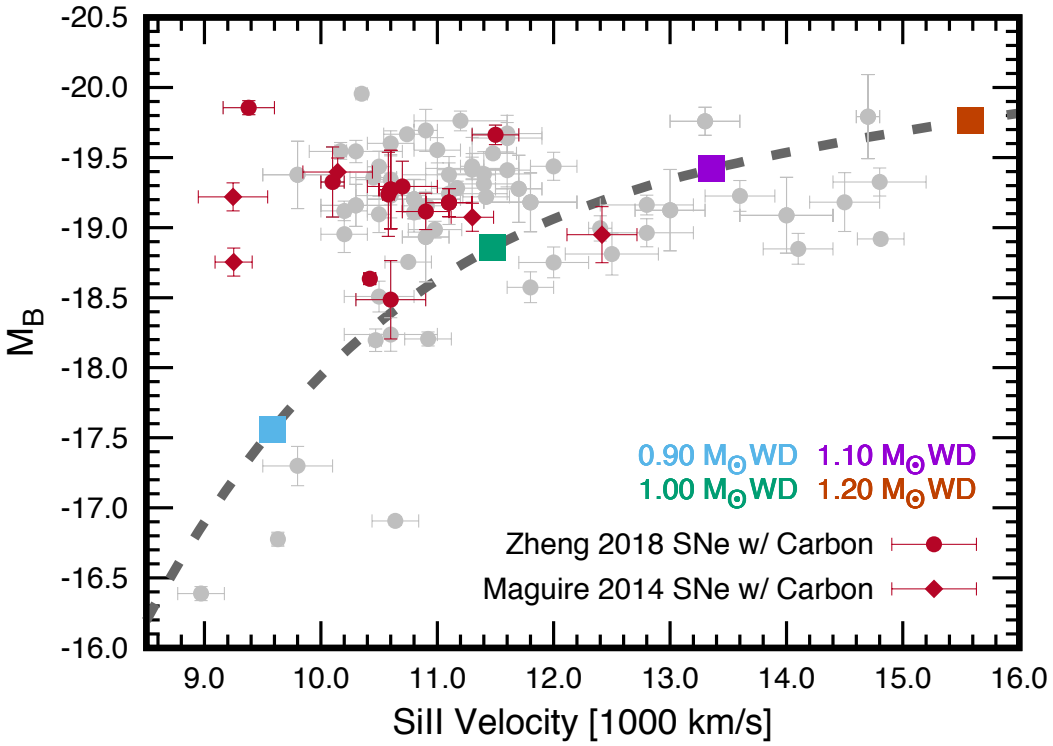

Figure 7.4: The Si II velocity - luminosity relationship introduced by Polin et al. (2019b). The circles represent SNe Ia from Zheng et al. (2018), and the squares are the thing helium shell models from Polin et al. (2019b). The grey data are SNe Ia that show no signs of carbon absorption and the red data are those that exhibit carbon absorption features in the early rise. We also include the additional SNe Ia from Maguire et al. (2014) that exhibit carbon absorption features. We note that the SNe Ia that exhibit carbon absorption predominantly lie in the cluster not modeled by double detonations.

suggest that these may be sub-Chandrasekhar mass double detonation explosions and that the lack of a C II feature is due to an absence of carbon in their atmospheres. What is further intriguing is that both Maguire et al. (2014) and Thomas et al. (2011) note that those SNe Ia with carbon features are grouped tightly in light curve shape space and have colors that are bluer than most SNe Ia. Our double detonation models exhibit neither of these characteristics.

To explore this this possibility further we take the population of SNe Ia from Zheng et al. (2018) and determine which SNe show carbon absorption features during the early rise. We examine these SNe on the Si II velocity-luminosity relationship plot introduced by Polin et al. (2019b) in Figure 7.4. We also include those SNe Ia from Maguire et al. (2014) which exhibit carbon features by using the Si II velocity found in Maguire et al. (2014) and

the B-band magnitudes determined by Pan et al. (2014). We show that the SNe Ia which exhibit carbon absorption features (plotted in red) exist predominantly in the population not consistent with our double detonation models, lending further credence to this method of separating SNe Ia into two distinct progenitor channels.

This highly motivates future work where all of these properties are examined simultaneously in a statistically significant sample of well observed SNe Ia, and compared with multi-dimensional double detonation simulations.

Chapter 8

Future Directions and Progress on Multidimensional Modeling

Our published sub-Chandrasekhar WD explosion models have been created using 1D computational methods (Polin et al. 2019b). We are currently in the process of extending this work to multi-dimensional (multi-D) hydrodynamic models. While many groups have performed multi-D hydrodynamic simulations of double detonation explosions (Fink et al. 2010; Moll & Woosley 2013; Townsley et al. 2019; Leung & Nomoto 2020), few have examined full multi-D radiative transport calculations to examine the dependence of observational properties on viewing angle (Kromer et al. 2010). Furthermore, the literature has primarily been concerned with the thin helium shell double detonations, rather than the more rare thick helium shell events. Thus, this is an open landscape for investigation. Here we discuss the importance of multi-D simulations and what questions we hope to answer using 2- and 3-dimensional hydrodynamic simulations of double detonation explosions paired with multi-D radiative transport calculations.

8.1 Current Status of Multi-D Models

Figure 8.1 shows an example of our preliminary 2D simulations. This particular model is a 0.76 $M_\odot$ WD with 0.15 $M_\odot$ helium on its surface, the same values as those found for our 1D model fit for SN 2018byg (De et al. 2019). Figure 8.1(a) shows the setup of our system at the time of the initial helium ignition. The initial helium ignition is inserted on the pole at a height of roughly one third the radial thickness of the helium shell. This was the ignition location found in the 1D models to delineate between a traditional double detonation (where the core is ignited via shock convergence) and an edge-lit scenario (where the core starts burning at the interface between the core and the helium shell) (see Chapter 2 for more details on the conditions for edge-lit ignitions). Figure 8.1(b) shows the simulation after having evolved for 0.5 s. Here we see that helium shell burning has begun to progress around the WD and the beginnings of a shock front traveling into the core. After the helium

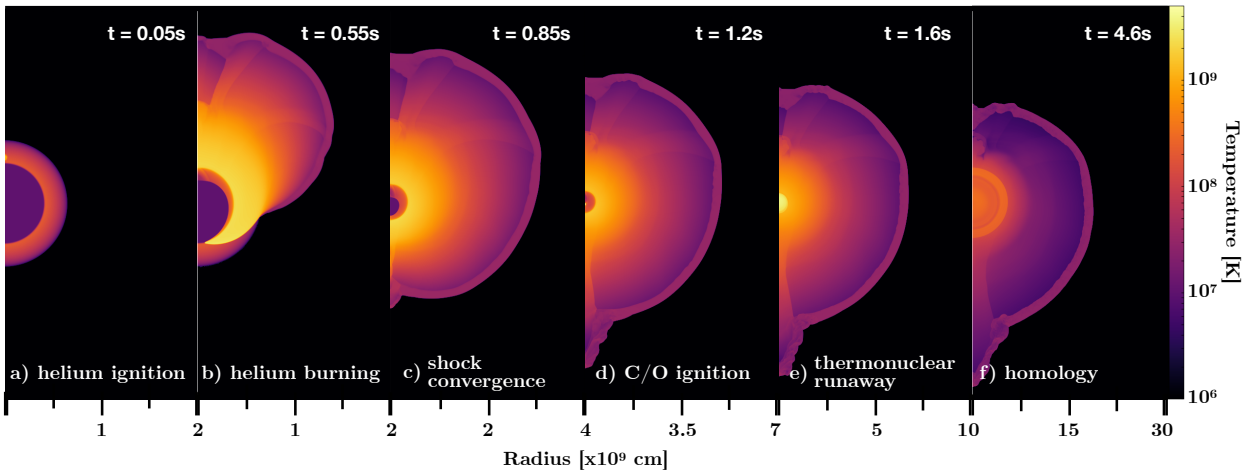

Figure 8.1: Preliminary example of our 2D hydrodynamic simulations of a double detonation explosion triggered by an ignition in a thick helium shell. We plot the temperature profile as the double detonation evolves over time.

shell burning is complete the helium ashes expand away from the WD. We show this in Figure 8.1(c) at which point the central shock front travels inwards towards the center of the WD. In Figure 8.1(d) the shock front converges, igniting the WD near the center of its core. Figure 8.1(e) shows the thermonuclear runaway of the WD. Here, the shock front created by the detonation of the CO WD is expanding outward into the helium shell ashes that have continued expanding as the WD burns. We note that while it took approximately 1.2 s for the system to evolve from the initial helium ignition to the second detonation of the WD core, it takes less than half a second for the entire WD to experience thermonuclear runaway. Several seconds later we show the ballistic ejecta freely expanding toward homology in Figure 8.1(f).

One of our main goals for this multi-D study is to compare the amount of mixing between the helium shell yields and WD products to the artificial mixing criterion created in our 1D models in order to fit the light curve of SN 2018byg. A mixing region of 0.2 $M_{\odot}$ was required to duplicate the characteristics of the early light curve rise for SN 2018byg. We had hoped Rayleigh-Taylor instabilities would cause some mixing in this regime when the thermonuclear shock front catches up with the slowly expanding helium shell ashes, however our 2D model shows no evidence for this phenomena.

We show the ejecta profiles of our 2D model and the equivalent 1D model in Figure 8.2, with the 2D profile representing a spherical average. While we do see some of the IMEs produced during thermonuclear runaway being smeared into the helium shell ashes, the magnitude of this mixing is significantly less than we employed in our 1D models of SN 2018byg. Furthermore, this smearing is likely caused by asymmetries over our spherical average rather than Rayleigh-Taylor mixing. The grey shaded region in the 2D plot denotes the mixing length of 0.2 $M_{\odot}$ required to fit the light curve of SN 2018byg when using our

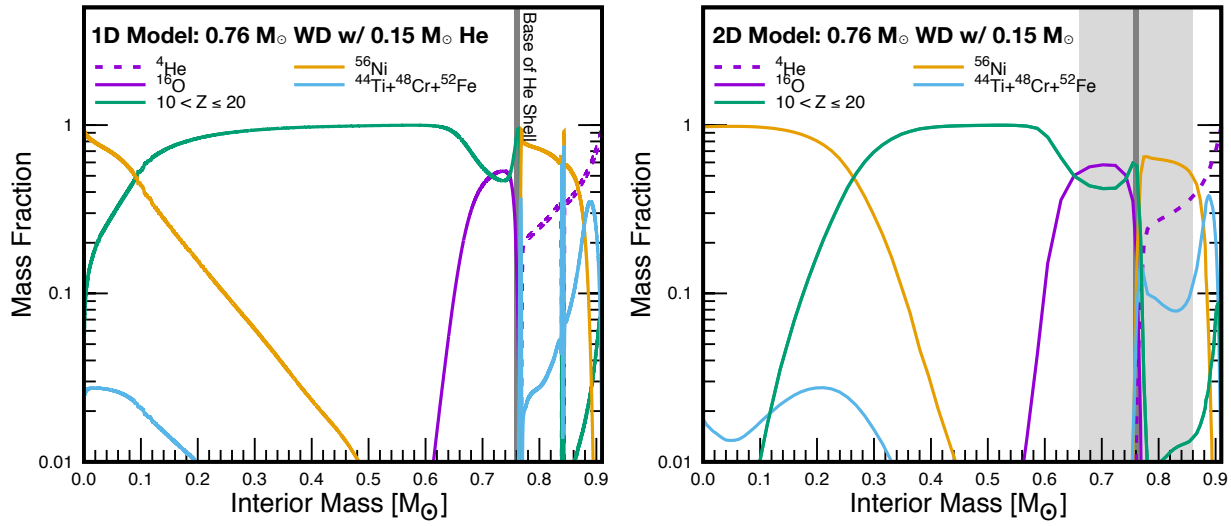

Figure 8.2: Ejecta profiles for the 0.76 $M_\odot$ WD with a 0.15 $M_\odot$ helium shell. The 1D model (left) undergoes less complete core burning and produces less ^{56}Ni than the (spherically averaged) 2D model (right). The grey region in the 2D plot shows the mixing length of 0.2 $M_\odot$ which was artificially implemented on the 1D model to fit SN 2018byg. Our 2D model does not produce enough mixing to account for this adjustment.

1D models. It seems that Rayleigh-Taylor instabilities alone cannot be responsible for the amount of mixing we need. Another source of mixing, not present in our 2D models is required, perhaps that caused by the ejecta interacting with the binary companion. We do note that while 2D simulations are likely adequate to gauge the general scope of this mixing phenomena, turbulence is inherently a 3D process so this exact quantity of mixing may change in future 3D simulations.

A striking difference in the ejecta profiles of the 1D and 2D models lies at the center of the core. The 2D model burns the core far more completely than the 1D model and produces a factor of 2 more ^{56}Ni in total, which will translate to a brighter event. Table 8.1 compares the summed nucleosynthetic yields for our 2D model and the equivalent 1D model. Although we do expect differences in the ^{56}Ni produced in the multi-D simulations, a factor of 2 is a significant change. We are in the regime where small changes in the density profile can lead to large changes in ^{56}Ni yields (see Figure 2.2). So, the difference between the 1D and 2D yields may be a result of small changes between the compression caused by the shock front when accounting for the 2D geometry. However, more work needs to be done before we can say for sure that these differences are physical, rather than numerical. For example, although we are comparing the 2D profile to a 1D simulation at the same resolution we have not yet completed resolution tests in 2D to ensure that this result is adequately converged to a solution that captures the shock physics in 2D.

We also note that while the 2D model contains a factor of 3.5 more ^{12}C than the 1D

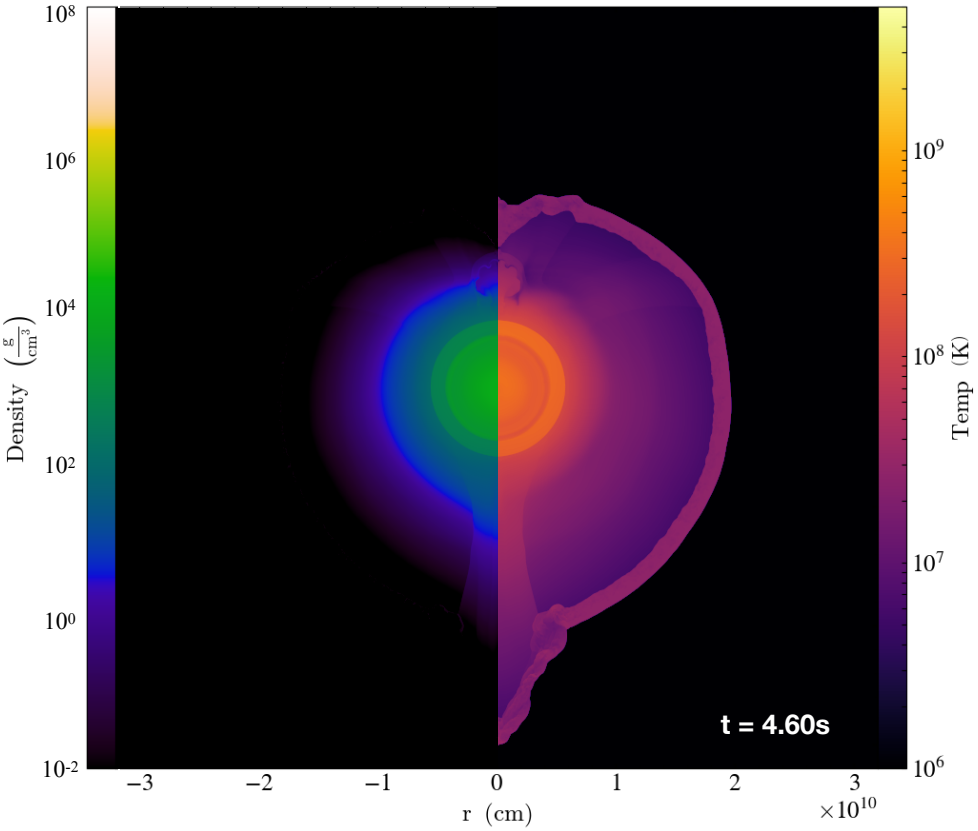

Figure 8.3: The final ejecta profile of a 0.76 $M_\odot$ WD with a 0.15 $M_\odot$ helium shell. The temperature profile is plotted on the right and density profile is shown on the left. Here the ejecta has reached it's final distribution as the velocity field has stopped evolving with time.

model, this is still an order of magnitude less than produced in Chandrasekhar mass models. We expect that the lack of a carbon absorption feature will remain a signature of a double detonation explosion as we complete our 2D study, however radiative transport calculations are required to determine how much ^{12}C can be present before the absorption feature becomes prominent in the early spectra.

8.2 Future Inquiries

While the amount of mixing that occurs between the WD and helium shell is a question we can answer with hydrodynamic modeling alone, there exist many questions that we can only answer when we combine our multi-D hydrodynamic simulations with full, multi-D radiative transport calculations.

For example, it is possible for the core ignition to occur off-center in the WD, as is the case for our preliminary model. How off center the ignition occurs will depend on

Table 8.1: 1D and 2D Model Comparison
for a 0.76 $M_\odot$ WD with a 0.15 $M_\odot$ Helium Shell

Element	1D Yields [$M_\odot$]	2D Yields [$M_\odot$]	Ratio (2D/1D)
^{4}He	5.28×10^{-2}	5.08×10^{-2}	0.96
^{12}C	4.27×10^{-4}	1.49×10^{-3}	3.49
^{16}O	4.38×10^{-2}	8.02×10^{-2}	1.83
^{20}Ne	1.92×10^{-6}	2.46×10^{-3}	1,280
^{24}Mg	9.07×10^{-4}	1.36×10^{-2}	15.0
^{28}Si	3.35×10^{-1}	2.40×10^{-1}	0.70
^{32}S	1.97×10^{-1}	1.20×10^{-1}	0.61
^{36}Ar	3.82×10^{-2}	2.33×10^{-2}	0.61
^{40}Ca	3.82×10^{-2}	2.45×10^{-2}	0.64
^{44}Ti	3.79×10^{-3}	5.26×10^{-3}	1.39
^{48}Cr	4.65×10^{-3}	5.96×10^{-3}	1.28
^{52}Fe	1.39×10^{-2}	1.73×10^{-2}	1.24
^{56}Ni	1.81×10^{-1}	3.10×10^{-1}	1.71

the WD mass, helium shell mass, and the relative burning-front propagation and shock convergence timescales, and may result in quite asymmetric explosions depending on the region of parameter space. Our preliminary model appears somewhat asymmetric in the temperature profile, and contains an artifact on the southern pole that is likely owing to the 2D axis-symmetric criterion. However, the density profile of the final ejecta configuration, shown in Figure 8.3, is far more symmetric, as there is not a lot of mass in the very outer most ejecta or along the pole. This prolateness may still lead to line of sight differences in the SN observables.

This is the case for the recent 2D simulation of the double detonation of a 1.0 $M_\odot$ WD with 0.02 $M_\odot$ helium on its surface performed by Townsley et al. (2019), where the WD ignition occurs at roughly half the radius of the WD. The resulting ejecta shows some mild asymmetries in the ^{56}Ni produced in the core, however the IMEs produced were more substantially asymmetric. In an approximation of multi-D radiation transport Townsley et al. (2019) model the observables of the ejecta profile by averaging the composition throughout a wedge of the ejecta and performing 1D radiative transport calculations based on a sphere of those averages. While the results were consistent with a normal SN Ia when viewed along the equator, the synthetic observables of this model varied drastically by viewing angle. The bolometric luminosity ranged from -19.5 mag when viewed along the pole opposite the helium ignition to -19.0 when viewed along the opposite pole. Both the velocities and strengths of the IME absorption features at the time of peak brightness vary by viewing angle as well, growing substantially stronger and faster (respectively) as the observer moves from the pole opposite the initial helium ignition around the WD until viewing along the line of sight of the opposite pole. While the radiative transport methods implemented in this study are adequate to examine qualitative trends in observables while varying viewing angle, it is likely that these effects will be less pronounced in reality. The process of averaging

along wedges assumes that from a given viewing angle the SN only emits photons from the composition along that line of sight. Radiative transfer, however, is inherently a multi-dimensional process, where photons originating in different parts of the medium will interact with this wedge in the process of emission before scattering in all directions, not just radially from the ejecta. This process tends to wash out line of sight viewing effects, whereas the wedge approximation will exacerbate them. Full multi-D radiative transport simulations are therefore still paramount in determining if double detonation asymmetries are compatible with SNe Type Ia observations.

While confirming that in multi-D hydrodynamic simulations the traditional double detonation mechanism still results in a central ignition, Moll & Woosley (2013) show that asymmetries may also occur in the helium shell ashes, particularly for thick helium shells. A single point ignition may result in more complete burning around the initial ignition, and multiple helium ignitions, for which we would require 3D simulations, can complicate the ejecta profiles further. The effect of these asymmetries on the characteristic early flux excess indicative of a thick helium shell double detonation is unknown. If it is the case that line of sight effects of asymmetries in the very outer ejecta are significant, then as we continue to discover more of these thick helium shell SNe, with better data throughout the early epochs, our 1D models will no longer be sufficient to probe the full physics exposed by these observations.

Lastly, while this work contains the first ever systematic investigation of double detonations in the nebular phase (Polin et al. 2019a), this picture is quite simplified by our 1D models. The nebular phase is a particularly powerful epoch from which to examine geometries of SNe because the entire ejecta has become optically thin. While different SN Ia models often start out looking similar and symmetric around the time of peak brightness, differences in internal structure can make themselves known at later times. With the completion of our multi-D study we plan to reexamine the nebular double detonations for both the regime responsible for Type Ia SNe as well as the low mass regime which we link to Ca-rich transients. In completing this last step, we hope to cement double detonation explosions as SN Ia progenitors, by showing our models' consistency with the observational signatures of Type Ia SNe throughout their evolution.

Bibliography

Almgren, A. S., Beckner, V. E., Bell, J. B., et al. 2010, ApJ, 715, 1221
Anupama, G. C., Sahu, D. K., & Jose, J. 2005, A&A, 429, 667
Arnett, W. D. 1969, Ap&SS, 5, 180
—. 1982, ApJ, 253, 785
Baron, E., Hauschildt, P. H., Nugent, P., & Branch, D. 1996, MNRAS, 283, 297
Bauer, E. B., Schwab, J., & Bildsten, L. 2017, ApJ, 845, 97
Bildsten, L., Shen, K. J., Weinberg, N. N., & Nelemans, G. 2007, ApJ, 662, L95
Blinnikov, S., Lundqvist, P., Bartunov, O., Nomoto, K., & Iwamoto, K. 2000, ApJ, 532, 1132
Blondin, S., Dessart, L., & Hillier, D. J. 2018, MNRAS, 474, 3931
Blondin, S., Matheson, T., Kirshner, R. P., et al. 2012, AJ, 143, 126
Botyánszki, J., & Kasen, D. 2017, ApJ, 845, 176
Botyánszki, J., Kasen, D., & Plewa, T. 2018, ApJ, 852, L6
Branch, D., Garnavich, P., Matheson, T., et al. 2003, AJ, 126, 1489
Brooks, J., Bildsten, L., Marchant, P., & Paxton, B. 2015, ApJ, 807, 74
Bulla, M., Miller, A. A., Yao, Y., et al. 2020, arXiv e-prints, arXiv:2001.00587
Cikota, A., Patat, F., Wang, L., et al. 2019, MNRAS, 2014
Cristiani, S., Cappellaro, E., Turatto, M., et al. 1992, A&A, 259, 63
De, K., Kasliwal, M. M., Polin, A., et al. 2019, ApJ, 873, L18
Dessart, L., Blondin, S., Hillier, D. J., & Khokhlov, A. 2014, MNRAS, 441, 532
Dessart, L., & Hillier, D. J. 2015, MNRAS, 447, 1370
Dimitriadis, G., Foley, R. J., Rest, A., et al. 2019, ApJ, 870, L1
Dong, S., Katz, B., Kushnir, D., & Prieto, J. L. 2015, MNRAS, 454, L61
Drout, M. R., Soderberg, A. M., Mazzali, P. A., et al. 2013, ApJ, 774, 58
Elias-Rosa, N., Benetti, S., Cappellaro, E., et al. 2006, MNRAS, 369, 1880
Filippenko, A. V., Chornock, R., Swift, B., et al. 2003, IAU Circ., 8159, 2
Filippenko, A. V., Richmond, M. W., Matheson, T., et al. 1992a, ApJ, 384, L15
Filippenko, A. V., Richmond, M. W., Branch, D., et al. 1992b, AJ, 104, 1543
Fink, M., Hillebrandt, W., & Röpke, F. K. 2007, A&A, 476, 1133
Fink, M., Röpke, F. K., Hillebrandt, W., et al. 2010, A&A, 514, A53
Fink, M., Kromer, M., Seitenzahl, I. R., et al. 2014, MNRAS, 438, 1762
Flörs, A., Spyromilio, J., Taubenberger, S., et al. 2019, arXiv e-prints, arXiv:1909.11055

Folatelli, G., Morrell, N., Phillips, M. M., et al. 2013, ApJ, 773, 53
Foley, R. J., & Kasen, D. 2011, ApJ, 729, 55
Foley, R. J., Narayan, G., Challis, P. J., et al. 2010, ApJ, 708, 1748
Foley, R. J., Challis, P. J., Chornock, R., et al. 2013, ApJ, 767, 57
Frohmaier, C., Sullivan, M., Maguire, K., & Nugent, P. 2018, ApJ, 858, 50
Ganeshalingam, M., Li, W., Filippenko, A. V., et al. 2010, ApJS, 190, 418
—. 2012, ApJ, 751, 142
García-Senz, D., Cabezón, R. M., & Domínguez, I. 2018, ApJ, 862, 27
Garnavich, P. M., Bonanos, A. Z., Krisciunas, K., et al. 2004, ApJ, 613, 1120
Geier, S., Marsh, T. R., Wang, B., et al. 2013, A&A, 554, A54
Goldstein, D. A., & Kasen, D. 2018, ApJ, 852, L33
Gómez, G., & López, R. 1998, AJ, 115, 1096
Guillochon, J., Parrent, J., Kelley, L. Z., & Margutti, R. 2017, ApJ, 835, 64
Hallakoun, N., & Maoz, D. 2019, MNRAS, 490, 657
Hicken, M., Challis, P., Jha, S., et al. 2009, ApJ, 700, 331
Hoeflich, P., & Khokhlov, A. 1996, ApJ, 457, 500
Hoeflich, P., Khokhlov, A. M., & Wheeler, J. C. 1995, ApJ, 444, 831
Hollands, M. A., Tremblay, P.-E., Gänsicke, B. T., Gentile-Fusillo, N. P., & Toonen, S. 2018, MNRAS, 480, 3942
Hosseinzadeh, G., Sand, D. J., Valenti, S., et al. 2017, ApJ, 845, L11
Hubble, E. 1929, Proceedings of the National Academy of Science, 15, 168
Iben, Jr., I., & Tutukov, A. V. 1984, ApJS, 54, 335
Jack, D., Hauschildt, P. H., & Baron, E. 2011, A&A, 528, A141
Jacobson-Galan, W. V., Polin, A., Foley, R. J., et al. 2019, arXiv e-prints, arXiv:1910.05436
Jiang, J.-A., Doi, M., Maeda, K., et al. 2017, Nature, 550, 80
Kasen, D. 2010, ApJ, 708, 1025
Kasen, D., Röpke, F. K., & Woosley, S. E. 2009, Nature, 460, 869
Kasen, D., Thomas, R. C., & Nugent, P. 2006, ApJ, 651, 366
Kasliwal, M. M., Kulkarni, S. R., Gal-Yam, A., et al. 2010, ApJ, 723, L98
—. 2012, ApJ, 755, 161
Katz, B., & Dong, S. 2012, arXiv e-prints, arXiv:1211.4584
Kawabata, K. S., Maeda, K., Nomoto, K., et al. 2010, Nature, 465, 326
Kotak, R., Meikle, W. P. S., Pignata, G., et al. 2005, A&A, 436, 1021
Krisciunas, K., Contreras, C., Burns, C. R., et al. 2017, AJ, 154, 211
Kromer, M., Sim, S. A., Fink, M., et al. 2010, ApJ, 719, 1067
Kromer, M., Pakmor, R., Taubenberger, S., et al. 2013, ApJ, 778, L18
Kushnir, D., Katz, B., Dong, S., Livne, E., & Fernández, R. 2013, ApJ, 778, L37
Leavitt, H. S., & Pickering, E. C. 1912, Harvard College Observatory Circular, 173, 1
Leloudas, G., Stritzinger, M. D., Sollerman, J., et al. 2009, A&A, 505, 265
Leung, S.-C., & Nomoto, K. 2020, ApJ, 888, 80
Li, W., Chornock, R., Leaman, J., et al. 2011a, MNRAS, 412, 1473
Li, W., Filippenko, A. V., Gates, E., et al. 2001, PASP, 113, 1178

Li, W., Leaman, J., Chornock, R., et al. 2011b, MNRAS, 412, 1441
Lira, P., Suntzeff, N. B., Phillips, M. M., et al. 1998, AJ, 115, 234
Livne, E. 1990, ApJ, 354, L53
Lunnan, R., Kasliwal, M. M., Cao, Y., et al. 2017, ApJ, 836, 60
MacLeod, M., Goldstein, J., Ramirez-Ruiz, E., Guillochon, J., & Samsing, J. 2014, ApJ, 794, 9
Magee, M. R., Maguire, K., Kotak, R., et al. 2020, A&A, 634, A37
Magee, M. R., Kotak, R., Sim, S. A., et al. 2016, A&A, 589, A89
Maguire, K., Sullivan, M., Thomas, R. C., et al. 2011, MNRAS, 418, 747
Maguire, K., Sullivan, M., Pan, Y. C., et al. 2014, MNRAS, 444, 3258
Margalit, B., & Metzger, B. D. 2016, MNRAS, 461, 1154
Matheson, T., Kirshner, R. P., Challis, P., et al. 2008, AJ, 135, 1598
Mazzali, P. A., Cappellaro, E., Danziger, I. J., Turatto, M., & Benetti, S. 1998, ApJ, 499, L49
Mazzali, P. A., Danziger, I. J., & Turatto, M. 1995, A&A, 297, 509
Mazzali, P. A., & Hachinger, S. 2012, MNRAS, 424, 2926
Mazzali, P. A., Röpke, F. K., Benetti, S., & Hillebrandt, W. 2007, Science, 315, 825
Mazzali, P. A., Sullivan, M., Filippenko, A. V., et al. 2015, MNRAS, 450, 2631
McCully, C., Jha, S. W., Foley, R. J., et al. 2014, ApJ, 786, 134
Metzger, B. D. 2012, MNRAS, 419, 827
Metzger, B. D., Piro, A. L., Quataert, E., & Thompson, T. A. 2009, arXiv e-prints, arXiv:0908.1127
Miller, A. A., Yao, Y., Bulla, M., et al. 2020, arXiv e-prints, arXiv:2001.00598
Moll, R., & Woosley, S. E. 2013, ApJ, 774, 137
Noebauer, U. M., Kromer, M., Taubenberger, S., et al. 2017, MNRAS, 472, 2787
Nomoto, K. 1982a, ApJ, 257, 780
—. 1982b, ApJ, 253, 798
Nomoto, K., Thielemann, F.-K., & Yokoi, K. 1984, ApJ, 286, 644
Nonaka, A., Almgren, A. S., Bell, J. B., et al. 2010, ApJS, 188, 358
Nugent, P., Baron, E., Branch, D., Fisher, A., & Hauschildt, P. H. 1997, ApJ, 485, 812
Nugent, P., Phillips, M., Baron, E., Branch, D., & Hauschildt, P. 1995, ApJ, 455, L147
Nugent, P. E. 1997, PhD thesis, University of Oklahoma
Pan, Y. C., Sullivan, M., Maguire, K., et al. 2014, MNRAS, 438, 1391
Parrent, J. T., Thomas, R. C., Fesen, R. A., et al. 2011, ApJ, 732, 30
Pastorello, A., Mazzali, P. A., Pignata, G., et al. 2007, MNRAS, 377, 1531
Pereira, R., Thomas, R. C., Aldering, G., et al. 2013, A&A, 554, A27
Perets, H. B., Gal-yam, A., Crockett, R. M., et al. 2011, ApJ, 728, L36
Perets, H. B., Gal-Yam, A., Mazzali, P. A., et al. 2010, Nature, 465, 322
Perlmutter, S., Aldering, G., Goldhaber, G., et al. 1999, ApJ, 517, 565
Phillips, M. M. 1993, ApJ, 413, L105
Phillips, M. M., Wells, L. A., Suntzeff, N. B., et al. 1992, AJ, 103, 1632
Pignata, G., Benetti, S., Mazzali, P. A., et al. 2008, MNRAS, 388, 971

Piro, A. L., Chang, P., & Weinberg, N. N. 2010, ApJ, 708, 598
Piro, A. L., & Morozova, V. S. 2016, ApJ, 826, 96
Piro, A. L., & Nakar, E. 2014, ApJ, 784, 85
Polin, A., Nugent, P., & Kasen, D. 2019a, arXiv e-prints, arXiv:1910.12434
—. 2019b, ApJ, 873, 84
Rabinak, I., & Waxman, E. 2011, ApJ, 728, 63
Riess, A. G., Filippenko, A. V., Challis, P., et al. 1998, AJ, 116, 1009
Riess, A. G., Filippenko, A. V., Li, W., et al. 1999, AJ, 118, 2675
Rigault, M., Brinnel, V., Aldering, G., et al. 2018, arXiv e-prints, arXiv:1806.03849
Rosswog, S., Ramirez-Ruiz, E., & Hix, W. R. 2008, ApJ, 679, 1385
Salvo, M. E., Cappellaro, E., Mazzali, P. A., et al. 2001, MNRAS, 321, 254
Scalzo, R. A., Ruiter, A. J., & Sim, S. A. 2014, MNRAS, 445, 2535
Schmidt, W., Ciaraldi-Schoolmann, F., Niemeyer, J. C., Röpke, F. K., & Hillebrandt, W. 2010, ApJ, 710, 1683
Scolnic, D. M., Jones, D. O., Rest, A., et al. 2018, ApJ, 859, 101
Sell, P. H., Arur, K., Maccarone, T. J., et al. 2018, MNRAS, 475, L111
Sell, P. H., Maccarone, T. J., Kotak, R., Knigge, C., & Sand, D. J. 2015, MNRAS, 450, 4198
Shappee, B. J., Holoien, T. W. S., Drout, M. R., et al. 2019, ApJ, 870, 13
Shen, K. J., & Bildsten, L. 2014, ApJ, 785, 61
Shen, K. J., Kasen, D., Miles, B. J., & Townsley, D. M. 2018a, ApJ, 854, 52
Shen, K. J., Kasen, D., Weinberg, N. N., Bildsten, L., & Scannapieco, E. 2010, ApJ, 715, 767
Shen, K. J., Boubert, D., Gänsicke, B. T., et al. 2018b, ApJ, 865, 15
Silverman, J. M., Foley, R. J., Filippenko, A. V., et al. 2012, MNRAS, 425, 1789
Sim, S. A., Röpke, F. K., Hillebrandt, W., et al. 2010, ApJ, 714, L52
Smith, M., Sullivan, M., Wiseman, P., et al. 2020, MNRAS, 494, 4426
Stritzinger, M., Leibundgut, B., Walch, S., & Contardo, G. 2006, A&A, 450, 241
Taubenberger, S. 2017, The Extremes of Thermonuclear Supernovae, 317
Taubenberger, S., Kromer, M., Pakmor, R., et al. 2013, ApJ, 775, L43
Thomas, R. C., Aldering, G., Antilogus, P., et al. 2011, ApJ, 743, 27
Timmes, F. X. 1999, ApJS, 124, 241
Timmes, F. X., & Swesty, F. D. 2000, ApJS, 126, 501
Toonen, S., Perets, H. B., Igoshev, A. P., Michaely, E., & Zenati, Y. 2018, A&A, 619, A53
Townsley, D. M., Miles, B. J., Shen, K. J., & Kasen, D. 2019, arXiv e-prints, arXiv:1903.10960
Turatto, M., Benetti, S., Cappellaro, E., et al. 1996, MNRAS, 283, 1
Wang, X., Li, W., Filippenko, A. V., et al. 2008, ApJ, 675, 626
Wang, X., Filippenko, A. V., Ganeshalingam, M., et al. 2009a, ApJ, 699, L139
Wang, X., Li, W., Filippenko, A. V., et al. 2009b, ApJ, 697, 380
Webbink, R. F. 1984, ApJ, 277, 355
Whelan, J., & Iben, Jr., I. 1973, ApJ, 186, 1007
Wood-Vasey, W. M., Friedman, A. S., Bloom, J. S., et al. 2008, ApJ, 689, 377

Woosley, S. E., & Kasen, D. 2011, ApJ, 734, 38
Woosley, S. E., & Weaver, T. A. 1994, ApJ, 423, 371
Yao, Y., Miller, A. A., Kulkarni, S. R., et al. 2019, ApJ, 886, 152
Yaron, O., & Gal-Yam, A. 2012, PASP, 124, 668
Zenati, Y., Perets, H. B., & Toonen, S. 2019a, MNRAS, 486, 1805
Zenati, Y., Toonen, S., & Perets, H. B. 2019b, MNRAS, 482, 1135
Zheng, W., Kelly, P. L., & Filippenko, A. V. 2018, ApJ, 858, 104
Zingale, M., Nonaka, A., Almgren, A. S., et al. 2013, ApJ, 764, 97
Zingale, M., Almgren, A. S., Sazo, M. G. B., et al. 2018, Journal of Physics: Conference Series, 1031, 012024